

Forest Fire Aerosol – Weather Feedbacks over Western North America Using a High-Resolution, On-line Fully Coupled, Air-Quality Model

Paul A. Makar¹, Ayodeji Akingunola¹, Jack Chen¹, Balbir Pabla¹, Wanmin Gong¹, Craig Stroud¹, Christopher Sioris¹, Kerry Anderson², Philip Cheung¹, Junhua Zhang¹, Jason Milbrandt³

¹Air Quality Research Division, Atmospheric Science and Technology Directorate, Environment and Climate Change Canada, 4905 Dufferin Street, Toronto, M3H 5T4, Canada

²Natural Resources Canada (emeritus), Summerland, British Columbia, Canada.

³Meteorological Research Division, Atmospheric Science and Technology Directorate, Environment and Climate Change Canada, 2121 Trans Canada Highway, Montreal, Canada

Correspondence to: Paul A. Makar (paul.makar@canada.ca)

Formatted: Subscript

Abstract. The influence of both anthropogenic and forest fire emissions, and their and subsequent chemical and physical processing, on the accuracy of weather and air-quality forecasts, was studied using a high resolution, on-line fully coupled air-quality model. Simulations were carried out for the period 4 July through 5 August 2019, at a 2.5-km horizontal grid cell size, over a 2250 x 3425 km² domain covering western Canada and USA, prior to the use of the forecast system as part of the FIREX-AQ ensemble forecast. Several large forest fires took place in the Canadian portion of the domain during the study period. A feature of the implementation was the incorporation of a new on-line version of the Canadian Forest Fire Emissions Prediction System (CFEPPSv4.0). This inclusion of thermodynamic forest fire plume-rise calculations directly into the on-line air-quality model allowed us to simulate the interactions between forest fire plume development and weather.

Incorporating feedbacks resulted in weather improvements in most metrics of both air quality and meteorological model forecast performance that exceeded or matched the, through comparison of no-feedback forecast and feedback simulations with surface, radiosonde, and satellite observations. For the meteorological simulations, these improvements occurred at greater than the 90% confidence, at most times and heights in the atmosphere. The feedback forecast out-performed the feedback forecast at 35 out of 48 statistical evaluation scores, for PM_{2.5}, NO₂, and O₃ level. Relative to the climatological cloud condensation nuclei and aerosol optical properties used in the no-feedback simulations, the on-line fully coupled model's aerosol indirect and direct effects were shown to result in feedback loops characterized by decreased increased surface temperatures in regions affected by forest fire plumes, decreases in stability within the smoke plume, increases in stability further aloft, decreased lower troposphere temperatures, and increased lower troposphere cloud droplet and raindrop number densities. The aerosol direct and indirect effect reduced oceanic cloud droplet number densities and increased oceanic rain drop number densities, relative to the no-feedback climatological simulation. The aerosol direct and indirect effects were responsible for changes to the near-surface PM_{2.5} and NO₂ aerosol concentrations at greater than the 90% confidence level near throughout the forest fires, with model domain, and to NO₂ and O₃ changes remaining below the 90% confidence level concentrations within forest fire plumes.

The simulations show that incorporating aerosol direct and indirect effect feedbacks can significantly improve the accuracy of weather and air quality forecasts, and that forest fire plume rise calculations within a ~~on-line~~ fully coupled model changes the predicted fire plume dispersion and emissions, the latter through changing the meteorology driving fire ~~intensity behaviour~~ and ~~fuel consumption growth~~.

1 Introduction

Atmospheric aerosol particles may be emitted (primary particles) or result from the condensation of the products of gas-phase oxidation reactions (secondary aerosol). With increasing transport time from emission sources, the processes of coagulation (colliding particles stick adhere creating larger particles) and condensation (low volatility gases condense to particle surfaces) tend to result in particles which have a greater degree of internal mixing (internal homogeneous mixtures). Primary and near-source particles are more likely to have a single or a smaller number of chemical constituents (external mixtures).

Atmospheric particles also modify weather through well-established pathways. Under clear sky conditions, the particles may absorb and/or scatter incoming light, depending on their size, shape, mixing state (internal, external or combinations) and their composition. The presence of the particles themselves may thus affect the radiative budget of the atmosphere, resulting in either positive or negative climate forcing (i.e. the absorption of a greater amount of incoming solar radiation versus increased scattering reflection of that radiation back out into space, a process known as the Aerosol Direct Effect; ADE). Aerosols can also alter the atmospheric radiative balance through interactions with clouds, this influence being referred to as the Aerosol Indirect Effect (AIE). Three broad classes of categories by which cloud/aerosol interactions take place (Oreopoulos *et al.*, 2020) include the first indirect effect, where higher aerosol loadings resulting in increasing numbers of cloud droplets with smaller sizes, hence increasing cloud albedo (Twomey *et al.*, 1977), the second indirect effect, where higher aerosol loadings suppress the collision-coalescence activity of the smaller droplets, reducing precipitation/drizzle, changing cloud heights, and changing cloud lifetime in warm clouds (Albrecht, 1989), and aerosol “invigoration” of storm clouds, where higher aerosol loadings may result in delayed glaciation of cloud droplets, in turn leading to greater latent heat release and stronger convection (Rosenfeld *et al.*, 2018).

The uncertainties associated with the ADE and particularly AIE account for a large portion of the uncertainties in current climate model predictions for radiative forcing between 1750 and 2011 (Mhyre *et al.*, 2013). Carbon dioxide is believed to have a positive (warming) global radiative forcing of approximately $1.88 \pm 0.20 \text{ Wm}^{-2}$, while the direct and indirect effects both have nominal values of approximately -0.45 Wm^{-2} , with uncertainty ranges encompassing -0.94 to $+0.07$ and -1.22 to 0.0 Wm^{-2} respectively. These uncertainties have spurred research designed to better characterize the ADE and AIE, and reduce these uncertainties, through both observations and atmospheric modelling. Observational studies of the ADE have established its large impact; for example, high aerosol loading over Eurasian boreal forests has been found to double the diffuse fraction of global radiation (i.e. increased scattering), a change sufficient to affect plant growth characterized via gross primary production (Ezhova *et al.*, 2018). Aerosol assimilation of Geostationary Ocean Color Imager Aerosol Optical Depth (AOD) observations into a coupled meteorology-chemistry model showed that South Korean AOD values increased by as much as 0.15 with the use of assimilation;

72 these increases corresponded to a local -31.39 W m^{-2} reduction in solar radiation received at the surface, and reductions
 73 in planetary boundary layer height, air temperature, and surface wind speed over land, and a deceleration of vertical
 74 transport (Jung *et al.*, 2019). Other studies in East Asia have shown ADE decreasing local shortwave reaching the
 75 surface by -20 W m^{-2} (Wang *et al.*, 2016), as well as significant changes in surface particulate matter and gas
 76 concentrations in response to these radiation changes.

77 However, one commonality amongst the recent studies of the ADE for air-quality models is a tendency towards
 78 negative biases in predicted aerosol optical depths, potentially indicating systematic under-predictions in aerosol mass,
 79 aerosol size, and/or inaccuracies in the assumptions for shape and/or mixing state. Mallet *et al.* (2017) noted this
 80 negative bias for regional climate model AOD predictions associated with large California forest fires compared to
 81 OMI and MRIS satellite observations. Palacios-Pena *et al.* (2018) noted that high AOD events associated with forest
 82 fires were under-predicted by most models in a study employing a multi-regional-model ensemble. The chosen AOD
 83 calculation methodology and mixing state assumptions employed in models also plays a role in systematic biases:
 84 Curci *et al.* (2015) compared aerosol optical depths, single scattering albedos, and asymmetry factors at different
 85 locations to observations, varying the source model for the aerosol composition, as well as the mixing state
 86 assumptions used in generating aerosol optical properties, for Europe and North America. AODs were biased low by
 87 a factor of two or more, regardless of model aerosol inputs or mixing state assumptions at 440 nm, single scattering
 88 albedos were biased low by up to a factor of two, with the poorest performance for “core-shell” approaches, while
 89 asymmetry factor estimates showed no consistent bias relative to observations. However, the assumed mixing state
 90 was clearly a controlling factor in the negative biases; the AOD predictions closest to the observations at 440 nm
 91 assumed an external mixture with particle sulphate and nitrate assumed to grow hygroscopically as pure sulphuric
 92 acid, lowering their refractive index with increasing aerosol size. This mixing state assumption and the different
 93 homogeneous mixture assumptions gave the best fit for single scattering albedo relative to observations. While not
 94 commenting on aerosol direct effect implications, Takeishi *et al.* (2020) noted that forest fire aerosols increase particle
 95 number concentrations but reduce their water uptake (hygroscopicity) relative to anthropogenic aerosols, with the
 96 latter effect reducing the resulting cloud droplet numbers by up to 37%. Mixing state and hygroscopicity properties
 97 of aerosols were thus shown to have a controlling influence on the ADE.

98 The AIE has often been shown to be locally more important for the radiative balance than ADE in terms of magnitude
 99 of the radiative forcing and response of predicted weather to AIE and ADE (Makar *et al.*, 2015(a); Jiang *et al.*, 2015;
 100 Nazarenko *et al.*, 2017). Several recent studies have attempted to characterize the relative importance of the AIE with
 101 the use of multi-year satellite observations, sometimes making use of models and data assimilation. Saponaro *et al.*
 102 (2017) used MODIS/Aqua linked observations of aerosol optical depth and Ångström exponent to various cloud
 103 properties, noting that the cloud fraction, cloud optical thickness, liquid water path, and cloud top height all increased
 104 with increasing aerosol loading, while cloud droplet effective radius decreased, with the effects dominating at low
 105 levels (between 900 to 700 hPa). Zhao *et al.* (2018) examined 30 years of cloud and aerosol data (1981-2011), and
 106 found that increasing aerosol loading up to $\text{AOD} < 0.08$ increased cloud cover fraction and cloud top height, while
 107 further increases in aerosol loading (AOD from 0.08 to 0.13) resulted in higher cloud tops, and larger cloud droplets.
 108 In polluted environments ($\text{AOD} > 0.30$) cloud droplet effective radius, optical depth and water path; cloud droplet

effective radius increased with increasing AOD. The first ADE was most sensitive to AOD in the AOD range 0.13 to 0.30; and the reduction of precipitation efficiency associated with the second aerosol indirect effect occurred for AODs between 0.08 and 0.4, in oceanic areas downwind of continental sources.

However, sources of uncertainty in AIE estimates persist, in part due to the number of poorly understood processes contributing to the atmospheric response to the presence of aerosols. Nazarenko *et al.* (2017) showed that short-term atmospheric radiative changes were reduced in magnitude when sea-surface temperature and sea-ice coupling was included in climate change simulations. Suzuki *et al.* (2019) showed that the vertical structure of atmospheric aerosols, as well as their composition, had a significant influence on radiative forcing. Penner *et al.* (2018) and Zhu *et al.* (2020) examined the impact of aerosol composition on cirrus clouds via ice nucleation, finding negative forcings for most forms of soot, but a contrary impact of secondary organic aerosols. Rothenburg *et al.* (2018) noted that tests of aerosol activation schemes carried out under current climate conditions had little variability, but had much greater variability for pre-industrial simulations, implying that the available data for evaluation using current conditions may poorly constrain ADE and AIE parameterizations used in simulating in past climates.

Forest fires are of key interest for improving the understanding and representation of ADE and AIE in models, due to the large amount of aerosols released during these biomass burning events. Forest fire emissions and interactions with weather are also of interest due to the expectation that the meteorological conditions resulting in forest fires may become more prevalent in the future under climate change (Hoegh-Guldberg *et al.*, 2018). Observations of aerosol optical properties during long-range transport events of North American forest fire plumes to Europe showed 500 nm AOD values of 0.7 to 1.2 over Norway, with Ångström exponents exceeding 1.4 and absorbing angstrom exponents ranging from 1.0 to 1.25, along with single scattering albedos greater than 0.9 at the surface and up to 0.99 in the column over these sites (Markowicz *et al.*, 2016). Biomass burning was shown to have a specific set of optical properties relatively independent of fuel type for three different types of biomass burning in China (cropland), Siberia (mixed forest) and California (needleleaf forest). The increase in upward radiative forcing at the top of the atmosphere due to fires being linearly correlated to AOD (R from 0.48 to 0.68), with slopes covering a relatively small range from 20 to 23 W m^{-2} unit AOD^{-1} . O'Neill *et al.* (2001) showed that forest fires have a profound impact on aerosol optical depth in western Canada, accounting for 80% of the summer AOD variability in that region, with a factor of three increase in AOD levels from clear-sky to forest fire plume conditions. O'Neill *et al.* (2001)'s analysis of TOMS AVHRR and GOES imagery suggested that forest fire aerosols increase in size with increasing downwind distance, due to secondary aerosol aging and condensation chemistry. We note here that reanalyzing the data presented in O'Neill *et al.* (2001) results in a linear relationship between fine mode particle effective radius (r_{eff} , μm) and the base 10 logarithm of distance from the fires (D , km) of $r_{\text{eff}} = 0.0106 \log_{10}(D) + 0.1163$, $R^2 = 0.18$. Mallet *et al.* (2017) simulated AODs in the range 1 to 2 for biomass burning events, and also noted changes in direct radiative forcing at the top of the atmosphere from positive to negative in both model results and simulations, with increasing downwind distance from the sources. Lu *et al.* (2017) carried out simulations with 5-km horizontal grid spacings for the eastern Russia forest fires of 2002 assuming an internal mixture for emitted aerosols with the WRF-CHEM model, and noted impacts on cloud formation for two different periods. The first period was characterized by high cloud droplet and small ice nuclei numbers, where the fire plumes reduced cloud rain and snow water content, large scale

frontal system dynamics were altered by smoke, and precipitation was delayed by a day. The second period was characterized by high numbers for cloud droplets and ice nuclei, where the fire plumes reduced rain water content, increased snow water content, and precipitation locations changed locally across the simulation domain. Russian forest fire simulations for 2010 with suites of ~~on-line~~^{fully} coupled air-quality models (Makar *et al.*, 2015; Palacios-Pena *et al.*, 2018; Baro *et al.*, 2017) showed substantial local impacts, such as reductions in average downward shortwave radiation of up to 80Wm^{-2} and temperature of -0.8°C (Makar *et al.*, 2015(a)).

Given the above developments in direct and indirect parameterizations, and the increasing amount of information available for estimating forest fire emissions, the impact of forest fires on weather, in the context of weather forecasting, is worthy of consideration. Air-quality model predictions of forest fire plumes have been provided to the public under operational forecast conditions of time- and memory-space limited computer resources (e.g. Chen *et al.*, 2019; James *et al.*, 2018; Ahmadvov *et al.*, 2019; Pan *et al.*, 2017). These simulations make use of satellite retrievals of forest fire hot-spots, climatological data on the extent of area burned by land use type, databases of fuel type linked to emission factors, and an *a priori* weather forecast to provide the meteorological inputs required to predict forest fire plume rise. The latter point is worthy of note in the context of the direct and indirect feedback studies noted above – both climate and weather simulations with prescribed forest fire emissions have consistently resulted in large perturbations of weather patterns in the vicinity of the forest fires. However, ~~their~~^{the} approaches for predicting forest fire plume rise and fire intensity and fuel consumption in operational regional scale forecasts up until now have relied on weather forecast information provided *a priori* and hence lacking those meteorological feedback effects.

The connection of the ADE and AIE within ~~a regional~~^{an} air-quality and weather forecast model context is referred to as “coupling”, with such a model being described in that body of literature as “on-line “fully-coupled” (Galmarini *et al.*, 2015) or “aerosol-aware” (Grell and Freitas, 2014).” However, several researchers have examined aerosol-radiative coupling along with fire spread and growth (as opposed to fire intensity and fuel consumption). The latter work employs ~~we note that in the field of~~ very high-resolution forest fire spread and growth models, and due to their very high resolution, an additional level of coupling, that of behaviour modelling, coupling of biomass burning with the atmosphere has also been defined as the interaction of dynamic meteorology with the heat released by the fire, may be included. However, the resolution requirements for these models (and their need for a relatively small computational time step) constrains their application to a relatively small region. A requirement for these approaches is the use of a very high resolution fire growth model imbedded within the air-quality model. At these resolutions, the simulated local-scale ~~where the initial~~ meteorology determines fire spread on the landscape, which ~~This in turn,~~ modifies the temperature and wind fields, in turn affecting future fire spread. The seminal work on this topic was carried out by (Clark *et al.*, (1996), and Linn *et al.*, (2002). More recent work includes the development of the WRF-FIRE model (Mandel *et al.*, 2011; Coen *et al.*, 2013), with full chemistry added in the WRFSC model (Kochanski *et al.*, 2016). Examples of the resolution required for these models include inner domain resolutions of 444 m with an imbedded fire model mesh of 22.2 m resolution, and a time step of 3.3 seconds (Kochanski *et al.*, 2016); 1.33 km with an imbedded fire model mesh of 67.7m, and a time step of 2 seconds (Kochanski *et al.*, 2019), and 222m, with a fire model mesh of 22m and a time step of 2 seconds (Peace *et al.*, 2015). Kochanski *et al* (2016) also noted a 13 to 30 hour computational time requirement to run their high-resolution modelling system. These

modelling efforts allow for this additional level of coupling – but at the expense of additional computation time preventing, at the current state of supercomputer processing, their application on synoptic-scale forecast domains combined with a full gas chemistry and size-resolved multi-component particle chemistry representation. Here we explore the effects of fire emissions characterized by fire intensity and fuel consumption modelling on the aerosol direct and indirect effects over synoptic scale domain. Our coupling ~~The coupling presented in the present paper~~ refers to that between the aerosols released by fires and other sources to meteorology through the ADE and AIE, with the resulting changes in meteorology in turn influencing fire behaviour (fire intensity and fuel consumption, etc.), in turn influencing plume rise, emissions height, and distribution, closing this feedback loop. We do not implement a very high resolution growth model, noting that this is impractical for operational forecasts at the current time, while showing that synoptic scale 2.5km simulations incorporating fire feedbacks may be carried out within an operational window with currently available supercomputers. As shown below, we find that a sufficiently substantial feedback between the aerosol direct and indirect effects can be discerned to change the vertical distribution of emitted pollutants.

A key consideration in parameterizing the AIE (via aerosol-cloud interaction) is the manner in which the cloud condensation process is represented in the meteorological component of the modelling system. In numerical weather prediction (NWP) models, clouds and precipitation are represented by a combination of physical parameterizations that are each targeted at a specific subset of moist processes. These include “implicit” (subgrid-scale) clouds generated by the boundary layer and the convection parameterization schemes (e.g Sundqvist, 1988), and “explicit” clouds from the grid-scale condensation scheme (Milbrandt and Yau, 2005(a,b), Morrison and Milbrandt, 2015, Milbrandt and Morrison, 2016). Depending on the model grid these “moist physics” schemes vary in their relative importance.

However, regardless of the horizontal grid cell size, the grid-scale condensation scheme plays a crucial role in atmospheric models, though to different degrees and using different methods, depending on the grid spacing and the corresponding relative contributions of the implicit schemes. A grid-scale condensation scheme will in general consist of the following three components: 1) a subgrid cloud fraction parameterization (CF, or cloud “macrophysics” scheme); 2) a microphysics scheme; and 3) a precipitation scheme (Jouan *et al.*, 2020). The cloud fraction (CF) is the percentage of the grid element that is covered by cloud (and is saturated), even though the grid-scale relative humidity may be less than 100%. The microphysics parameterization computes the bulk effects of a complex set of cloud microphysical processes. If precipitating hydrometeors are advected by the model dynamics, the precipitation is said to be *prognostic*; if precipitation is assumed to fall instantly to the surface upon production, it is considered *diagnostic*. The precipitation “scheme” is not a separate component per se, since it simply reflects the level of detail in the microphysics parameterization, but it is a useful concept to facilitate the comparison of different grid-scale condensation parameterizations.

With a wide range of grid cell sizes in current NWP models, there is a wide variety of types of condensation schemes and degrees of complexity in their various components. For example, cloud-resolving models (with grid spacing on the order of 1 km or less) have typically used detailed bulk microphysics schemes (BMSs), with prognostic precipitation, and no diagnostic or prognostic CF component (i.e. the CF is either 0 or 1). Large-scale global models use condensation parameterizations, sometimes referred to as “stratiform” cloud schemes, typically with much simpler microphysics and diagnostic precipitation, but with more emphasis on the details of the CF. However, with continually

increasing computer resources and decreasing grid spacing (both in research and operational prediction systems), the distinction between schemes designed for specific ranges of model resolutions is disappearing and condensation schemes are being designed or modified to be more versatile and usable across a wider range of model resolutions (e.g. Milbrandt and Morrison, 2016).

Aerosol-cloud interactions and feedback mechanisms are difficult to represent in grid-scale condensation schemes with very simple microphysics components. For example, to benefit from the predicted number concentrations of cloud condensation nuclei and ice nuclei, the microphysics needs to be double-moment (predicting both mass and number) for at least cloud droplets and ice crystals, respectively. Until recently, detailed BMSs were only used at cloud resolving scales, hence requiring these relatively high resolutions to be recommended in feedback modelling. In recent years, multi-moment BMSs have been used in operational NWP for model grid spacings of 2–4 km (e.g. Seity *et al.*, 2010, Pinto *et al.*, 2015, Milbrandt *et al.*, 2016). Further, condensation schemes with detailed microphysics are starting to use non-binary CF components (e.g. Chosson *et al.*, 2014, Jouan *et al.*, 2020), thereby allowing detailed microphysics to be used at larger scales, and hence allowing the same indirect feedback parameterizations to be used at multiple scales. Nevertheless, the expectation is that detailed parameterization will provide a more accurate representation of cloud formation at the near cloud-resolving scales, without the complicating aspect of a diagnostic CF, motivating the use of km-scale grid spacing for feedback studies.

The formation of secondary aerosols from complex chemical reactions are another key consideration in feedback forecast implementation, given the impact of aerosol composition on aerosol optical and cloud formation properties, as described above.

In the sections which follow, we describe our high resolution, ~~on-line~~^{fully} coupled air-quality model with on-line forest fire plume rise calculations, which was created as part of the FIREX-AQ air-quality forecast ensemble (<https://www.esrl.noaa.gov/csl/projects/firex-aq/>), to address the following questions:

- (1) Will a ~~on-line~~^{fully} coupled model of this nature provide improved forecasts of *both* weather and air-quality, using standard operational forecast evaluation tools, techniques and metrics of forecast confidence? That is, despite the uncertainties in the literature as described above, are these processes sufficiently well described in our model that their use results in a formal improvement in forecast accuracy?
- (2) Are the changes in forest fire plume rise associated with implementing this process directly within a ~~on-line~~^{fully} coupled model sufficient to result in significant perturbations to weather predictions and to chemistry? What are these perturbations?

We employ our ~~on-line~~^{fully} coupled model with 2.5-km grid cell size domain covering most of western North America, and compare model results to surface meteorological and chemical observations, and to vertical column observations of temperature and aerosol optical depth (AOD), in order to quantitatively evaluate the effect of feedback coupling of the ADE and AIE on model performance. We then compare feedback and no-feedback simulations to show the impacts of the ADE and AIE feedbacks on cloud and other meteorological predictions, and on key air quality variables (particulate matter, nitrogen dioxide, and ozone). We begin our analysis with a description of our modelling platform.

2 Model Description

2.1 GEM-MACH

The Global Environmental Multiscale – Modelling Air-quality and CHemistry (GEM-MACH) model in its online coupled configuration has been described elsewhere (Makar *et al.*, 2015a,b; Gong *et al.*, 2015, 2016). Briefly, the model combines the Environment and Climate Change Canada Global Environmental Multiscale weather numerical weather prediction model (GEM, Cote *et al.*, 1998, Girard *et al.*, 2014) with gas and particle process representation using the on-line paradigm, with options for climatological versus full coupling between meteorology and chemistry. GEM-MACH's main processes ~~In GEM-MACH's climatological coupling configuration, prescribed, invariant climatological values for the two configurations aerosol optical properties and cloud condensation nuclei (CCN) are employed here are described within the model's radiative transfer and cloud microphysics modules. In the full coupling configuration, the ADE is simulated using GEM-MACH's predicted aerosol loading and Mie scattering using a binary water-dry aerosol homogeneous mixture assumption, at the 4 wavelengths employed by GEM's radiative transfer algorithms, and at additional wavelengths for diagnostic purposes. The full coupling also includes the AIE by simulating aerosol-cloud interaction via explicit droplet nucleation using the algorithm of Abdul-Razzak and Ghan (2002) along with on-line aerosol composition and size (Gong *et al.*, 2015). This droplet nucleation replaces the decoupled model's existing droplet nucleation calculation in the Predicted Particle Properties (P3) microphysics scheme (Morrison and Milbrandt, 2015, Milbrandt and Morrison, 2016). The latter assumes an invariant aerosol population of a single lognormal size distribution (with a geometric mean diameter of 100 nm and total aerosol number concentration of 300 cm^{-3} , consisting of pure ammonium sulphate; Morrison and Grabowski, 2008). The prognostic cloud droplet number and mass mixing ratios from the P3 microphysics are then transferred back to the chemistry module for using in cloud processing of gases and aerosols (cloud scavenging and chemistry) calculations, completing the AIE feedback process loop (Gong *et al.*, 2015) Table 1. The chemistry modules of GEM-MACH also include process representation for gas-phase chemistry (ADOMII mechanism, 42 gas species, Stockwell *et al.*, 1989), cloud processing including aqueous chemistry, scavenging of gases and aerosols, below-cloud removal and wet deposition (Gong *et al.*, 2015), particle microphysics employing a sectional size distribution and 8 chemical species (Gong *et al.*, 2003), particle inorganic thermodynamics (Makar *et al.*, 2003), the formation of secondary organic aerosols using a modified yield approach (Stroud *et al.*, 2018), process representation for surface fluxes as a boundary condition on the solution for vertical diffusion, and semi-Lagrangian advection for transported chemical tracers.~~

The specific base model version employed in these simulations is GEMv4.9.8/GEM-MACHv2 (Moran *et al.*, 2018), incorporating the following additional improvements in addition to those noted above: (a) the AIE parameterization was modified for use with the P3 cloud microphysics scheme; (b) forest canopy shading and turbulence was parameterized following Makar *et al.*, (2017); (c) anthropogenic plume rise was parameterized through calculating residual buoyancy of the rising plume (Akingunola *et al.*, 2018); (d) emissions of crustal material undergo a meteorological modulation with crustal material emissions being inhibited when the soil water content is predicted to be greater than 10%; (e) emissions/deposition of NH_3 are implemented using a bidirectional flux parameterization (Whaley *et al.*, 2018; Zhang *et al.*, 2003); (f) CH_4 is treated as a reactive and emitted tracer; (g) the KPP-generated

293 ~~RODAS-3 solver (Sandu and Sander, 2006) is used for the solution of ADOMII gas-phase mechanism (Stockwell~~
294 ~~and Lurmann, 1989); (g) MODIS retrievals were used to create monthly leaf area index values for use in the model's~~
295 ~~biogenic emissions, forest canopy shading and turbulence, and deposition algorithms; (h) a parameterization for the~~
296 ~~impacts of vehicle-induced turbulence on vertical diffusive transport was employed (Makar *et al.*, 2020).~~

297 Simulations were carried out with a 2.5-km horizontal grid cell spacing over a 900 x 1370 grid cell domain, covering
298 most of western Canada and the USA (Figure 1). The meteorological boundary conditions for the simulation were a
299 combination of 10-km ~~resolution~~ GEM forecasts updated hourly (themselves originating in data assimilation analyses
300 of real-time weather information; ~~Figure 1(a)~~), and 2.5-km GEM simulations (~~Figure 1(c)~~) employing, in the northern
301 portion of ~~this~~ the 2.5-km domain, the Canadian Land Data Assimilation System (Carrera *et al.*, 2015), to better
302 simulate surface conditions. Both “feedback” and “no feedback” simulations were carried out on a 30-hour forecast
303 cycle (Figure 2). Following the usual practice for weather forecasts, the analysis-driven meteorological forecasts at 10
304 km resolution were updated operationally every 24 hours at 12 UT (~~Figure 2(a)~~). These 10 km resolution ~~weather~~
305 forecasts were ~~used to drive a 30-hour, 10-km resolution GEM-MACH forecast (Figure 1(b), Figure 2(b)), which~~
306 ~~employed ECMWF reanalysis data for North American chemical lateral conditions (Innes *et al.*, 2019). The 10-km~~
307 ~~resolution weather forecasts were also used to drive~~ followed by a 30-hour meteorology-only forecast at 2.5-km
308 resolution on the high resolution domain (~~of~~ Figure 1(c), Figure 2(c)). ~~The last 24 hours of the 10-km resolution~~
309 ~~GEM-MACH forecast was also used to provide chemical lateral boundary conditions for the 24-hour 2.5km on-line~~
310 ~~coupled GEM-MACH simulation (Figure 1(c), Figure 2(d)). The last 24 hours of the 2.5-km GEM simulation which~~
311 were used as meteorological initial and boundary conditions for the 24-hour 2.5-km ~~on-line fully-coupled GEM-~~
312 MACH simulation (~~Figure 1(c), Figure 2(d)). The~~ These two stages of meteorology-only simulations were carried
313 out to prevent chaotic drift from the observed meteorology, and to allow spin-up time for the cloud fields of that
314 meteorology to reach equilibrium (6-hour timeframe). ~~Chemical lateral boundary conditions were taken from~~
315 ~~climatologies based on ECMWF MACC II global atmospheric chemical composition modelling and reanalysis~~
316 ~~(Inness *et al.*, 2013).~~ Chemical initial concentrations for each consecutive forecast within the 2.5-km GEM-MACH
317 model domain were “rolled over” or “daisy-chained” between subsequent forecasts without chemical data
318 assimilation. Forecast performance scores presented here are for the inner 2.5-km domain from this set of linked 24
319 forecast simulations, mimicking operational forecast conditions.

320 2.2 CFFEPS Version 4.0: On-line forest-fire plume rise calculations

321 In addition to the above algorithm improvements relative to GEM-MACH implementations, this model system setup
322 has incorporated the first on-line calculation of forest-fire plume-rise by energy balance driven using on-line
323 meteorology, in a new version of the Canadian Forest Fire Emissions Prediction System (CFFEPS). The algorithms
324 of CFFEPSv2.03 are described in detail and evaluated elsewhere (Chen *et al.*, 2019), but will be outlined briefly here,
325 as well as subsequent modifications to this forest fire emissions processing module.

326 CFFEPS combines near-real-time satellite detection of forest fire hotspots with national statistics of burn areas by
327 Canadian province and by specific fuel type across North America. CFFEPS assumes persistence fire growth in the
328 subsequent 24- to 72-hour forecasts with hourly fuel consumed calculated (kg m^{-2}), based on GEM forecast

meteorology and predicted fire ~~intensity and fuel consumption~~behaviour in grid cells representing fire locations. The modelled fire fuel consumption is then linked with combustion-phase specific emission factors (g kg^{-1}) for fire specific emissions and chemical speciation. Fire energy associated with the modelled combustion process is also estimated, and is used in conjunction with *a priori* forecasts of meteorology within the column to determine plume rise. In its off-line/non-coupled configuration (Chen *et al.*, 2019), CFFEPS carries out residual buoyancy calculations at five preset pressure levels (surface, 850, 700, 500, 250 mb). CFFEPS predicts plume injection heights, which are in turn used to redistribute the mass emissions below the plume top to the model hybrid levels. This approach employed in CFFEPSv2.03 provided a substantial improvement in forecast accuracy relative to the previous approach employing modified Briggs (Briggs, 1965, Pavlovic *et al.*, 2016) plume rise formulae in the offline GEM-MACH forecast system (Chen *et al.*, 2019). A recent evaluation of the plume heights predicted by CFFEPS was carried out utilizing MISR and TROPOMI satellite retrieval data (Griffin *et al.*, 2020). Seventy cases studied using MISR data showed good agreement between satellite and CFFEPS-predicted maximum and mean plume heights (maximum plume height observed versus predicted values and standard deviations: 1.7 ± 0.9 versus 2.0 ± 1.0 km; mean plume height observed versus predicted: 1.3 ± 0.6 versus 1.3 ± 0.4 km). A larger number of case studied using TROPOMI data (671 in total) also showed a reasonable agreement, with CFFEPS showing a small tendency to overpredict heights (maximum observed versus predicted plume heights 2.2 ± 1.6 versus 2.5 ± 1.2 km; mean observed versus predicted plume heights 0.7 ± 0.5 versus 1.1 ± 0.6 km).

However, other work has shown the substantial impact of large forest fires on regional weather (Makar *et al.*, 2015a; Palacios-Pena *et al.*, 2018, Baro *et al.*, 2017), including changes to the surface radiative balance and atmospheric stability. These findings imply that plume rise calculations employing an *a priori* weather forecast lacking the impact of fire plumes via the ADE and AIE may not accurately predict the weather conditions critical to subsequent forest fire plume rise prediction. In order to study this possibility, and to allow forest fire plumes to influence weather and hence subsequent fire spread/growth, several changes were made to CFFEPS implementation, resulting in version 4.0 of CFFEPS, used here. The process flow within CFFEPSv2.03 versus CFFEPSv4.0 are compared in Figure 3. The original C language CFFEPSv2.03 code was converted to FORTRAN90, and following successful off-line comparisons to the original code, was then integrated as an on-line subroutine package within GEM-MACH itself with the near-real-time satellite hotspot data and location fuel parameters being read into GEM-MACH directly (CFFEPSv4.0 is this new on-line package). A key advantage of the CFFEPSv4.0 subroutine integration within GEM-MACH is that the residual buoyancy calculations for plume injection heights are now carried out over the model hybrid model layers, rather than the five coarse resolution, prescribed pressure levels of CFFEPSv2.03, making complete use of GEM-MACH's detailed vertical structure. Additionally, CFFEPSv4.0 allows plume rise calculations to be updated during model runtime. When GEM-MACH is run in ~~on-line fully~~-coupled mode, the ADE and AIE implementations allow model-generated aerosols to modify the predicted meteorology, in turn influencing predicted fire emissions and plume rise, closing these feedback loops. The on-line implementation of CFFEPSv4.0 thus allows us to investigate the effects of meteorology on subsequent forest fire plume development, the changes to modelled aerosol compositions, and, ultimately, the feedbacks to weather.

The formation of particles from forest fires affects meteorology on the larger scale via the ADE and AIE, in turn modifying the regional scale atmospheric features affecting fire growth, such as the temperature profiles below forest fire plumes. ~~However, we note that CFFEPSv4.0 employs forest fire heat to determine plume rise as a subgrid-scale thermodynamic process parameterization rather than a very high resolution explicit fire growth parameterization; the very~~ However, we note that the local scale weather modifications due to the addition of forest fire heat to the atmosphere are not ~~yet~~ incorporated into fire spread or GEM microphysics. Specifically, when the feedback version of GEM-MACH incorporating CFFEPSv4.0 is used in its ~~on-linefully~~ coupled configuration, CFFEPSv4.0 ~~uses estimates of~~ calculates forest fire plume rise using the heat released to calculate forest fire plume rise. These calculations employ lapse rates at the fire locations, that with feedbacks enabled, meteorological predictions which include the ADE and AIE generated by forest fire aerosols on atmospheric stability ~~within from~~ the current ~~on-line fully~~ coupled model timestep. ~~This is The resulting added aerosol mass due to the fire in contrast to earlier off-line implementations of CFFEPS, which made use of a priori non-turn affects the meteorology through ADE and AIE, closing this feedback weather forecast lapse rates loop.~~ To the best of our knowledge, this is the first implementation of a dynamic forest fire plume injection height scheme incorporated into a ~~on-linefully~~ coupled high-resolution, ~~operational~~ air quality forecast modelling system. The impact of this feedback on both weather and air-quality can be substantial, as we show in the following sections.

The locations of the daily forest hotspots detected during the study period, and the corresponding magnitude of the daily PM_{2.5} emissions generated by CFFEPS for each hotspot are shown in Figure 4. Individual hotspots with the highest magnitude emissions are located in the state of Nevada (Figure 4(a), southern boxed region). However, the largest ensemble emissions from a suite of hotspots occurs in northern Alberta (Figure 4(a), northern boxed region). Expanded views of the northern Alberta and Nevada hotspots are shown in Figure 4(b,c) respectively – the use of smaller symbols shows that the Alberta hotspots are groups representing large spreading fires, which overplotted in Figure 4(a), while the Nevada hotspots indicate single fires of small spatial extent and duration rather than larger spreading fires. The Alberta fires are thus the most significant sources of forest fire emissions in the study domain for the period analyzed here.

2.2 Feedback and No-Feedback Simulations

Two simulations were carried out for the period July 4th through August 5th 2019; a “feedback” (ADE and AIE feedbacks enabled – ~~on-linefully~~ coupled model) and a “no-feedback” simulation (ADE and AIE make use of GEM’s climatological aerosol radiative and CCN properties – the ~~one-way coupled decoupled~~ model). During this period, five large forest fires took place in the northern portion of the modelling domain. The two parallel combined meteorology and air-quality forecasts in the ~~on-linefully~~ coupled model with/without ADE and AIE coupling were evaluated ~~for meteorological using the US EPA AIRNOW data (<https://www.airnow.gov>) and air quality variables, Environment and Climate Change Canada’s EMET and ARCAD operational forecast evaluation systems, respectively.~~ Following evaluation, the simulation mean values of hourly meteorological and chemical tracer

predictions were compared to analyze the impact of ~~on-line~~^{fully} coupled ADE and AIE feedbacks on both sets of fields.

3 Model Evaluation

3.1 Meteorology Evaluation

Surface meteorological conditions were evaluated at three-hour intervals from the start of both of the two sets of paired 24-hour forecasts using standard metrics of weather forecast performance including mean bias (MB), mean absolute error (MAE), root mean square error (RMSE), correlation coefficient (R) and standard deviation (σ). In all comparisons, a 90% percent confidence level assuming a normal distribution was used to identify statistically different results between forecast simulations. Note that 90% confidence levels are commonly used in meteorological forecast evaluation, with values of 80% to 85% recommended (Pinson and Kariniotakis, 2004) and up to 90% used (Luig *et al.*, 2001) for variables such as wind speed, rather than the 95% or 99% confidence levels in other fields, in recognition of the difficulties inherent in prognostic forecasts of the chaotic weather system. Here, the confidence range formulation of Geer (2014) has been applied using a 90% confidence level in model predictions, with the statistical measures considered different at the 90% confidence level when the 90% confidence ranges do not overlap. The surface meteorological evaluations shown here only include those variables and metrics where results were significantly different at the 90% confidence level.

Several model forecast output variables were evaluated and the surface variables showing statistically significant differences relative to observations at the 90% confidence level included: 2 m temperature, surface pressure, 2 m dewpoint temperature, 10 m wind speed, sea-level pressure, and accumulated precipitation (the latter in 3 different metrics). The comparisons are shown as time series in three-hourly intervals as a function of forecast hour prediction time forward from forecast hour 0, for grid cells corresponding to measurement locations in Figures 5, 6, 7, 8, 9, 10, and 11 for each of these quantities, respectively. Note that these statistics measure domain-wide performance, across all of the reporting stations within the model domain, during the sequence of 24-hour forecasts comprising the simulation period. The duration of the time series in these comparison figures is thus a function of the duration of the contributing forecasts.

Figure 5 shows an example analysis for surface temperature bias for the entire model domain. Figure 5(a) shows the average model ~~mean bias~~ (MB) time series across all stations and all forecasts at the given forecast hours, while Figure 5(b) shows the corresponding difference in the MB absolute values. The difference plot in Figure 5(b) shows the feedback – no-feedback scores, such that scores below the zero line indicate superior performance of the feedback forecast, while those above the zero line indicate superior performance of the no-feedback forecast. Here, the feedback forecast was statistically superior at forecast hours 3, 6, 15, ~~18~~ and ~~24~~¹⁸ at the 90% confidence level at these forecast hours, and both simulations were at par (differences below the 90% confidence level) at hours ~~9, 12 and 21~~, ~~with the no-feedback forecast being superior at 90% confidence at hour 9, and 24~~. The feedback forecast thus has superior performance, at greater than 90% confidence, over half of the forecast hours evaluated within the domain, ~~equivalent~~

performance at two hours (hours 12 and 21, both within 90% confidence limits), and inferior performance at one hour (hour 9), during the simulation period.

All of the metrics for which surface temperature forecast performance differed at the 90% confidence level are shown in Figure 6. In addition to MB, the scores for MAE, and RMSE showed superior forecast performance for the feedback relative to the no-feedback case at the 90% confidence level for hours ~~6 through 15 and 18~~, while the improvement for the correlation coefficient was only reached the 90% confidence level at ~~hour 18~~~~hours 6 and 12~~.

The meteorological forecast performance metrics with statistically significant differences for surface pressure, dewpoint temperature, and sea-level pressure are shown in Figures 7, 8, and 9 respectively. The model performance differences in these three Figures show a similar pattern: a degradation in performance with the use of feedbacks at hour 3, with the differences between the two forecasts either dropping below the 90% confidence level, or the feedback forecast showing an improvement by hour 9, followed by several hours in which the feedback forecast has a superior performance, usually at greater than 90% confidence. The duration of this latter period varies between the metrics, from up to 18 hours for MAE for surface pressure (Figure 7(b)) to 3 hours for the correlation coefficient of dew-point temperature (Figure 8(d)).

The initial loss of performance for the feedback forecast may represent a form of “model spin-up” that may be unique to on-line coupled models, but may be affected or improved with further adjustments to the forecast cycling setup for the chemical species. As noted earlier (Figure 2), in order to prevent chaotic drift from observed meteorology, we made use of a 30-hour 2.5-km resolution analysis-driven weather forecast to update our on-line coupled model’s initial meteorology at hour zero of each 24 hour forecast. The cloud fields provided as initial conditions at hour zero include observation analysis for the 6 hours prior to hour zero - these have reached a quasi-equilibrium in the high-resolution weather forecast (Figures 2(b,e)) by the time they are used as initial and boundary conditions in the on-line coupled model (Figure 2(c,f)). However, the on-line coupled model’s aerosol fields at hour zero, used to initialize the subsequent forecast (Figure 2, dashed blue arrow), still reflect the locations of aerosol-cloud interactions in the previous on-line coupled simulation. The initial three to six hours of feedback forecast degradation represents the time required for the on-line coupled model to reach a new equilibrium consistent between both its aerosol and the cloud fields.

One possible solution for this model spin-up inconsistency would be to eliminate the intermediate driving 2.5-km meteorological simulation in favour of a longer 30-hour on-line coupled forecast with the first six hours removed as spin-up (i.e. extend the duration of steps (c) and (f) in Figure 2 to 30 hours, starting at UT hour 6). The duration of the forecast experiments carried out here was limited to 24 hours due to limited computational resources, and, more importantly, the operational requirement for an on-time forecast delivery for the purpose of the FIREX-AQ field campaign. The 24-hour forecast simulations carried out in Figure 2 (c,f) each required nearly 3 hours of supercomputer processing time; longer simulation periods were not possible within the operational window available for forecasting.

Model 10-m windspeed forecasts were also improved with the incorporation of feedbacks for ~~hours 3 and 6, for all metrics (Figure 10), hour ranges between hour 3 and hour 12, depending on the metric, with the longest duration improvement for MB, MAE, and RMSE, and the shortest duration for correlation coefficient and standard deviation~~

(Figure 9). A decrease in MB, marginal performance degradation of the feedback forecast at close to 90% confidence at hours 21 and 24 can also be seen for root mean square error, correlation coefficient, and standard deviation in this Figure.

Precipitation forecast performance from the two simulations varied depending on the metric chosen (Figure 11). The metrics in this case were based on the number of coincident precipitation “events” versus “non-events” as shown in contingency Table 24.

The Heidke skill score { $HSS = \frac{2(AD - BC)}{[(A + C)(C + D) + (A + B)(B + D)]}$ } measures the fractional improvement of the forecast over the number correct by chance. The Frequency Bias { $FB = (A + B) / (A + C)$ } measures the frequency of event over-forecasts ($FB > 1$) versus event under-forecasts ($FB < 1$). The Equitable Threat score { $ETS = (A - \tilde{A}) / (A + C + B - \tilde{A})$, where $\tilde{A} = (A + B)(A + C) / (A + B + C + D)$ } measures the observed and/or forecast events that were correctly predicted. Following standard practice at Environment and Climate Change Canada, the HSS is used as a measure of total precipitation accumulated over a 6-hour interval, with no lower limit on the amount of precipitation defining an “event”, while FB and ETS define precipitation “events” as being those with greater than 2mm / 6 hours – consequently FB and ETS have a smaller number of data points for comparison than HSS.

Figure 11 shows improvements to the on-line fully coupled precipitation forecast at the 90% confidence level were seen for the HSS 6-hour accumulated metric at hours 12, 18 and 24, while the frequency bias index of 6-hour accumulated precipitation showed degradation at hours 6 and improved performance at hour 12, 24, and the equitable threat score of 6-hour accumulated precipitation showed significant differences at 90% confidence between the two simulations degradation at hour 24. As is noted above, the latter two metrics employed a minimum 6-hour precipitation threshold of 2 mm prior to comparisons (this is the reason for the reduced number of points available for comparison in Figure 11(b,c) relative to Figure 11(a)). These findings suggest that the on-line fully coupled model's improvements for trend towards improved total precipitation over time (Figure 11(a)) are the result of slightly improved performance for relatively light low-level precipitation events ($< 2 \text{ mm } 6 \text{ hr}^{-1}$), offsetting a degradation of performance for higher level precipitation events. Precipitation events have thus become more frequent, but “lighter” with the use of the feedback parameterizations.

The meteorological forecast performance metrics with statistically significant differences for surface pressure, dewpoint temperature, and sea level pressure are shown in Figures 7, 8, and 10 respectively. The model performance differences in these three Figures show a similar pattern: a degradation in performance with the use of feedbacks at hour 3, with the differences between the two forecasts either dropping below the 90% confidence level, or the feedback forecast showing an improvement by hour 6, followed by several hours in which the feedback forecast has a superior performance. The duration of this latter period varies between the metrics, from up to 18 hours for MAE for surface pressure (Figure 7(b)) to 6 hours for the standard deviation of dew-point temperature (Figure 8(d)).

We believe that the initial loss of performance for the feedback forecast may represent a form of “model spin-up” that may be unique to fully coupled models, but may be affected or improved with further adjustments to the forecast cycling setup for the chemical species. As noted earlier (Figure 2), in order to prevent chaotic drift from observed

meteorology, we made use of a 30-hour 2.5-km resolution analysis-driven weather forecast to update our fully coupled model's initial meteorology at hour zero of each 24-hour forecast. The cloud fields provided as initial conditions at hour zero include observation analysis for the 6 hours prior to hour zero—these have reached a quasi-equilibrium in the high-resolution weather forecast (Figures 2(b,e)) by the time they are used as initial and boundary conditions in the fully coupled model (Figure 2(c,f)). However, the fully coupled model's *aerosol* fields at hour zero, used to initialize the subsequent forecast (Figure 2, dashed blue arrow), still reflect the locations of aerosol-cloud interactions in the previous fully coupled simulation. We believe that the initial three to six hours of feedback forecast degradation represents the time required for the fully coupled model to reach a new equilibrium consistent between both its aerosol and the cloud fields.

One possible solution for this model spin-up inconsistency would be to eliminate the intermediate driving 2.5-km meteorological simulation in favour of a longer 30-hour fully coupled forecast with the first six hours removed as spin-up (i.e. extend the duration of steps (c) and (f) in Figure 2 to 30 hours, starting at UT hour 6). The duration of the forecast experiments carried out here was limited to 24 hours due to limited computational resources, and, more importantly, the operational requirement for an on-time forecast delivery for the purpose of the FIREX-AQ field campaign. The 24-hour forecast simulations carried out in Figure 2 (c,f) each required nearly 3 hours of supercomputer processing time; longer simulation periods were not possible within the operational window available for forecasting.

The amalgamated observations and model pairs of vertical temperature profile data from 39 radiosonde sites in western North America are shown in Figures 12 and 13. Improvements in the forecasted temperature vertical profile with increasing forecast time are evident at 250, 300, 400, 500, and 850 hPa in the 12th hour forecast, with degradations at 200 and 700 hPa (Figure 12). Improvements and at 300, 925 and 1000 hPa may be seen in the 24th hour (Figure 13) forecast; it is. The forecast simulation with aerosol feedbacks enabled also worth noting the entire region at and below 300 showed slight improvements in the 10, and 50 hPa 12th hour temperatures and 50 hPa has improved temperature forecasts (mean values to the left of the vertical line), albeit not always at >90% confidence. 24th hour temperatures, while 500 hPa 24th hour temperature performance degraded slightly. There are larger differences between the 1000 hPa forecasts, though these also have the least number of contributing stations (i.e. only those located close to sea-level contribute to the lowest level temperature biases). Other levels of the atmosphere showed no statistically significant change at the 90% confidence level in temperature profile forecast performance with the use of feedbacks.

3.2 Chemistry Evaluation

Improvements to airChemistry-forecast quality model performance is usually evaluated using standard statistical metrics have been a focus for research since the 1980's starting with dispersion model evaluation (Fox, 1981), and the identification of mean bias and normalized mean square error as potentially useful metrics to complement the Pearson correlation coefficient (Hanna, 1988). More recently, the Pearson correlation coefficient has been noted as being capable of producing high values for relatively poor model results (Krause *et al.*, 2005), as well as being unable to distinguish systematic model underestimation (Yu *et al.*, 2006), unable to provide information on whether data series have a similar magnitude and capable of providing a false sense of relationship where none exists due to outliers.

(Duveiller *et al.*, 2016) and clusters of model-observation pairs (Aggarwal and Ranganathan, 2016). More recently, model evaluation has focused on metrics which do not have the tendency to weight the higher magnitude values unduly (a particularly useful property with air-quality variables which may vary by several orders of magnitude), which are dimensionless (allowing a comparison across different evaluated variables), and which are bounded and symmetric (properties allowing comparisons to be made and equally valued across the entire range of possible concentrations; e.g. Yu *et al.* (2006)). Metrics such as the modified coefficient of efficiency (Legates and McCabe, 1999) and the more recent incarnations of the Index Of Agreement (Willmott *et al.*, 2012) are examples of the more recent metrics used for air-quality model evaluation. Here, we have made use of a range of metrics spanning the literature on this topic, with the understanding that the properties of different metrics vary, that no single metric provides a perfect means of evaluating model performance, and that a variety of metrics should be applied. The metrics used here span the variety that have appeared in the literature since the early 1980's, and include Factor of 2, Mean Bias, Mean Gross Error, Normalized Mean Gross Error, Correlation Coefficient, Root Mean Square Error, Coefficient of Efficiency, and Index of Agreement. The formulae for these metrics and a brief description of their relative advantages and disadvantages appears in Appendix A (Supplemental Information).

~~against hourly observations collected from surface measurement stations.~~ Both simulations' performance for ozone (O_3), nitrogen dioxide (NO_2) and particulate matter with diameters less than $2.5\ \mu m$ ($PM_{2.5}$) were evaluated using the above metrics, employing hourly AIRNOW data (USA: AQS network: <https://www.epa.gov/aqs>; Canada: NAPS network: <http://maps-cartes.ec.gc.ca/mspa-naps/data.aspx>) and the *openair* package (Carslaw and Ropkins, 2012). The summary performance metric scores for the two simulations grouped, according to contributing measurement network, are shown in Table 32, with boldface values indicating the better score for the given simulation case. With respect to this table, we note that:

- (a) The feedback simulation generally outperforms the no-feedback simulation (more bold-face scores in the "feedback" rows, for 35 out of 48 metric comparisons columns, with a few notable exceptions, discussed below).
- (b) ~~Feedback forecast score improvements occurred were more noticeable for $PM_{2.5}$ (usually first to second digit), followed by O_3 , with the NO_2 scores often being the same for the first few digits. In some evaluation metrics, the feedback simulation showed substantial quantitative improvements over the no feedback simulation (e.g. feedback $PM_{2.5}$ MB is reduced by over a factor of 3 relative to its no feedback counterpart over Western Canada, the region of wildfire activity).~~
- (c) We note that the boundary conditions employed for our 2.5km simulations had a strong impact on model air-quality performance. As described above, these boundary conditions originated in a 10-km resolution simulation making use of ECMWF global reanalysis values on its own lateral boundaries. The magnitudes of the statistics of Table 3 may be compared to the magnitudes of the statistics from our initial ACPD submission (which made use of a MOZART 2009 reanalysis for chemical lateral boundary conditions for the 2.5km GEM-MACH domain). The use of feedbacks had a similar relative impact on forecast performance (34 out of 48 statistics improving in the feedback forecast in the initial simulation, compared to 35 out of 48 statistics in the current work). However, the net impact of the ECMWF-driven 10-km GEM-MACH values being used for chemical

lateral boundary conditions, rather than the MOZART climatology, was a degradation of performance. As we show below, however, the revised boundary conditions led to improvements in model aerosol optical depth performance relative to observations.

(c) For cases when the no-feedback simulation outperforms the feedback simulation, the relative magnitude of the performance difference is smaller than the feedback simulation's improvements (e.g. Western USA PM_{2.5} and Western Canada NO₂ mean bias degradations of 9.0 and 27.8 percent relative to the PM_{2.5} improvement of a factor of 3 noted above).

(d) Both simulations have negative mean biases for O₃ of -3.5 to -3.7 ppbv throughout the model domain, negative biases for PM_{2.5} in the Western USA, positive biases for PM_{2.5} in Western Canada, negative biases for NO₂ in Western Canada and positive biases for NO₂ in the Western USA.

One possible cause for the overall model biases noted in (d) may reside in inadequate chemical boundary conditions used for the forecasting setup. An unprecedented large high-resolution (2.5 km) model domain and on-time delivery of forecasts in support of FIREX-AQ put a significant constraint on available computational resources. 2.5 km chemical boundary conditions for these simulations were taken from seasonal climatologies from ECMWF global model analyses, rather than coarse resolution model simulations. During the time simulated, large forest fires occurred both within the domain (in northern Alberta and Saskatchewan in Canada), and outside of this model domain (in Alaska north of the Panhandle). These out-of-domain sources were thus not available as lateral boundary conditions on the 2.5 km domain, with possible impacts on model performance for the three species thus resulting in overall forecast biases in both the feedback and the no-feedback simulations, particularly in Western Canada.

The impact of lateral boundary conditions on model predictions can be seen when comparing MODIS retrievals of aerosol optical depth (AOD) with model predictions (Figure 14). AOD is a function of both the particle's abundance and optical properties, integrated throughout the vertical column. However, direct comparisons between satellite and model-predicted AOD values must be undertaken with some care, due to the nature of the satellite retrieval/retrievals quality assurance and control procedures, the motion of the orbiting spacecraft, and the scan time of the instrument. The manner in which AOD is calculated introduces additional uncertainty due to the range of values which may be derived from the same aerosol speciation using different methodologies (Curci *et al.*, 2015). For a polar-orbiting instrument such as MODIS, the time at which overpasses occur varies with location, and valid satellite retrievals may not occur when the location being scanned is obscured by clouds. Observed averages may be built up over multiple valid scans over time, but the number of valid scans contributing to the local average at any given location will vary, due to the time and space variation in cloud cover. Here, individual valid Collection 6.1 MODIS/Aqua (MYD04_L2 AOD_550_Dark_Target_Deep_Blue_Combined) 10 km resolution 550 nm AODs were matched in time and space to the nearest model 2.5-km grid cell and output frequency hour. Levy *et al.*, (2013) contains details on the MODIS combined AOD product. No averaging was employed in our comparison (Figure 14); all satellite overpass AOD pixels and matching model AOD pixels are shown. Noting that the Both model and observed values were then locally averaged across the simulation period, to a common resolution 0.1° latitude longitude grid co-located with the model grid, in order to generate the comparison shown in Figure 14. Individual pixels of this image thus incorporate a

spatially varying number of values in the local averages, but these local averages are matched in time, space, and local averaging period. The region over which comparisons were made thus corresponds to the high-resolution model domain, and white areas within the images correspond to regions where satellite data used in the averaging were excluded due to QA/QC constraints, such as the presence of clouds, surface ice, etc.

The MODIS-observed local average AOD values of Figure 14 (a,b) are generally higher than the model predictions (c,d), with the exception of the region co-located with large forest fires in Northern Alberta and Saskatchewan (Figure 14 (d), yellow regions). In addition, as noted above, other satellite imagery has shown the presence of several large forest fires occurring in Alaska, outside of the modelling domain, with smoke plumes extending from these sources down through the northern and western coastal boundaries of the model domain (yellow regions in Figure 14(a)). It is likely that at least some of the biases in PM_{2.5} and NO_x and consequently in the production of secondary ozone, reflect the absence of these sources. Scatterplots of all paired AOD values in Figure 15 (a,b) and for the northern portion of Alberta (Figure 15(c,d)) show that the overall negative bias is due to a large number of underestimated “background” values of AOD in the model simulations, while in the immediate vicinity of the Alberta/Saskatchewan forest fires, model values are considerably higher than observations.

The local model positive biases in AOD colour scale is logarithmic, the model simulation driven using the ECMWF + 10-km resolution GEM-MACH for boundary conditions (Figure 14(b)) is a much better match to observations (Figure 14(a)) than the model simulation driven by MOZART climatological boundary conditions (Figure 14(c)). The slope of the linear best fit line between all observation and model pairs in each case mirrors this finding, with the original (MOZART climatology) boundary conditions having a slope of 0.15 and R² of 0.0382, and the revised ECMWF + GEM-MACH 10-km boundary conditions having a slope of 0.56 and an R² of 0.067.

within Northern Alberta might partly be attributed to overestimates in emitted particulate matter mass in the CFFEPS module, or from inaccurate treatment of fire plume centerline dispersion downwind of primary emissions over large fire sources. Previous work with CFFEPS by Chen *et al.* (2019) for the 2017 fire season has shown similar PM_{2.5} positive biases for western Canada, with MB of +5.8 µg m⁻³ (88 stations) and for Western USA with MB of +8.6 µg m⁻³ (221 stations). These positive biases (Chen *et al.*, 2019) were higher specific to sub-regions closer to areas of active fires (MB of +12 µg m⁻³ for the sub-region including the provinces of Alberta and British Columbia, and +29 µg m⁻³ for the sub-region comprising the states of Idaho, Montana, Oregon and Washington, respectively). At least part of the positive biases may be due to 10km GEM-MACH forest fire emissions occurring in the state of Alaska being overestimated during the study period. However, the ECMWF reanalysis also captures significant particulate mass crossing the Bering Strait from fires in Siberia during this period, so the relative contributions of fires within the low resolution GEM-MACH domain and the ECMWF boundary conditions driving that domain are combined, and can't be separated in the runs carried out. Our analysis here and these earlier results suggest a positive bias in CFFEPS' PM_{2.5} emissions or insufficient dilution/vertical extent of the predicted fire plumes.

The local AOD positive biases associated with fires could also be the result of the mixing state assumptions of the Mie code used here for generating aerosol optical properties. These assumptions may also account for negative AOD biases over much of the remainder of the model domain. We have used a mass-weighted homogeneous mixture

approach, with the complex refractive index values for the 8 particle species being calculated for pure water-dry component homogeneous mixtures at each of the 12 particle size bins, followed by mass weighting to generate values for each of the model components. As noted earlier, this overall negative bias of AOD predictions (both boundary condition configurations result in observation:model slopes less than unity) is a common problem in air-quality models, and may be due to assumptions regarding the model mixing state (Curci *et al.*, 2015). That comparison of multiple mixing state assumptions on AOD with observations for European and North American modelling domains (Curci *et al.*, 2015), showed a typical factor of two model under-prediction of 440 nm North American AOD across all mixing state assumptions, with European AOD negative biases ranging from unbiased to a factor of 2. For the latter group, those models employing an assumption of external mixing, with hygroscopic growth factors for sulphate and nitrate assumed to be similar to those of sulphuric acid, had the highest AODs and hence closest values compared to observations at 440nm. However, in that investigation, the latter method also sometimes resulted in AOD over-predictions by a factor of 2 at 870 nm. These earlier findings along with overestimates at forest fire plumes with our current homogeneous mixture approach at 550nm suggest that the hygroscopic growth may be overestimated for forest fire particles, in turn overestimating forest fire AODs locally, while external mixing assumptions may be required to improve model AOD performance elsewhere in the model domain.

3.3 Model Evaluation Summary

Overall, the incorporation of feedbacks in this study has resulted in improvements in weather and air-quality forecast accuracy, albeit with some caveats. Weather forecast variables showed improvements at the 90% confidence level for several fields, and vertical profiles showed a matching performance or improvements at most levels, particularly close to the surface, and times with increasing forecast lead time. Total precipitation scores also showed minor improvements or matching performance at the 90% confidence level improved. A previously unexpected spin-up issue specific to on-line fully coupled models was noted: the impact of on-line fully coupled particulate matter on cloud variables was sufficiently strong that cloud field adjustment in the first 6 hours of the forecast was required prior to some weather forecast variable improvements to be apparent (surface pressure, dewpoint temperature, sea-level pressure). While the current forecast cycling duration was constrained by operational requirements, this suggests that forecast cycling should include both air-quality and meteorological variables during on-line fully coupled forecast spin-up periods. That is, the model tracer concentrations 6 hours prior to the current forecast start-up could also be used during the initial meteorological spin-up period, thus allowing chemistry and cloud formation to spin-up simultaneously. Scores for surface PM_{2.5}, NO₂, and O₃ also generally improved with the incorporation of feedbacks (35 out of 48 comparisons showed improvements). The choice of lateral boundary conditions was shown to have a significant impact on chemical performance within the model domain, with some metrics showing large improvements. In comparison to satellite-based AOD values, the current model's AOD values were generally biased low, with smaller magnitude biases exceptions being associated with the ECMWF + 10-km GEM-MACH boundary conditions in the regions of Alberta and Saskatchewan with active forest fires where AOD was biased high. The latter comparison also showed that large fires off-domain in Alaska and Siberia likely had a large impact on AODs in the eastern and northern section of the model domain, through comparison with our initial, due to missing boundary

Formatted: Font: Italic

condition contributions. These sources were missing due to operational limitations in the model simulations, shown here.

4 Effects of Feedbacks on Selected Simulation-Period Average Variables

In this section, we compare time averages of the entire study period for the two simulations, both at the surface and in vertical cross-sections through the model domain, to illustrate some of the changes in both weather and air-quality associated with the incorporation of feedbacks. We have found differences at greater than 90% confidence between the predicted meteorological and chemical forecasts in the vicinity of the Alberta/Saskatchewan forest fires, as well as in contrasting changes between land and sea. We note again here that the “no-feedback” simulation makes use of time and spatially invariant aerosol CCN and optical properties, within the meteorological portion of the model. The comparisons thus show the differences associated with the use of climatological constant aerosol properties, and the on-line fully coupled model-generated aerosols.

As in the meteorological evaluation, we have made use of 90% confidence levels in order to gauge the level of significance of the differences between the feedback and no-feedback simulations in the following analysis. At each model grid cell the values of the standard deviation about the mean for each respective simulation was calculated. The difference between the means becomes significant at a given confidence level c if the regions defined by $M_f \pm z^* \frac{\sigma_f}{\sqrt{N}}$ and $M_{nf} \pm z^* \frac{\sigma_{nf}}{\sqrt{N}}$ do not overlap, where N is the number of points averaged, M_f is the feedback mean value, M_{nf} is the no-feedback mean value, σ_f and σ_{nf} are the corresponding standard deviation, and z^* is the value of the \sqrt{c} percentile point for the fractional confidence interval c of the normal distribution ($z^* = 1.645$ at $c = 0.90$). Grid cell values where this overlap does not occur (i.e. where the mean values differ at or above the 90% confidence level) may be defined via the following equation¹:

$$\frac{|M_{nf} - M_f|}{z^* (\sigma_f + \sigma_{nf})} > 1 \quad (1)$$

The approach for representing model grid value 90% confidence levels is described in detail in SI Appendix A2. The differences in the mean grid cell values between the simulations for which the above quantity is greater than unity thus differ at or greater than the 90% confidence level. Differences in the mean values, as well as the value of the above ratio, are thus reported in the following section.

4.1 Effects of Feedbacks on Time-Averaged Meteorology

The feedback – no-feedback differences in the simulation-period average cloud droplet number density (number kg^{-1} of air) and mass density (g water kg^{-1} of air) along centred cross-sections spanning the length and width of the 2.5-km

¹ Note that for cases where $M_{nf} > M_f$, significance at the confidence level associated with z^* occurs when the range of standard errors about the mean do not overlap, i.e. $M_{nf} - z^* \frac{\sigma_{nf}}{\sqrt{N}} > M_f + z^* \frac{\sigma_f}{\sqrt{N}}$, or $(M_{nf} - M_f) / \left(\frac{z^*}{\sqrt{N}} (\sigma_{nf} + \sigma_f) \right) > 1$. Similarly, for cases where $M_f > M_{nf}$, significance at the confidence level associated with z^* occurs when $(M_f - M_{nf}) / \left(\frac{z^*}{\sqrt{N}} (\sigma_{nf} + \sigma_f) \right) > 1$. Equation (1) may thus be used to describe both conditions.

Formatted: Justified

resolution model domain are shown in Figure 15 (cross-section 16 (the locations of the cross-sections are shown in Figure 1). The “Ocean”, “Land”, and “Forest Fire” regions identified are with reference to the approximate locations of these features along these cross-sections. Figure 15-16 also shows the confidence ratio values as described above – regions where the predicted mean values differ at or above the 90% confidence level are shown in red, while those differences below the 90% confidence interval are shown in blue. Feedbacks increase the cloud droplet number density over the northern part of the domain, including the region impacted by the Alberta/Saskatchewan forest fires, from the surface up to about 500600 mb (roughly equivalent to hybrid level 0.500600), and decrease at higher elevations further to the south aloft and along the length of the model domain into the western USA (Figure 15-16(a)). Cloud droplet numbers also decrease over the ocean, but increase eastwards over the land (Figure 15-16(b)). The latter is unrelated to the forest fires; this is an indication that the modelled aerosol number concentration over the ocean is much lower than the single climatological aerosol population assumed in the no-feedback run, resulting in lower cloud droplet number concentrations. The changes in both cases, the differences are significant at the 90% confidence level from the surface up to hybrid level 0.60 in the northern region which is most impacted by forest fire smoke, and in isolated regions further aloft at hybrid level 0.550 along the south to north cross-section (Figure 15-16(c)), and over the regions of the ocean in the west to east cross-section (Figure 15-16(d)). Higher-than-climatology aerosol loadings, a large portion of which are due to the forest fires, resulted increased cloud droplet number densities in the lower troposphere, while decreasing them in the mid-to-upper troposphere (Figure 15(a)). This impact of feedbacks is in accord with the satellite observations of Saponaro *et al.* (2017), and was also seen in Takeishi *et al.* (2020). In contrast, cloud droplet mass density (i.e. cloud liquid water content) largely decreases across the domain along the north-south cross-section (Figure 15-16(e)), as well as over the ocean, with a varying pattern over the land in the east-west cross-section (Figure 15-16(f)). The magnitudes and significance levels for the average change in cloud droplet mass are lower than for cloud droplet number, with the most significant differences occurring over the ocean (Figure 15-16(g,h)). Consistent with the cloud droplet number changes, rain droplet numbers and mass mixing ratios increase aloft with the feedback simulation, over both the forest region impacted by the forest fires (Figure 16-17(a,e)) and over the ocean (Figure 16-17(b,f)), with a varying impact over the land and more distant from the forest fire sources (Figure 16-17(f)). The changes are significant at the 90% confidence level for rain droplet number in these regions (compare Figure 16-17(a) with 16-17(c); 16-17(b) with 16-17(d)), while the rain droplet mass changes sometimes reach approach but are usually below the 90% confidence level (Figure 16(g,h)). These results suggest that relative to the no-feedback simulation, which employs climatological aerosol CCN properties, the AIE in the feedback simulation is causing significant change in hydrometeor numbers, and a less significant increase in hydrometeor mass. In the forest fire-impacted region, the ADE and AIE in the feedback simulation significantly increase the number of cloud droplets near the surface and throughout decrease the number of cloud droplets in the middle to upper troposphere (Figure 15-16(a,c)). The rain drop number in the middle troposphere (Figure 16-17(a,c)) also increases significantly between hybrid levels 0.90 to 0.70 (Figure 16-17(e,g)). Near-surface rain drop number and rain drop mass differences throughout the cross sections (Figure 16-17(e,f)) fall below the 90% confidence level (Figure 16-17(g,h)).

Over the oceans, water droplet number and mass both decrease (Figure 15+6(b,f)), and raindrop number and mass increase (Figure 16+7(b,f)); more atmospheric water is converted to rain drops as a result of the feedbacks, relative to the climatology in the no-feedback simulation. However, these changes are more significant aloft than at the surface, with the difference in both rain drop number and mass falling below the 90% confidence level near the surface. We interpret these changes as a shift in over-ocean liquid hydrometeor numbers and to a lesser degree the water mass aloft from cloud droplets to rain drops due to the AIE in the feedback setup relative to the climatology of the no-feedback simulation. The changes occur at the 90% confidence level aloft, but the near-surface changes are smaller and are usually below the 90% confidence level.

Differences in the average surface precipitation flux and the confidence ratio values are shown in Figure 17+8. Changes in average precipitation (Figure 17+8(a)) appear random, though locally these differences are significant at the 90% confidence level (Figure 17+8(b)). Both the magnitude of the differences and the frequency in their reaching the 90% confidence level increase south-westwards. Given the local and episodic nature of rainfall events, the high level of significance in this case probably results from the presence or absence of individual rainfall events between the two simulations affecting the local average and standard deviations.

Several systematic changes in the average values of the model's meteorological output fields were noted due to the use of feedbacks relative to aerosol property climatologies (Figure 18+9), although all fall below the 90% confidence level for the difference in the mean values between the two simulations (Figure 19). Specific humidity, surface air temperature generally increased (Figure 19(b)) though less so in the region most affected by forest fires (Figure 18(a), surface air temperature decreased below the smoke plumes while increasing further south (Figure 18(b)), while dewpoint temperature decreased (Figure 18+9(c)), implying a decrease in relative humidity with feedbacks. Surface pressure increased over the land (mostly east of the Rockies), particularly in the region downwind of the Alberta/Saskatchewan fires while decreasing over the ocean (Figure 18+9(d)). Planetary boundary layer height increased over the land (Figure 18+9(e)) except in the immediate vicinity of the Alberta/Saskatchewan fires, consistent with decreased atmospheric stability in the lowest part of the atmosphere. The friction velocity also increased with the use of feedbacks (Figure 18+9(f)); this is consistent with a decrease in stability and an increase in turbulent energy. The air temperature increases occur at the surface south of the forest-fire impacted region are limited to the lowest part of the atmosphere (Figure 21 (a,b)), usually below hybrid level 0.914 (approximately 1 km above the surface). The feedbacks decrease temperatures between hybrid levels 0.914 and above roughly 750 mb, decreasing temperatures from the surface in the forest-fire impacted region up to 750 mb (Figure 20 (a,b)), 0.724. Feedbacks thus increase near-surface or do not affect temperatures, relative to the no-feedback meteorological model's simple aerosol climatology, in regions far from the fires, decreasing them near the fires surface, and decrease temperatures in the lower free Troposphere, and increase temperatures further aloft. All—However, all of these differences between feedback and no-feedback simulations features, despite their large geographic range, fall below the local 90% confidence ratio. However, when the differences in air temperature resulting associated with feedback and no-feedback forecasts are compared to observations across the entire domain (as opposed to at gridpoint locations as in Figures 18 and 19) 90% confidence level, reflecting the large variability in surface temperatures contained within each simulation. Longer time simulations than carried out here are required in order to improve confidence in the

temperature predictions across all forecast hours. However, these results, particularly for surface temperature, may be contrasted with Figures 6(a), 12 and 13, which suggests that temperature differences rise above the 90% confidence level is exceeded both at the surface interval at specific forecast times (Figure 6(a)), and at multiple heights aloft at the 12th and 24th forecast hours (Figures 12, 13), at surface and upper atmosphere measurement sites.

4.2 Effects of Feedbacks on Time-Averaged Chemistry

In the previous meteorological impacts section, changes in aerosol loading relative to the climatology, dominated by forest fires, were shown to have a significant impact on cloud formation and atmospheric temperatures through ADE and AIE. These might be expected to in turn influence and be influenced by particulate matter emitted by the forest fires, with the plume rise of the forest fires dependent on the meteorological changes. Air temperatures increase slightly in the model surface layer south of the fires (Figure 1849(b), +0.01 to +0.05 °C) but decrease at greater magnitudes through the rest of the lower Troposphere (surface near the fires to hybrid level 0.749980 up to 0.667, Figure 20(a), 21), with a maximum decrease of -0.5°C between hybrid levels 0.893871 and 0.848824. The reduction/increase in temperatures between hybrid levels 0.90 to 0.70 from the impact of the smoke plumes is similar to the findings of Saponaro et al. (2017). These changes air temperatures near the surface and decreases aloft (a stronger negative vertical gradient in temperature) implies a decrease in near-surface atmospheric stability associated with feedbacks, given that the overall temperature gradient from the surface has become more negative (that is, the ambient lapse rate has increased). Rising air parcels will follow an adiabatic lapse rate; these increases in the ambient lapse rate imply that rising air parcels will have an increasing tendency to be warmer than their environment. Feedbacks have thus reduced atmospheric stability within the forest fire smoke in the lowest part of the atmosphere; the atmosphere there has become more unstable. Meanwhile, the feedbacks decrease the environmental lapse rate further aloft above the forest fire smoke, between hybrid levels 0.848 and 0.339. Rising air parcels in this region following an adiabatic lapse rate will thus have an increasing tendency to be colder than their environment – the atmosphere above the smoke plumes has become more stable. This is echoed by the response of the concentration fields to the near-surface stability change, as can be seen through comparisons of the PM_{2.5}, NO₂ and O₃ surface concentrations changes (Figure 2122) and as vertical cross-sections (Figures 22, 23, 24, 25), respectively. Changes For all three surface fields, changes above the 90% confidence level for PM_{2.5} and NO₂ occur near the forest fires themselves (red regions, near top of model domain, Figure 2122(a,b)), though remain below e). The differences in particulate matter concentrations are also significant at the 90% confidence for O₃ level throughout the model domain (Figure 21(c)). 22(a)). Note that while the PM_{2.5} mean values are significantly different at the 90% confidence level throughout the model domain, the magnitude of those differences are sometimes small, particularly in the upper atmosphere, where the aerosol concentrations are relatively small. However, the regions with the larger magnitude regional differences in PM_{2.5} concentrations also occur at greater than the 90% confidence level (compare spatial locations of coloured regions in Figure 22(a,b) to red regions in Figure 22(e,d)). Feedbacks result in near-surface PM_{2.5} decreases in the regions downwind of the forest fires (Figure 2122(a), Figure 2223(a), note the large blue region and more intense blue region near surface in Figure 2223(a)), suggesting less PM_{2.5} mass is present near the surface due to the feedbacks. Given the increase in near-surface stability below

the fire plumes noted above, this ~~This could reflect a change in the vertical distribution probably reflects a injection height of the plumes in addition to other transport changes associated with the decrease in downward diffusive mixing of the forest fire plumes once aloft – the feedbacks thus have a tendency to increase the smoke plume concentrations aloft, by preventing the downward mixing of smoke injected by the fires. These atmospheric stability. Lower troposphere decreases in PM2.5 concentration effects rise above over the ocean and increases over the land at or greater than the 90% confidence level within the region closest to the fires. may also be seen (Figure 23(b,d)).~~

Feedbacks result in an increase in near-surface NO₂ in several inland urban centers and less NO₂ at surface level downwind (Figure 21 22(b), though these differences are only significant at the 90% confidence level within the forest fire plumes (Figure 21(e), Figure 23(24(a,c)). Ocean versus land NO₂ differences remain below the 90% confidence level.

Feedbacks decreased ~~lower Troposphere surface~~ O₃ near the forest fires (Figure 21 22(c), Figure 24 25(a)), while ~~decreasing~~ increasing O₃ ~~near above hybrid level 0.383 aloft.~~ The forest fires are also the only area where the differences in between mean ozone forecasts ~~approach have greater than the~~ 90% confidence.

Overall, the most significant effects of the feedbacks were: (1) ~~increases changes~~ in PM2.5 ~~aloft and decreases near concentrations throughout the surface in areas impacted by the fires model domain,~~ and (2) ~~increases changes~~ in NO₂ ~~aloft and decreases near the surface near the fires, to lesser extent than PM2.5, and (3) decreases in lower troposphere and O₃, particularly near the surface in the region impacted by the fires within the forest fire plumes.~~

The feedback-induced changes in primary and secondary pollutants in the forest fire regions are consistent with the decrease in atmospheric stability noted above – a greater proportion of the primary particulate matter and NO₂ resulting from near-surface forest fire emissions of NO ~~remain aloft are carried upwards~~ with the addition of feedbacks. The decrease in surface ozone and increase further aloft in the fire region (Figure 24 25(a)) spatially matches the ~~decrease changes in surface NO₂ (Figure 22 23(a)). Chemically,)~~ this ~~may imply implies~~ that the changes associated with feedbacks occur in NO_x-limited environments, i.e., with relatively high VOC/NO_x ratios, ~~since in these. In such~~ environments, decreases in NO_x emissions may lead to decreases in the rate of secondary O₃ formation. ~~Alternatively, the reduction in near-surface O₃ concentrations may reflect a decrease in light levels reaching the surface due to cloud attenuation (aerosol indirect effect), with the resulting lower photolysis rates resulting in a reduction in surface photochemical ozone production.~~

Our analysis thus suggests ~~a net~~ enhanced upward transport occurs in forest fire plumes due to feedbacks, and that this transport is linked to feedback-induced:

- (1) ~~Increases decreases~~ in local ~~near-surface~~ atmospheric stability, ~~reducing downward mixing of particulate plumes once aloft~~ (Figure 22 24(a));
- (2) ~~Increases increases~~ in cloud droplet numbers ~~throughout near the lower troposphere surface~~ (Figure 15 16(a)); and
- (3) ~~Increases increases~~ in rain drop numbers aloft (Figure 16 17(a)).

This combination suggests the presence of an AIE feedback loop – ~~increased lower atmosphere decreased~~ stability results ~~a greater proportion of particulate matter remaining aloft in higher forest fire plume rise,~~ in turn ~~resulting in lofting proportionally~~ more particles ~~remaining at~~ higher levels in the atmosphere where they may act as

Formatted: Indent: First line: 1.27 cm

cloud condensation nuclei, increasing cloud droplets aloft (Figure 1546(a)). This in turn results in increased lower middle troposphere cooling, through the 1st AIE (increase in cloud droplet numbers aloft leading to increased cloud albedo and cooling of the atmosphere below the cloud tops) while the corresponding decreases in particles and cloud condensation nuclei at lower levels results in a smaller near-surface impact on the AIE and ADE, hence relatively minor changes on near-surface temperatures (Figure 2024(a)). This combination maintains a feedback-induced near-surface unstable/less stable temperature gradient, relative to the no-feedback simulation employing aerosol property climatologies. We acknowledge that these changes in temperature fall below the 90% confidence level for the averages over all times, though note that differences in mean bias relative to observations for the two simulations became significantly different at specific times of day in the forecasts (Figure 6(a), hours 3, 6, 15 and 18, corresponding to 15, 18, 3 and 6 UT, or 9 AM, 12 noon, 9 PM, and midnight MDT), implying that the temperature changes at these specific times reach a higher level of significance. Similarly, Figures 12 and 13 show reductions in the near-surface temperature biases with the use of feedbacks.

~~Similarly, over the oceans, the feedback-induced decrease in surface PM2.5 (Figure 23(a)) is accompanied by lower middle troposphere cooling (Figure 24(b), note the dark blue band over ocean between hybrid levels 0.914 and 0.824), implying a decrease in stability. While aerosol increases aloft are not large, the lower level PM2.5 act as CCN, resulting in increased cloud formation and convection, in turn increasing cloud droplet and rain drop numbers aloft, which through the 1st AIE, maintains the slightly less stable temperature profile. We acknowledge that these changes in temperature fall below the 90% confidence level for the averages over all times, though note that differences in mean bias relative to observations for the two simulations became significantly different at specific times of day in the forecasts (Figure 6(a), hours 3, 6, 15 and 18, corresponding to 15, 18, 3 and 6 UT, or 9 AM, 12 noon, 9 PM, and midnight MDT), implying that the temperature changes at these specific times reach a higher level of significance.~~

4.3 Summary, Differences in Forecast Simulation-Period Averages

Relative to the no-feedback simulation employing an aerosol climatology, the AIE feedback as simulated here is associated with ~~increases/decreases~~ in near-surface stability over both ocean and forest-fire influenced land areas. Over oceans, near-surface particulate matter is removed as cloud condensation nuclei, resulting in increased cloud droplet numbers, maintaining the temperature gradient through the 1st aerosol indirect effect. In the vicinity of forest fires, ~~increases/decreases~~ in near-surface stability result in ~~more/increased transport of~~ PM2.5 remaining aloft, increasing the availability of cloud condensation nuclei aloft, increasing cloud droplet numbers aloft, hence also maintaining the less stable near-surface/increased temperature gradient through the 1st aerosol indirect effect. We note that the ADE may also play a weak role, particularly in the southern part of the domain, where lower atmosphere temperature gradient increases are not accompanied by significant changes in cloud droplet numbers (Figure 1546(a), southern half of the cross-section), but are accompanied by significant though small magnitude increases in PM2.5 in the lower atmosphere (Figure 2223(a), southern half of cross-section), and temperature profile changes (Figure 2024) below the 90% confidence level.

5 Conclusions

The work carried out here suggests that the answers to our two research questions (“Can on-line coupled models improve both air-quality and meteorological forecasts?” and “Are the changes in forest fire forecasts associated with implementing forest fire emissions within a on-line coupled model sufficient to significantly perturb weather and chemistry?”) are both a qualified “yes”. Within

~~The simulations analyzed here were conducted in preparation for an experimental forecast carried out as part of the FIREX-AQ campaign, and hence were limited by operational time constraints to a sequence of nested 24 hour forecasts. However, the high resolution domain size employed here, was sufficiently large to result in improvements or matching in weather forecast performance was seen for most times both surface and heights in the atmosphere, profile variables at greater than or above the 90% confidence level. Improvements in model performance for surface PM2.5, NO₂ and O₃ were also found, across most statistical measures (35 out of 48 statistical evaluation scores showed improvements). Comparing average vertical cross-sections, the chemical concentration changes associated with feedbacks were. The differences between feedback and no-feedback simulations occurred at or above the most significant close to 90% confidence level throughout the model domain for PM2.5, though were limited at the 90% confidence level for NO₂ and O₃ to the immediate vicinity of the forest fires in the northern portion of the domain. There, increased net vertical transport associated with decreased near-surface stability feedbacks lowered near-surface PM2.5 and NO₂ concentrations and increased them aloft, and resulted in reduced surface O₃ in the NOx-limited regions of the forest fire plume.~~

~~Our~~The simulations suggest that aerosol optical depth in the region, as well as the overall chemical performance of the model, was strongly influenced by upwind boundary conditions. AODs were biased low despite PM2.5 positive biases, suggesting that the homogeneous mixture approach for aerosol optical properties results in a general under-prediction of aerosol optical depths, in accord with Curci *et al.* (2015), and that obtaining better data for forest fire aerosol optical properties should be a priority for future study, as well as an examination of (2015), and external mixture approaches. Positive are recommended in further study. However, this general negative bias in simulated AOD is locally offset by positive biases in the region affected by vicinity of forest fires. This suggests that forest fire plumes have significantly different optical properties, and may be less hygroscopic, than industrial aerosols of comparable size. Special / separate treatment of forest fire CCN and optical properties are therefore also recommended in future work.

On-line Fully coupling forest fire plume rise calculations with the weather parameters was shown to have a significant impact on the height of primary pollutants reached by forest fires, the formation of near-surface ozone near the forest fires, and on particulate matter, throughout much of the three dimensional model domain. These changes were largely driven by the AIE, which maintains an increased lapse rate (decreased near-surface temperature gradient (reduced stability) over the forest-fire-influenced and oceanic portions of the region studied. Weak evidence for the influence of the ADE was shown in the southern part of the domain, where increases in particulate matter were also accompanied by decreases in stability between the surface and the lower-middle troposphere (the differences were at a lower than 90% confidence level for these comparisons of temperatures averaged over all model times).

Formatted: Font: Italic

Relative to the no-feedback aerosol climatology for CCN and aerosol optical properties, the simulations carried out here suggested that in the vicinity of forest fires feedbacks significantly increase cloud droplet ~~near the surface,~~ ~~increase cloud droplet~~ number densities near the surface and aloft, and significantly increase rain drop number densities aloft, relative to forecasts driven by climatological aerosol properties. Over the oceans, feedbacks decreased cloud droplet number density and increased rain drop number density aloft, relative to the simulation employing invariant CCN properties. ~~Oceanic cloud-~~ ~~Cloud~~ droplet mass increased to a lesser degree (with smaller regions above the 90% confidence level), as did rain drop mass (the mean differences for which for the most part remained below the 90% confidence level). This provides some evidence for a shift in atmospheric water mass associated with feedbacks from cloud water to rain over the oceans relative to the no-feedback climatology, though this shift occurred largely within the variability of the cloud fields within each simulation. Longer simulations may be needed to achieve higher confidence in this finding.

Data Availability

The datasets used here for model evaluation are available from the publicly accessible websites (AQS network) <https://www.epa.gov/aqs> and (NAPS network) <http://maps-cartes.ec.gc.ca/nspa-naps/data.aspx>.

Author Contribution

PAM: experiment design, conceptualization, analysis, writing of manuscript drafts; AA: model code and run script design and implementation, statistical analysis of model results, model analysis graphics; JC: forest fire emissions processing system design and coding, manuscript contributions, draft review and assistance; BP: forecast system simulations and design; WGWanmin Gong[†]: indirect effect updates, advice on P3 ~~implementation~~ implementation, manuscript contributions, manuscript review; CSCStroud: code version contributions, manuscript review; CSCStonis: AOD analysis, manuscript contributions and review; KS: forest fire emissions processing system design and coding, manuscript contributions and review; PC: forecast system simulations and design; JZ: emissions processing and input field assistance, manuscript review and contributions; J.M.: indirect effect updates and advice on implementing AIE in the P3 scheme, manuscript review and contributions.

Competing Interests

The authors declare that they have no conflict of interest.

References

- Abdul-Razzak, H., and Ghan, S.J.: A parameterization of aerosol activation. 3. Sectional representation, J. Geophys. Res. Atm., 107 (D3), <http://dx.doi.org/10.1029/2001JS000483>, 6 pp, 2002.
- Aggarwal, R., and Ranganathan, P., Common pitfalls in statistical analysis: the use of correlation techniques, Perspect. Clin. Res., 187-190, 2016.

971 Ahmadov, R., James, E., Grell, G., Alexander, C., Benjamin, S., McKeen, S., Pereira, G., Freitas, S., Csiszar, I.,
 972 Tsidulko, M., Kondragunta, S., Xu, C., Wong, K.Y., and Albers, S.: Forecasting smoke, visibility and smoke-
 973 weather interactions using a coupled meteorology-chemistry modeling system: Rapid Refresh and High-
 974 Resolution Rapid Refresh coupled with Smoke (RAP/HRRR-Smoke), EGU 2019 Conference presentation,
 975 Geophysical Research Abstracts, Vol. 21, EGU2019-18605, 2019.
 976 <https://meetingorganizer.copernicus.org/EGU2019/EGU2019-18605.pdf>, 2019.
 977 Akingunola, A., Makar, P.A., Zhang, J., Darlington, A., Li, S.-M., Gordon, M., Moran, M.D., and Zheng, Q.: A
 978 chemical transport model study of plume-rise and particle size distribution for the Athabasca oil sands, *Atm.*
 979 *Chem. Phys.*, 18, 8667-8688, 2018.
 980 Albrecht, B.A.: Aerosols, cloud microphysics, and fractional cloudiness, *Science*, 245(4923), 1227-1230,
 981 <https://doi.org/10.1126/science.245.4923.1227>, 1989.
 982 Baro, R., Palacios-Pena, L., Baklanov, A., Balzarini, A., Brunner, D., Forkel, R., Hirtl, M., Honzak, L., Perez, J.L.,
 983 Pirovano, G., San Jose, R., Schroder, W., Werhahn, J., Wolke, R., Zabhar, R., Jimenez-Guerrero, P.: Regional
 984 effects of atmospheric models on temperature: an evaluation of an ensemble of online coupled models, *Atm.*
 985 *Chem., Phys.*, 17, 9677-9696, 2017.
 986 Briggs, G.A.: A plume rise model compared with observations, *J. Air. Poll. Cont. Assoc.*, 15, 433-438,
 987 <https://doi.org/10.1080/000022470.1965.10468404>, 1965.
 988 Briggs, G.A.: Plume rise and buoyancy effects, atmospheric sciences and power production, in: DOE/TIC-
 989 27601(DE84005177), edited by Randerson, D., Technical Information Center, U.S. Dept. of Energy, Oak Ridge,
 990 TN, USA, 327-366, 1984.
 991 Carrera, M.L., Belair, S., Bilodeau, B.: The Canadian Land Data Assimilation System (CalDAS): description and
 992 synthetic evaluation study, *J. Hydrometeor.*, 16, 1293-1314, 2015.
 993 [Carslaw, D.C., and Ropkins, K., openair – An R package for air quality data analysis, *Env. Mod. Soft.*, vol. 27-28,](#)
 994 [pp 52-61, 2012.](#)
 995 Chen, J., Anderson, K., Pavlovic, R., Moran, M.D., Englefield, P., Thompson, D.K., Munoz-Alpizar, R., and Landry,
 996 H.: The FireWork v2.0 air quality forecast system with biomass burning emissions from the Canadian Forest
 997 Fire Emissions Prediction System v2.03, *Geosci. Model Dev.*, 12, 3283–3310, 2019.
 998 Clark, T.L., Coen, J. and Latham, D.: Description of a coupled atmosphere–fire model. *International Journal of*
 999 *Wildland Fire*, 13(1), pp.49-63, 2004.
 1000 Clark, T.L., Jenkins, M.A., Coen, J.L., Packham, D.R.: A coupled atmosphere-fire model: role of convective froude
 1001 number and dynamic engineering at the fireline, *Int. J. Wildland Fire*, 6, 177-190, 1996.
 1002 [Coen, J., Cameron, M., Michalakes, J., Patton, E., Riggan, P., and Yedinak, K., WRF-Fire: coupled weather-wildfire](#)
 1003 [modelling with the Weather Research and Forecasting Model, *J. Appl. Meteorol. Climatol.*, 52, 16-38, 2013.](#)
 1004 Côté, J., Gravel, S., Méthot, A., Patoine, A., Roch, M., Staniforth, A.: The operational CMC/MRB global
 1005 environmental multiscale (GEM) model. Part 1: design considerations and formulation. *Mon. Wea. Rev.*, 126,
 1006 1373-1395, 1998.

Curci, G., Hogrefe, C., Bianconi, R., Im, U., Balzarini, A., Baro, R., Brunner, D., Forkel, R., Giordano, L., Hirtl, M., Honzak, L., Jimenez-Guerrero, P., Knote, C., Langer, M., Makar, P.A., Pirovano, G., Perez, J.L., San Jose, R., Syrakov, D., Tuccella, P., Werhahn, J., Wolke, R., Zabkar, R., Zhang, J., and Galmarini, S.: Uncertainties of simulated aerosol optical properties induced by assumptions on aerosol physical and chemical properties: an AQMEII2 perspective, *Atm. Env.*, 115, 541-522, 2015.

Duveiller, G., Fasbender, D. and Meroni, M., Revisiting the concept of a symmetric index of agreement for continuous datasets, *Sci. Rep.*, 6, 19401; doi: 10.1038/srep19401, 2016.

Ezhova, E., Ylivinkka, I., Kuusk, J., Komsaare, K., Vana, M., Krasnova, A., Noe, S., Archinov, M., Belan, B., Park, S-B., Lavric, J.V., Heimann, M., Petaja, T., Vesala, T., Mammarella, I., Kolari, P., Back, J., Rannik, U., Kerminen, V.-M., and Kulmala, M.: Direct effect of aerosols on solar radiation and gross primary production in boreal and hemiboreal forests, *Atm. Chem. Phys.*, 18, 17863-17881, 2018.

Fox, D.G., Judging air quality model performance – a summary of the AMS workshop on dispersion model performance, *Bull. Am. Met. Soc.*, 62, 599-609, 1981.

Galmarini, S., Hogrefe, C., Brunner, D., Makar, P., Baklanov, A., Preface, *Atm. Env.*, 115, 340-344, 2015.

Geer, A.J.: Significance of changes in medium-range forecast scores, *Tellus A.*, 68, 30229, <http://dx.doi.org/10.3402/tellusa.v68.30229>, 2016.

Girard, C., Plante, A., Desgagne, M., McTaggart-Cowan, R., Cote, J., Charron, M., Gravel, S., Lee, V., Patoine, A., Qaddouri, A., Roch, M., Spacek, L., Tanguay, M., Vaillancourt, P.A., and Zadra, A.: Staggered vertical discretization of the Canadian Environmental Multiscale (GEM) model using a coordinate of the log-hydrostatic-pressure type. *Mon. Wea. Rev.*, 142, 1183–1196, 2014.

Gong, S.L., Barrie, L.A., Blanchet, J.-P., von Salzen, K., Lohmann, U., Lesins, G., Spacek, L., Zhang, L.M., Girard, E., Lin, H., Leaitch, R., Leighton, H., Chylek, P., Huang, P.: Canadian Aerosol Module: a size-segregated simulation of atmospheric aerosol processes for climate and air quality models. 1. Module development. *J. Geophys. Res.*, 108, 4007, <http://dx.doi.org/10.1029/2011JG002002>, 2003.

Gong, W., Beagley, S.R., Zhang, J., Cousineau, S., Chen, J., Sassi, M., Munoz-Alpizar, R., Morrison, H., Lyons, L., and Bellavance, P.: Modelling regional air quality in the Canadian Arctic: impact of North American wildfire and Arctic shipping emissions, in: *Air Pollution Modelling and Its Application, XXIV*, edited by Steyn, D.G. and Chaumerliac, N., Springer, Switzerland, 301-306, 2016.

Gong, W., Makar, P.A., Zhang, J., Milbrandt, J., Gravel, S., Hayden, K.L., Macdonald, A.M., Leaitch, W.R.: Modelling aerosol-cloud-meteorology interaction: a case study with a fully coupled air quality model (GEM-MACH), *Atm. Env.*, 115, 695-715, 2015.

Grell, G.A., and Freitas, S.R., A scale and aerosol aware stochastic convective parameterization for weather and air quality modelling, *Atmos. Chem. Phys.*, 14, 5233-5250, 2014.

Griffin, D., Sioris, C., Chen, J., Dickson, N., Kovachik, A., De Graaf, M., Nanda, S., Veefkind, P., Dammers, E., McLinden, C.A. and Makar, P., The 2018 fire season in North America as seen by TROPOMI: aerosol layer height intercomparisons and evaluation of model-derived plume heights. *Atmospheric Measurement Techniques*, 13(3): 1427-1427, 2020.

1044 [Hanna, S.R., Air quality model evaluation and uncertainty, J. Air Poll. Control Assoc., 38, 406-412, 1988.](#)

1045 Hoegh-Guldberg, O., Jacob, D., Taylor, M., Bindi, Brown, S., Camilloni, I., Diedhiou, A., Djalante, R., Ebi, K.L.,

1046 Engelbrecht, F., Guiot, J., Hijikata, Y., Mehrotra, S., Payne, A., Seneviratne, S.I., Thomas, A., Warren, R., and

1047 Zhou, G.: Impacts of 1.5°C Global Warming on Natural and Human Systems. In: *Global Warming of 1.5°C. An*

1048 *IPCC Special Report on the impacts of global warming of 1.5°C above pre-industrial levels and related global*

1049 *greenhouse gas emission pathways, in the context of strengthening the global response to the threat of climate*

1050 *change, sustainable development, and efforts to eradicate poverty* [Masson-Delmotte, V., Zhai, P., Pörtner, H.-

1051 O., Roberts, D., Skea, J., Shukla, P.R., Pirani, A., Moufouma-Okia, W., Péan, C., Pidcock, R., Connors, S.,

1052 Matthews, J.B.R., Chen, Y., Zhou, X., Gomis, M.I., Lonnoy, E., Maycock, T., Tignor, M., and Waterfield, T.

1053 (eds.)]. In Press, 2018.

1054 Inness, A., [Ades, M., Agusti-Panareda, Baier, F., Benedetti, A., Barre, J., Benedictow, A., Blechschmidt, A.-M.,](#)

1055 [Dominguez, J.J., Bouarar, I., Chabrillat, S., Clark, H., Clerbaux, C., Coheur, P., Engelen, R., Eskes, H.J., Ernst,](#)

1056 [Q., Flemming, J., George, M., Granier, C., Hadji-Lazaro, J., Huijnen, V., Hurtmans, D., Jones, L., Kipling, Z.,](#)

1057 [Massart, S., Parrington, M., Peuch, V.-H., Kaiser, J.W., Kapsomenakis, J., Lefever, K., Leitao, J., Razinger, M.,](#)

1058 [Remy, S., Schulz, M., and Richter, A., Schultz, M.G., Simmons, A.J., Suttie, M., Sten, O., Thepaut, J.-N.,](#)

1059 [Thouret, V., Vrekoussis, M., Zerefos, C., The CAMS-MACC team: The MACC reanalysis: an 8-yr data set of](#)

1060 [atmospheric composition, Atmos. Chem. Phys., 19, 3515-3556, 2019](#), [4073-4109,](#)

1061 [http://dx.doi.org/10.5194/acp-13-4703-2013, 2013.](#)

1062 James, E., Ahmadov, R., and Grell, G.: Realtime Wildfire Smoke Prediction in the United States: the HRRR-Smoke

1063 Model, in: EGU General Assembly Conference Abstracts, vol. 20 of EGU General Assembly Conference

1064 Abstracts, p. 19526, 2018

1065 Jiang, Y., Yang, X.-Q., and Liu, X., Seasonality in anthropogenic aerosol effects on East Asian climate simulated

1066 with CAM5, J. Geophys. Res. Atmos., 120, 10837-10861, doi:10.1002/2015JD023451, 2015.

1067 Jouan, C., J.A. Milbrandt, P. Vaillancourt, F. Chosson, H. Morrison: Adaptation of the Predicted Particles Properties

1068 (P3) microphysics scheme for large-scale numerical weather prediction. *Wea. Forecasting* (under review),

1069 2020.

1070 Jung, J., Souri, A.H., Wong, D., Lee, S., Jeon, W., Kim, J., Choi, Y.: The impact of the direct effect of aerosols on

1071 meteorology and air quality using aerosol optical depth simulation during the KORUS-AQ campaign, J.

1072 Geophys. Res. Atmos., 124, 8303-8319, [https://doi.org/10.1029/2019JD030641, 2019.](#)

1073 [Kochanski, A.K., Jenkins, M.A., Yedinak, K., Mandel, J., Beezley, J., and Lamb, B., Toward an integrated system](#)

1074 [for fire, smoke and air-quality simulations. Int. J. Wildland Fire, 25, 534-568, 2016.](#)

1075 [Kochanski, A.K., Malia, D.V., Fearon, M.G., Mandel, J., Souri, A.H., and Brown, T., Modelling wildfire smoke](#)

1076 [feedback mechanisms using a coupled fire-atmosphere model with a radiatively active aerosol scheme, J.](#)

1077 [Geophys. Res. Atmos., 124, 9099-9116, 2019.](#)

1078 [Krause, P., Boyle, D.P., Base, F., Comparison of different efficiency criteria for hydrological model assessment,](#)

1079 [Adv., Geosci., 5, 89-97, 2005.](#)

1080 Legates, D.R., and McCabe, G.J. Jr. Evaluating the use of “goodness-of-fit” measures in hydrologic and
1081 hydroclimatic model validation, Water Resources Res., 35, 233-241, 1999.

1082 Linn, R., Reisner, J., Colman, J.J. and Winterkamp, J.: Studying wildfire behavior using FIRETEC. International
1083 journal of wildland fire, 11(4), pp.233-246, 2002.

1084 Lu, Z., and Sokolik, I.N.: Examining the impact of smoke on frontal clouds and precipitation during the 2002 Yakutsk
1085 wildfires using the WRF-Chem-SMOKE model and satellite data, J. Geophys. Res. Atm., 122, 12765-12785,
1086 <https://doi.org/10.1002/2017JD027001>, 2017.

1087 Luig, A., Bofinger, S., Beyer, H.G.: Analysis of confidence intervals for the prediction of regional wind power
1088 output, Proc. European Wind Energy Conference, Copenhagen, pp 725-728, 2001. Available at
1089 [https://www.researchgate.net/publication/228793040_Analysis_of_confidence_intervals_for_the_prediction_o](https://www.researchgate.net/publication/228793040_Analysis_of_confidence_intervals_for_the_prediction_of_regional_wind_power_output)
1090 [f_regional_wind_power_output](https://www.researchgate.net/publication/228793040_Analysis_of_confidence_intervals_for_the_prediction_of_regional_wind_power_output), last accessed August 23, 2020.

1091 Makar, P.A., Gong, W., Milbrandt, J., Hogrefe, C., Zhang, Y., Curci, G., Zabkar, R., Im, U., Balzarini, A., Baro, R.,
1092 Bianconi, R., Cheung, P., Forkel, R., Gravel, S., Hirtl, H., Honzak, L., Hou, A., Jimenez-Guerrero, P., Langer,
1093 M., Moran, M.D., Pabla, B., Perez, J.L., Pirovano, G., San Jose, R., Tuccella, P., Werhahn, J., Zhang, J.,
1094 Galmarini, S.: Feedbacks between air pollution and weather, part 1: Effects on weather. Atmospheric
1095 Environment, 115, 442-469, 2015a.

1096 Makar, P.A., Gong, W., Hogrefe, C., Zhang, Y., Curci, G., Zabkar, R., Milbrandt, J., Im, U., Balzarini, A., Baro, R.,
1097 Bianconi, R., Cheung, P., Forkel, R., Gravel, S., Hirtl, H., Honzak, L., Hou, A., Jimenez-Guerrero, P., Langer,
1098 M., Moran, M.D., Pabla, B., Perez, J.L., Pirovano, G., San Jose, R., Tuccella, P., Werhahn, J., Zhang, J.,
1099 Galmarini, S.: Feedbacks between air pollution and weather, part 2: Effects on chemistry. Atmospheric
1100 Environment, 115, 499-526, 2015b.

1101 Makar, P.A., Moran, M.D., Schultz, M.T., Taylor, A.: Speciation of volatile organic compound emissions for
1102 regional air quality modeling of particulate matter and ozone, J. Geophys. Res., 108,D2, 4041,
1103 doi:1029/2001JD000797, 2003.

1104 Makar, P.A., Staebler, R.M., Akingunola, A., Zhang, J., McLinden, C., Kharol, S.K., Pabla, B., Cheung, P. and
1105 Zheng, Q.: The effects of forest canopy shading and turbulence on boundary layer ozone, Nature
1106 Communications, 8, art. no. 15243, doi: 10.1038/ncomms15243, 2017.

1107 Makar, P.A., Stroud, C., Akingunola, A., Zhang, J., Ren, S., Cheung, P., and Zheng, Q.: Vehicle induced turbulence
1108 and atmospheric pollution, Proceedings of the National Academy of Sciences of the USA (under review), 2020.

1109 Mallet, M., Solmon, F., Roblou, L., Peers, F., Turquety, S., Waquet, F., Jethva, H., Torres, O.: Simulation of optical
1110 properties and direct and indirect radiative effects of smoke aerosols over marine stratocumulus clouds during
1111 summer 2008 in California with the regional climate model RegCM, J. Geophys. Res. Atm., 122, 10312-10337,
1112 <https://doi.org/10.1002/2107JD026905>, 2017.

1113 Mandel, J., Beezley, J.D., Kochanski, A.K., Coupled atmosphere-wildland fire modelling with WRF 3.3 and SFIRE
1114 2011, Geosci. Model Dev., 4, 591-610, 2011.

1115 Markowicz, K.M., Pakszys, R., Ritter, C., Zielenski, T., Udisti, R., Cappelletti, D., Mazzola, M., Shobara, M., Xian,
1116 P., Zawadzka, O., Lisok, J., Petelski, T., Makuch, P., Karasinski, G.: Impact of North American intense fires on

1117 aerosol optical properties measured over the European Arctic in July 2015, *J. Geophys. Res. Atm.*, 121, 14487-
 1118 14512, doi:10.1002/2016JD025310, 2016.

1119 Milbrandt, J.A. and Morrison, H.: Parameterization of Cloud Microphysics Based on the Prediction of Bulk Ice
 1120 Particle Properties. Part III: Introduction of Multiple Free Categories. *J. Atmos. Sci.*, 73, 975-995, doi:
 1121 <https://doi.org/10.1175/JAS-D-15-0204.1>, 2016.

1122 Milbrandt, J. A., S. Bélair, S., Faucher, M., Vallée, M., Carrera, M.L., and Glazer, A.: The pan-Canadian High
 1123 Resolution (2.5 km) Deterministic Prediction System. *Wea. Forecasting*, 31, 1791-1816, 2016.

1124 Milbrandt, J.A., and Yau, M.K.: A multimoment bulk microphysics parameterization. Part I: analysis of the role of
 1125 the spectral shape parameter, *J. Atmos. Sci.*, 62, 3051-3064, 2005a.

1126 Milbrandt, J.A., and Yau, M.K.: A multimoment bulk microphysics parameterization. Part II: a proposed three-
 1127 moment closure and scheme, *J. Atmos. Sci.*, 62, 3065-3081, 2005b.

1128 Moran, M.D., Pavlovic, R., and Anselmo, D.: Regional air quality deterministic prediction system (RAQDPS):
 1129 update from version 019 to version 020, Montreal, available at:
 1130 [http://collaboration.cmc.ec.gc.ca/cmc/CMOI/product_guide/docs/tech_note/technote_raqdps-](http://collaboration.cmc.ec.gc.ca/cmc/CMOI/product_guide/docs/tech_note/technote_raqdps-v2.0_20180918_e.pdf)
 1131 [v2.0_20180918_e.pdf](http://collaboration.cmc.ec.gc.ca/cmc/CMOI/product_guide/docs/tech_note/technote_raqdps-v2.0_20180918_e.pdf), last access: 1 December 2018.

1132 Morrison, H., and Milbrandt, J.A.: Parameterization of Cloud Microphysics Based on the Prediction of Bulk Ice
 1133 Particle Properties. Part I: Scheme Description and Idealized Tests. *J. Atmos. Sci.*, 72, 287-311, doi:
 1134 <https://doi.org/10.1175/JAS-D-14-0065.1>, 2015.

1135 Morrison, H. and W. W. Grabowski, W.W.: Modeling supersaturation and subgrid-scale mixing with two-moment
 1136 warm bulk microphysics. *J. Atmos. Sci.*, 65, 792-812, doi: <https://doi.org/10.1175/2007JAS2374.1>, 2008.

1137 Myhre, G., Shindell, D., Bréon, F.-M., Collins, W., Fuglestad, J., Huang, J., Koch, D., Lamarque, J.-F., Lee, D.,
 1138 Mendoza, B., Nakajima, T., Robock, A., Stephens, G., Takemura, T. and Zhang, H.: Anthropogenic and
 1139 Natural Radiative Forcing. In: *Climate Change 2013: The Physical Science Basis. Contribution of Working*
 1140 *Group I to the Fifth Assessment Report of the Intergovernmental Panel on Climate Change* [Stocker, T.F., D.
 1141 Qin, G.-K. Plattner, M. Tignor, S.K. Allen, J. Boschung, A. Nauels, Y. Xia, V. Bex and P.M. Midgley (eds)].
 1142 Cambridge University Press, Cambridge, United Kingdom and New York, USA, 2013.

1143 Nazarenko, L., Rind, D., Tsigaridis, K., Del Genio A.D, Kelly, M., and Tausnev, N.: Interactive nature of climate
 1144 change and aerosol forcing, *J. Geophys. Res. Atm.*, 122, 3457-3480, doi:10.1002/2016JD025809, 2017.

1145 Oeropoulos, L., Cho, N., and Lee, D.: A global survey of apparent aerosol-cloud interaction signals, *J. Geophys. Res.*
 1146 *Atm.*, 125, e2019JD031287, <https://doi.org/10.1029/2019JD031287>, 21 pp, 2020.

1147 O'Neill, N.T., Eck, T.G., Holben, B.N., Smimov, A., Royer, A., and Li, Z.: Optical properties of boreal forest fire
 1148 smoke derived from Sun photometry, *J. Geophys. Res.*, 107, 4125, doi 10.1029/2001JD000877, 21 pp., 2002

1149 Palacios-Pena, L., Baro, R., Baklanov, A., Balzarini, A., Brunner, D., Forkel, R., Hirtl, M., Honzak, L., Lopez-
 1150 Romero, J.M., Motavez, J.P., Perez, J.L., Pirovano, G., San Jose, R., Schroder, W., Werhahn, J., Wolke, R.,
 1151 Zabkar, R., and Jimenez-Guerrero, P.: An assessment of aerosol optical properties from remote-sensing
 1152 observations and regional chemistry-climate coupled models over Europe, *Atm. Chem. Phys.*, 18, 5021-5043,
 1153 2018.

1154 Pan, L., Kim, H. C., Lee, P., Saylor, R., Tang, Y., Tong, D., Baker, B., Kondragunta, S., Xu, C., Ruminski, M. G.,
 1155 Chen, W., McQueen, J., and Stajner, I.: Evaluating a fire smoke simulation algorithm in the National Air Quality
 1156 Forecast Capability (NAQFC) by using multiple observation data sets during the Southeast Nexus (SENEX)
 1157 field campaign, *Geosci. Model Dev. Discuss.*, <https://doi.org/10.5194/gmd-2017-207>, 2017.
 1158 Pavlovic, R., Chen, J., Anderson, K., Moran, M.D., Beaulieu, P.A., Davignon, D. and Cousineau, S.: The FireWork
 1159 air quality forecast system with near-real-time biomass burning emissions: Recent developments and evaluation
 1160 of performance for the 2015 North American wildfire season. *Journal of the Air & Waste Management*
 1161 *Association*, 66(9), 819-841, 2016.
 1162 Peace, M., Mattner, T., Mills, G., Kepert, J., and McCaw, L., Fire-modified meteorology in a coupled fire-
 1163 atmosphere model, *J. App. Met. and Clim.*, 54, 704-720, 2015.
 1164 Penner, J.E, Zhou, C., Gamier, A., Mitchell, D.L.: Anthropogenic aerosol indirect effects in cirrus clouds, *J.*
 1165 *Geophys. Res. Atm.*, 123, 11652-11677, <https://doi.org/10.1029/2018JD029204>, 2018.
 1166 Pinson, P., and Kariniotakis, G.: On-line adaptation of confidence intervals based on weather stability for wind power
 1167 forecasting, in *Proc. Of the Global Wind Power Conference*, Chicago, USA, 2004. Available at [https://hal-](https://hal-mines-paristech.archives-ouvertes.fr/hal-00529488/document)
 1168 [mines-paristech.archives-ouvertes.fr/hal-00529488/document](https://hal-mines-paristech.archives-ouvertes.fr/hal-00529488/document), last accessed August 23, 2020.
 1169 Pinto, J. O., Grim, J.A., Steinter, M.: Assessment of the High-Resolution Rapid Refresh model's ability to predict
 1170 mesoscale convective systems using object-based evaluation. *J. Atmos. Sci.*, 30, 892-913, 2015.
 1171 Rothenberg, D., Avramov, A., Wang, C.: On the representation of aerosol activation and its influence on model-
 1172 derived estimates of the aerosol indirect effect, *Atm. Chem. Phys.*, 18, 7961-7983, 2018.
 1173 Sandu, A. and Sander, R.: Technical note: Simulating chemical systems in Fortran90 and Matlab with the Kinetic
 1174 PreProcessor KPP-2.1, *Atmos. Chem. Phys.*, 6, 187–195, <https://doi.org/10.5194/acp-6-187-2006>, 2006
 1175 Saponaro, G., Kolmonen, P., Sogacheva, L., Rodriguez, E., Virtanen, T., and de Leeuw, G.: Estimates of the aerosol
 1176 indirect effect over the Baltic Sea region derived from 12 years of MODIS observations, *Atm. Chem. Phys.*, 17,
 1177 3133-3143, 2017.
 1178 Seity, Y., Brousseau, P., Malardel, S., Hello, G., Bénard, P., Bouttier, F., Lac, C., and Masson, V.: The AROME-
 1179 France convective-scale operational model. *Mon. Wea. Rev.*, 139, 876-913, 2010.
 1180 Stockwell, W.R. and Lurmann, F.W.: Intercomparison of the ADOM and RADM gas-phase chemical mechanisms,
 1181 Electric Power Institute Topical Report, Electric Power Institute, Palo Alto, California, 323pp, 1989.
 1182 Stroud, C.A., Makar, P.A., Zhang, J., Moran, M.D., Akingunola, A., Li, S.-M., Leithead, A., Hayden, K., Siu, M.:
 1183 Improving air quality model predictions of organic species using measurement-derived organic gaseous and
 1184 particle emissions in a petrochemical-dominated region. *Atmospheric Chemistry and Physics*, 18 (18), pp.
 1185 13531-13545, 2018.
 1186 Sundqvist, H.: Parameterization of condensation and associated clouds in models for weather prediction and general
 1187 circulation simulation. In: Schlesinger M.E. (eds) *Physically-Based Modelling and Simulation of Climate and*
 1188 *Climatic Change*. NATO ASI Series (Series C: Mathematical and Physical Sciences), vol 243. Springer,
 1189 Dordrecht, 1988.

1190 Suzuki, K, and Takemura, T.: Perturbations to global energy budget due to absorbing and scattering aerosols, *J.*
 1191 *Geophys. Res. Atm.*, 124, 2194-2209, <https://doi.org/10.1029/2018JD029808>, 2019.
 1192 Takeishi, A., Strövelmo, T., and Fierce, L.: Disentangling the microphysical effects of fire particles on convective
 1193 clouds through a case study, *J. Geophys. Res. Atm.*, doi:10.1029/2019JD031890, 2020.
 1194 Twomey, S.: The influence of pollution on the shortwave albedo of clouds, *J. Atmos. Sci.*, 34, 1149-1152, 1977.
 1195 Wang, J., Allen, D.J., Pickering, K.E., Li, Z., and He, H.: Impact of aerosol direct effect on East Asian air quality
 1196 during the EAST-AIRE campaign, *J. Geophys. Res. Atm.*, 121, 6534-6554, doi: 10.1002/2016JD025108, 2016.
 1197 Whaley, C.H., Makar, P.A., Shephard, M.W., Zhang, L., Zhang, J., Zheng, Q., Akingunola, A., Wentworth, G.R.,
 1198 Murphy, J.G., Kharol, S.K., and Cady-Periera, K.E.: Contributions of natural and anthropogenic sources to
 1199 ambient ammonia in the Athabasca oil sands and north-western Canada, *Atm. Chem. Phys.*, 18, 2011-2034,
 1200 2018.
 1201 [Willmott, C.J., Robeson, S.M., Matsuura, K., A refined index of model performance, *Int. J. Climatol.*, 32, 2088-](#)
 1202 [2094, 2012.](#)
 1203 [Yu, S., Eder, B., Dennis, R., Chu, S.-H., Schwartz, S.E., New unbiased metrics for evaluation of air quality models,](#)
 1204 [*Atmos. Sci. Lett.*, 7, 26-34, 2006.](#)
 1205 Zhang, L., Brook, J.R., and Vet., R.: A revised parameterization for gaseous dry deposition in air-quality models,
 1206 *Atm. Chem. Phys.*, 3, 2067-2082, <https://doi.org/10.5194/acp-3-2067-2003>, 2003.
 1207 Zhao, X., Liu, Y., Yu, F., and Heidinger, A.K.: Using long-term satellite observations to identify sensitive regimes
 1208 and active regions of aerosol indirect effects for liquid clouds over global oceans, *J. Geophys. Res. Atm.*, 123,
 1209 457-472, <https://doi.org/10.1002/2017JD027187>, 2018.
 1210 Zhu, J., and Penner, J.E.: Indirect effects of secondary organic aerosol on cirrus clouds, *J. Geophys. Res. Atm.*, 125,
 1211 e2019JD032233, <https://doi.org/10.1029/2019JD032233>, 19 pp., 2020.
 1212
 1213

1214 **Tables:**

1215

<u>Model Process or Configuration Component</u>	<u>Description</u>	<u>Reference (where applicable)</u>
<u>Base weather forecast model</u>	<u>Global Environmental Multiscale (GEM), v4.9.8</u>	<u>Cote <i>et al.</i> (1998), Girard <i>et al.</i> (2014)</u>
<u>Base air-quality model</u>	<u>Global Environmental Multiscale – Modelling Air-quality and Chemistry (GEM-MACH) v2</u>	<u>Moran <i>et al.</i> (2018)</u>
<u>Aerosol Direct Effect</u>	<u>Feedback simulations: GEM-MACH's predicted aerosol loading and Mie scattering using a binary water-dry aerosol homogeneous mixture assumption, at 4 wavelengths employed by GEM's radiative transfer algorithms, and at additional wavelengths for diagnostic purposes.</u> <u>No-Feedback simulations: invariant climatological values for aerosol optical properties are used.</u>	<u>Makar <i>et al.</i> (2015a,b)</u>
<u>Aerosol Indirect Effect</u>	<u>Feedback simulations: Modified P3 cloud microphysics scheme, driven by an aerosol size and speciation specific nucleation scheme (Abdul-Razzak and Ghan, 2002).</u> <u>No-feedback implementation: P3 scheme driven by an invariant aerosol population of a single lognormal size distribution (with a geometric mean diameter of 100 nm and total aerosol number of 300 cm⁻³ consisting of pure ammonium sulphate).</u> <u>The prognostic cloud droplet number and mass mixing ratios from the P3 microphysics are then transferred back to the chemistry module for using in cloud processing of gases and aerosols (cloud scavenging and chemistry) calculations, completing the AIE feedback process loop in the case of the feedback implementation (Gong <i>et al.</i>, 2015).</u>	<u>Gong <i>et al.</i> (2015), Abdul-Razzak and Ghan (2002), Morrison and Milbrandt (2015), Milbrandt and Morrison (2016), Morrison and Grabowski (2008).</u>
<u>Forest fire plume rise</u>	<u>CFFEPSv4.0 (see text)</u>	

<u>Gas-phase chemistry mechanism</u>	<u>ADOMII mechanism, 42 gas species.</u>	<u>Stockwell <i>et al.</i> (1989)</u>
<u>Gas-Phase chemistry solver</u>	<u>KPP-generated RODAS3 solver</u>	<u>Sandu and Sander (2006)</u>
<u>Cloud processing of aerosols</u>	<u>Aqueous chemistry, scavenging of gases and aerosols, below-cloud removal and wet deposition.</u>	<u>Gong <i>et al.</i> (2015)</u>
<u>Particle microphysics</u>	<u>Sectional size distribution and 8 chemical species.</u>	<u>Gong <i>et al.</i> (2003)</u>
<u>Particle inorganic thermodynamics</u>	<u>Local equilibrium subdomain approach</u>	<u>Makar <i>et al.</i> (2003)</u>
<u>Secondary organic aerosol formation</u>	<u>Modified yield approach</u>	<u>Stroud <i>et al.</i> (2018)</u>
<u>Vertical diffusion</u>	<u>Fully implicit approach, with surface fluxes as a boundary condition</u>	
<u>Advection</u>	<u>Semi-Lagrangian approach, 3-shell mass conservation correction (ILMC approach)</u>	
<u>Forest canopy shading and turbulence.</u>	<u>Light attenuation within forest canopies and turbulence reductions due to vegetation applied to thermal coefficients of diffusivity.</u>	<u>Makar <i>et al.</i> (2017)</u>
<u>Anthropogenic plume rise</u>	<u>Parameterization calculating residual buoyancy of the rising plume.</u>	<u>Akingunola <i>et al.</i> (2018).</u>
<u>Meteorological modulation of aerosol crustal material</u>	<u>Aerosol crustal material is inhibited when the soil water content is > 10%.</u>	
<u>Ammonia emissions and deposition</u>	<u>Bi-directional flux parameterization employed.</u>	<u>Whaley <i>et al.</i> (2018), Zhang <i>et al.</i> (2003).</u>
<u>Methane treatment</u>	<u>Reactive, emitted and transported tracer</u>	
<u>Leaf Area Index data</u>	<u>MODIS retrievals used to create monthly LAI values for biogenic emissions, forest canopy shading and turbulence, deposition</u>	

Vehicle-induced turbulence	Observation-based parameterization used to modify near-surface coefficients of thermal diffusivity	Makar <i>et al.</i> (2020)
--	--	--

Table 1. GEM-MACH model configuration details and references.

Event Forecast	Event Observed	
	Yes	No
Yes	A	B
No	C	D

Table 24. Event versus non-event contingency table. A = number of events forecast and observed; B=number of events forecast but not observed; C=number of events observed but not forecast; D = number of cases where events were neither forecast nor observed.

Table 2. Summary performance metrics for ozone, nitrogen dioxide, and PM2.5. Bold-face indicates the simulation with the better performance score for the given metric, chemical species and sub-region. Italic indicates a tied score, and regular font the simulation with the lower performance score. FO2: fraction of scores within a factor of 2. MB: Mean Bias. MGE: Mean Gross Error. R: Correlation Coefficient. RMSE: Root Mean Square Error. COE: Coefficient of Error. IOA: Index of Agreement.

[illegible]

		Western USA	No Feedback	0.493	0.346	2.3412	0.57275	0.6535	3.67494	0.1774	0.5884
				428	669	78	9	85	7	6+	19
			Feedback	0.483	0.427	2.3322	0.57074	0.6515	3.65785	0.1804	0.5904
				427	578	4	6	81	8	41	29

1230

1231 **Table 3: Summary performance metrics for ozone, nitrogen dioxide, and PM2.5. Bold-face indicates the simulation with**
1232 **the better performance score for the given metric, chemical species and sub-region, italics indicate a tied score, and regular**
1233 **font the simulation with the lower performance score. FO2: fraction of scores within a factor of 2. MB: Mean Bias. MGE:**
1234 **Mean Gross Error. NMGE: Normalized Mean Gross Error. R: Correlation Coefficient. RMSE: Root Mean Square**
1235 **Error. COE: Coefficient of Error. IOA: Index of Agreement.**

Formatted: Font: +Body (Times New Roman), (Int'l) Calibri, Kern at 12 pt

Formatted: Font: +Body (Times New Roman), Bold, Font color: Text 1, (Int'l) Calibri, Kern at 12 pt

Formatted: Font: +Body (Times New Roman), (Int'l) Calibri, Kern at 12 pt

Formatted: Font: +Body (Times New Roman), (Int'l) Calibri, Kern at 12 pt

Formatted: Font: +Body (Times New Roman), Font color: Text 1, (Int'l) Calibri, Kern at 12 pt

Formatted: Font: +Body (Times New Roman), (Int'l) Calibri, Kern at 12 pt

Formatted: Font: +Body (Times New Roman), Font color: Text 1, (Int'l) Calibri, Kern at 12 pt

Formatted: Font: +Body (Times New Roman), Font color: Text 1, (Int'l) Calibri, Kern at 12 pt

Formatted: Font: Bold

Formatted: Font: Bold

Formatted: Font: Bold

Formatted: Font color: Text 1

Formatted: Font color: Text 1

Formatted: Font: +Body (Times New Roman)

Formatted: Font: +Body (Times New Roman), Not Bold

Formatted: Font: +Body (Times New Roman)

Formatted: Font: +Body (Times New Roman)

Formatted: Font: +Body (Times New Roman)

Formatted: Font: +Body (Times New Roman)

Formatted: Font: +Body (Times New Roman)

Formatted: Font: +Body (Times New Roman), 10 pt

Formatted: Font: +Body (Times New Roman), 10 pt

Formatted: Font: +Body (Times New Roman), 10 pt, Bold

Formatted: Font: +Body (Times New Roman), 10 pt, Bold

Formatted: Font: +Body (Times New Roman), 10 pt

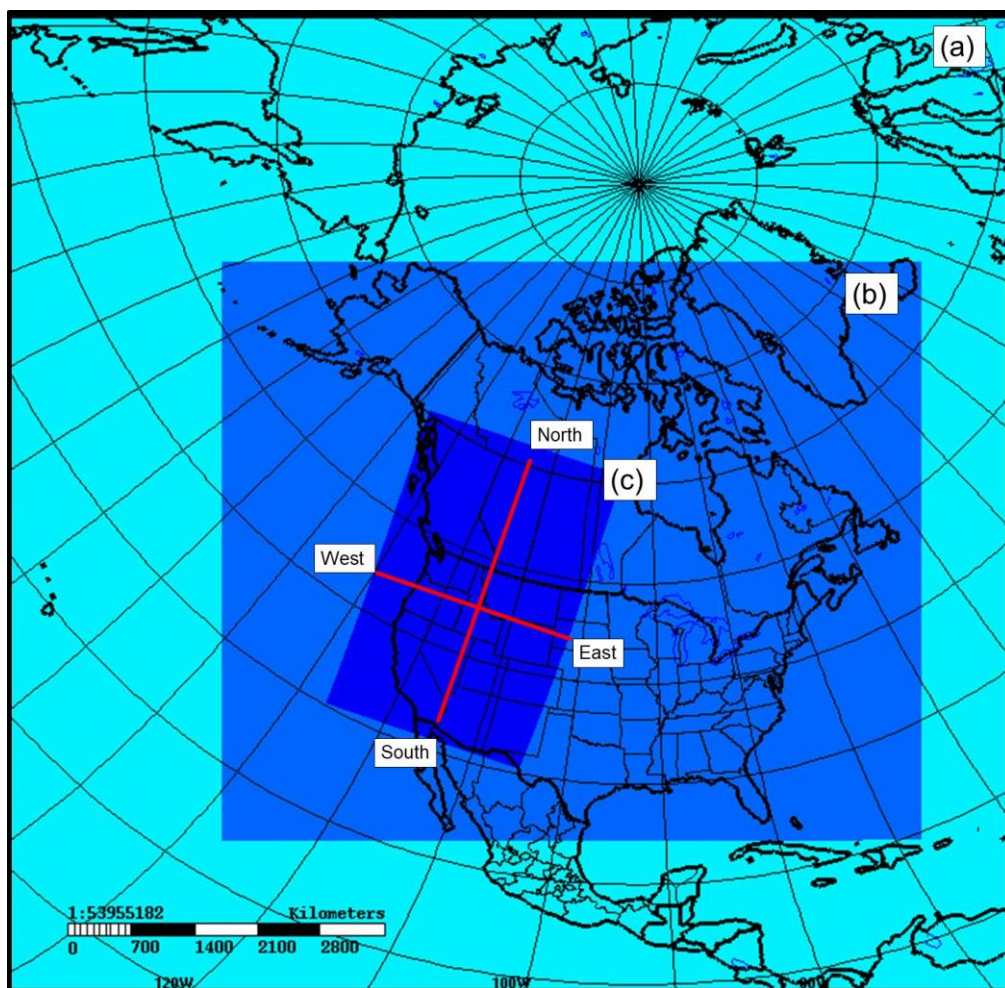
Formatted: Font: +Body (Times New Roman), 10 pt, Bold

Formatted: Font: +Body (Times New Roman), 10 pt, Bold

Formatted: Font: +Body (Times New Roman), 10 pt, Bold

Formatted: Line spacing: single

Figures:



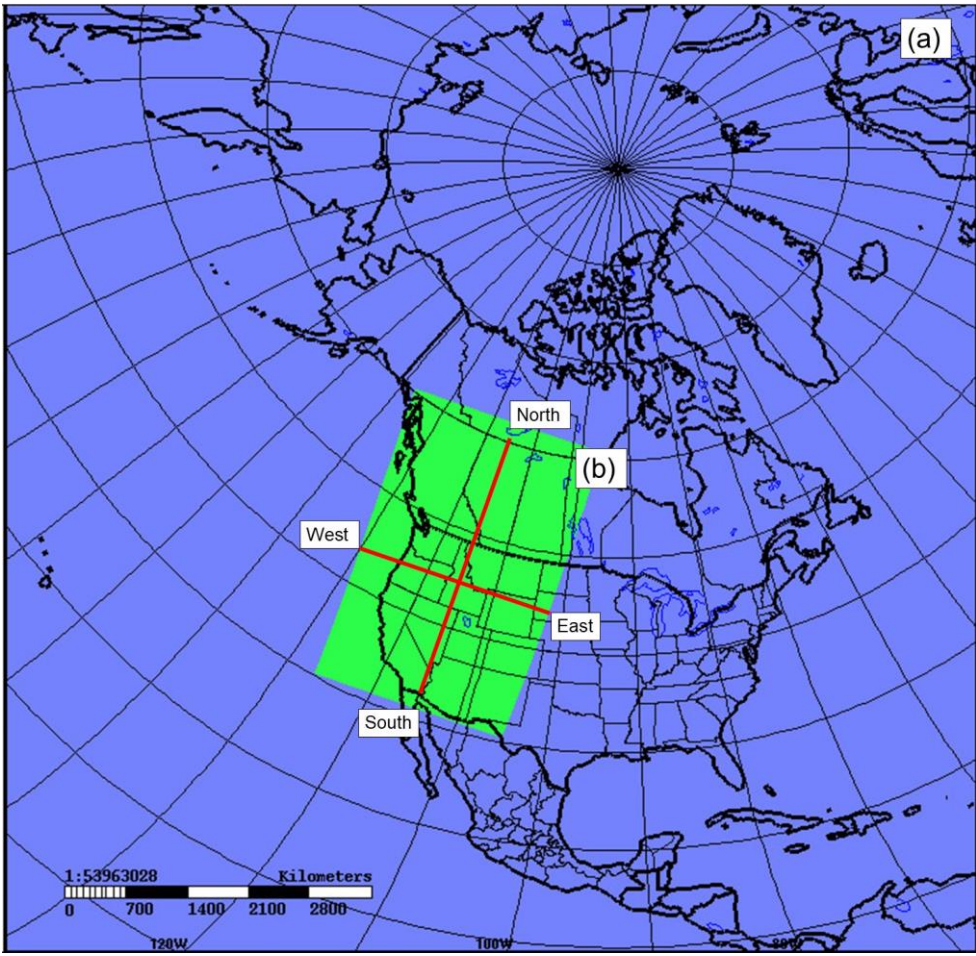


Figure 1: GEM-MACH domains: (a) Operational GEM meteorology 10km resolution forecast domain. (b) GEM-MACH 10km resolution experimental 2.5 km grid cell size forecast domain. (c) GEM-MACH inner 2.5 km grid resolution forecast domain for comparison to observations, used here. Red lines indicate locations of illustrative South to North and West to East cross-sections appearing in subsequent analysis in the text.

Formatted: English (Canada)

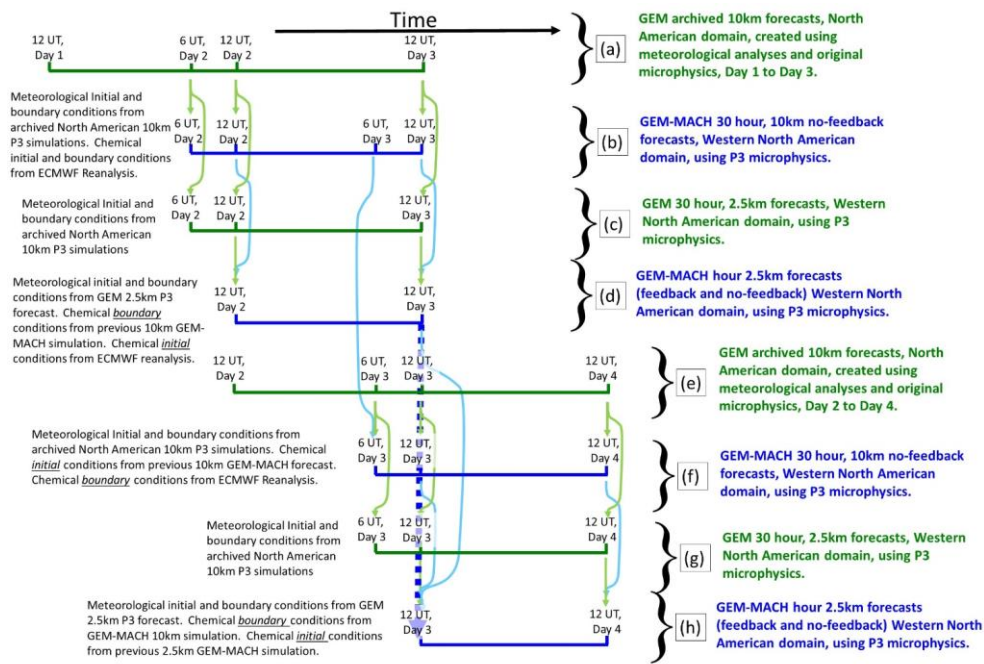
Formatted: English (Canada)

Formatted: English (Canada)

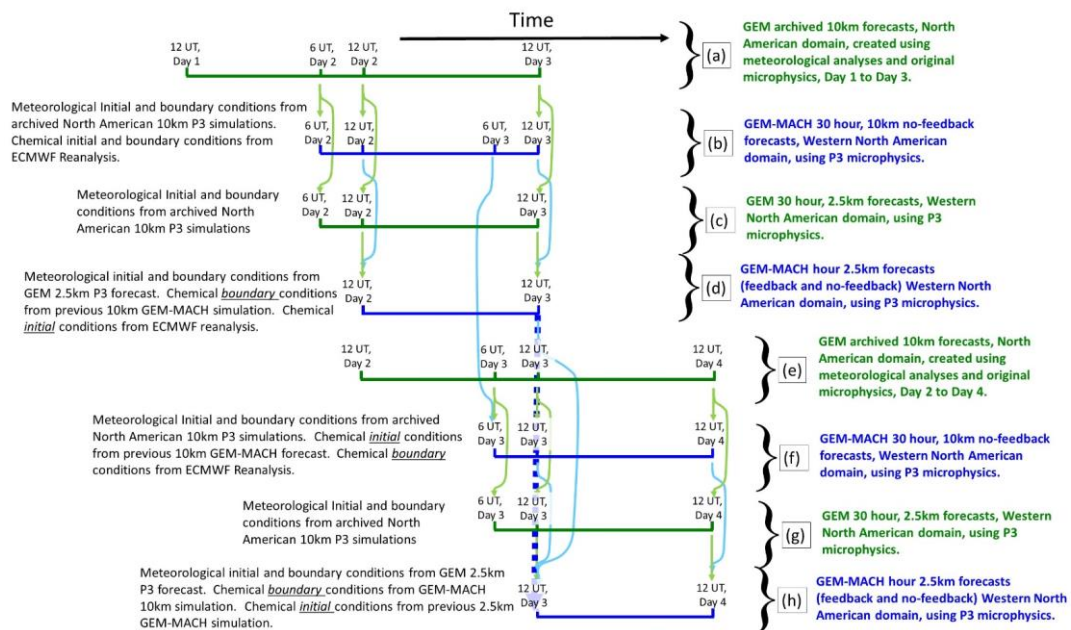
Formatted: English (Canada)

Formatted: English (Canada)

Formatted: Font: 9 pt, Bold, English (Canada)



Formatted: English (Canada)



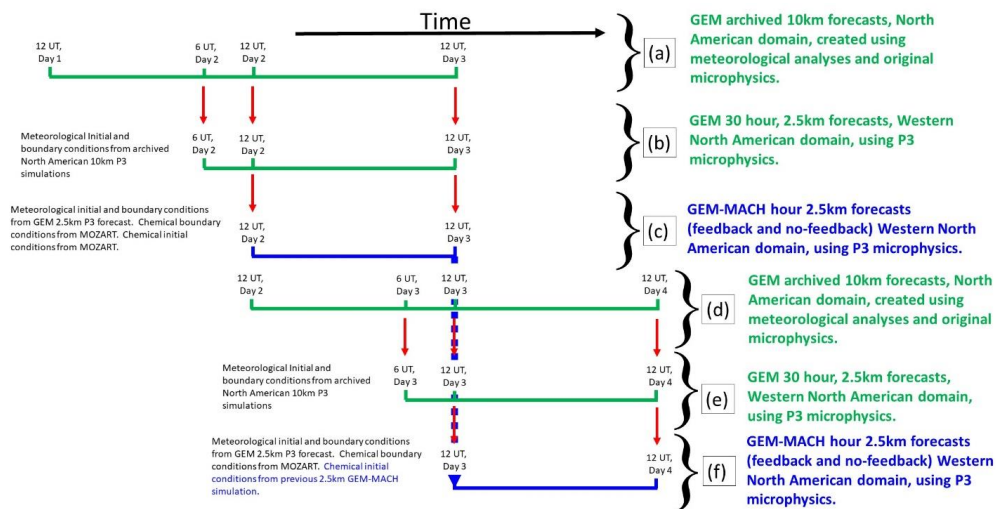


Figure 2: Example time sequencing of model simulations used to generate the 2.5-km GEM-MACH simulations carried out here. Green lines and print indicate GEM (weather forecast only) simulations), blue lines and print indicate 2.5-km GEM-MACH simulations. Arrows indicate data flow (light green: meteorological information; light blue: chemical information). Steps (a) through (f) illustrate the sequence of forecasts used to generate two consecutive days of 2.5km GEM-MACH simulations. Note that on-line coupling occurs only at the 2.5km GEM-MACH forecast level, in this sequencing.

Formatted: Font: 9 pt, Bold

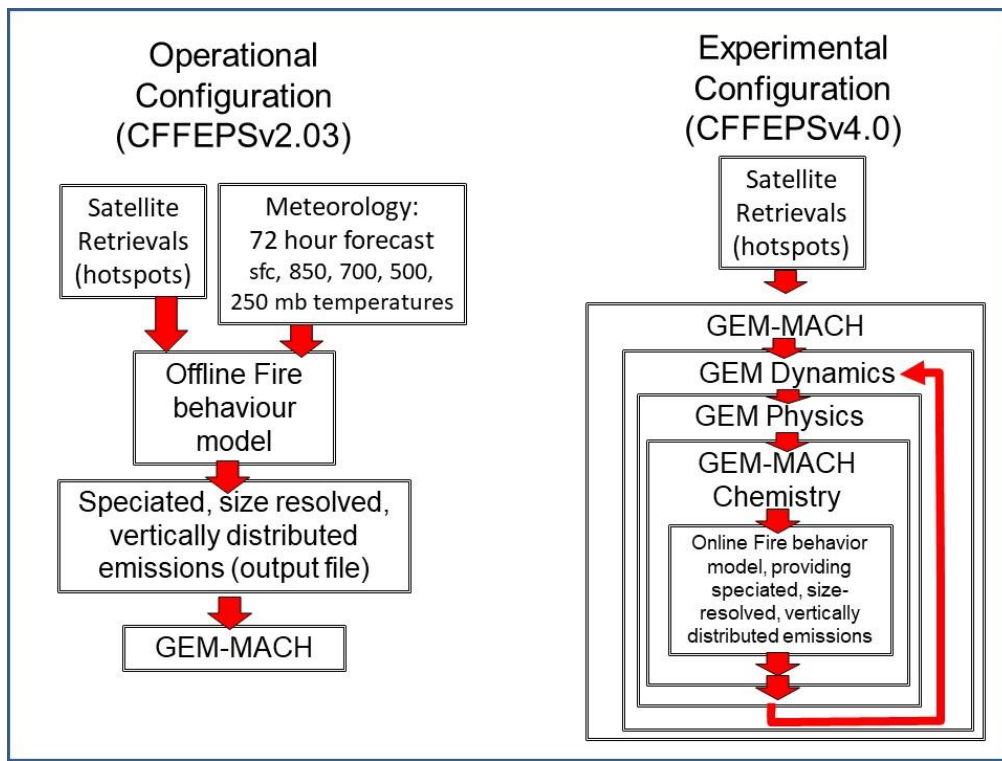
Formatted: Font: 9 pt, Bold, English (Canada)

Formatted: Font: 9 pt, Bold, English (Canada)

Formatted: Font: 9 pt, Bold, English (Canada)

Formatted: English (Canada)

Formatted: Normal



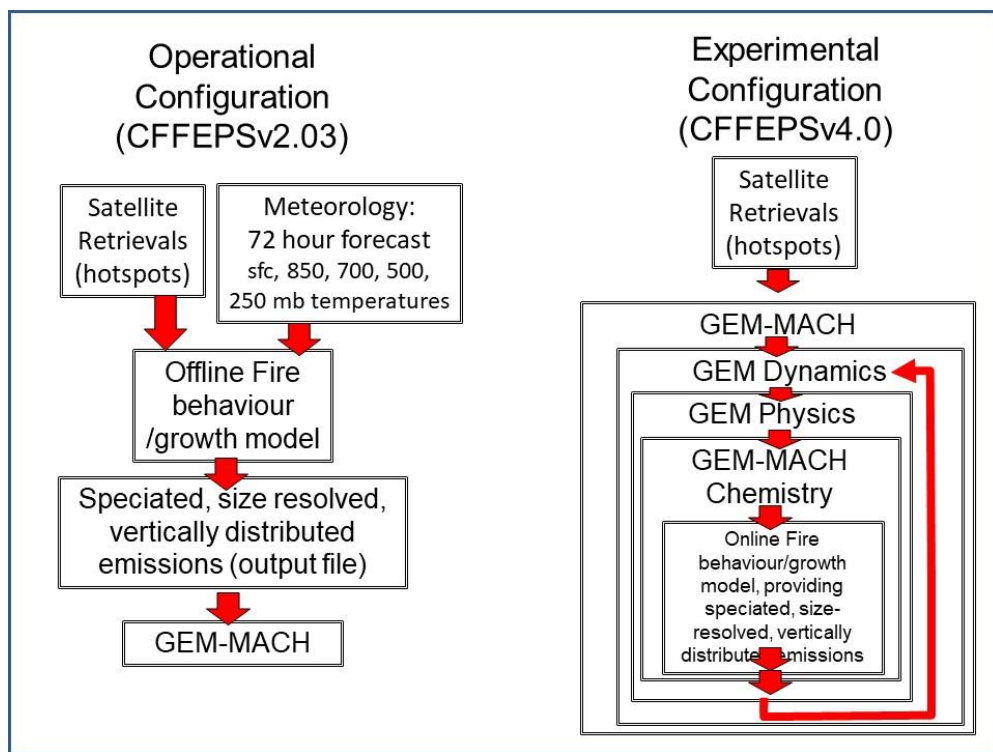
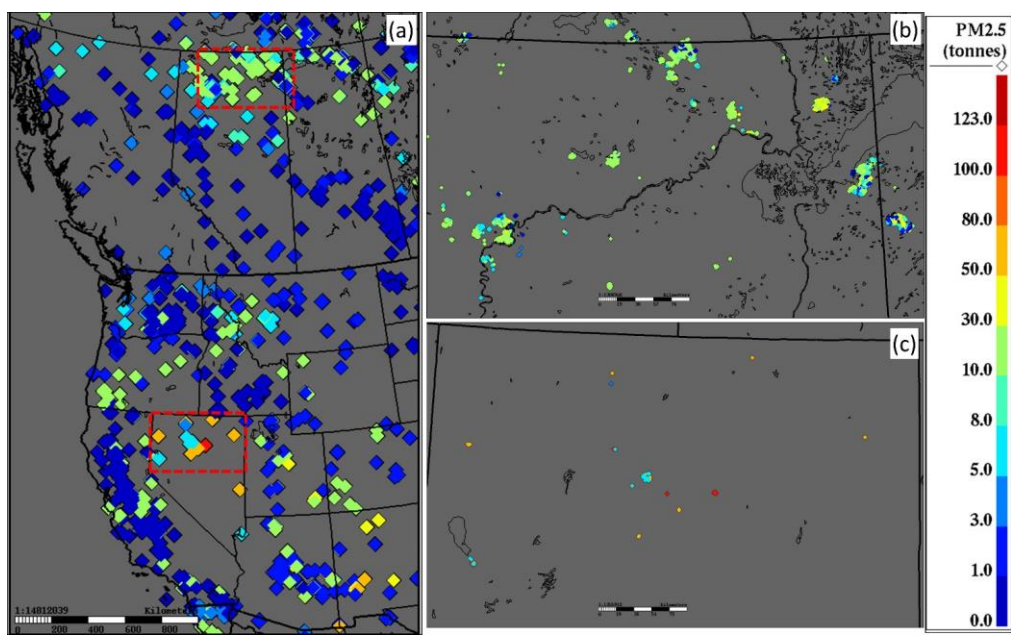


Figure 3: Process comparison between original (CFFEPSv2.03, left) and on-line (CFFEPSv4.0, right) forest fire emissions and vertical plume distribution algorithms.



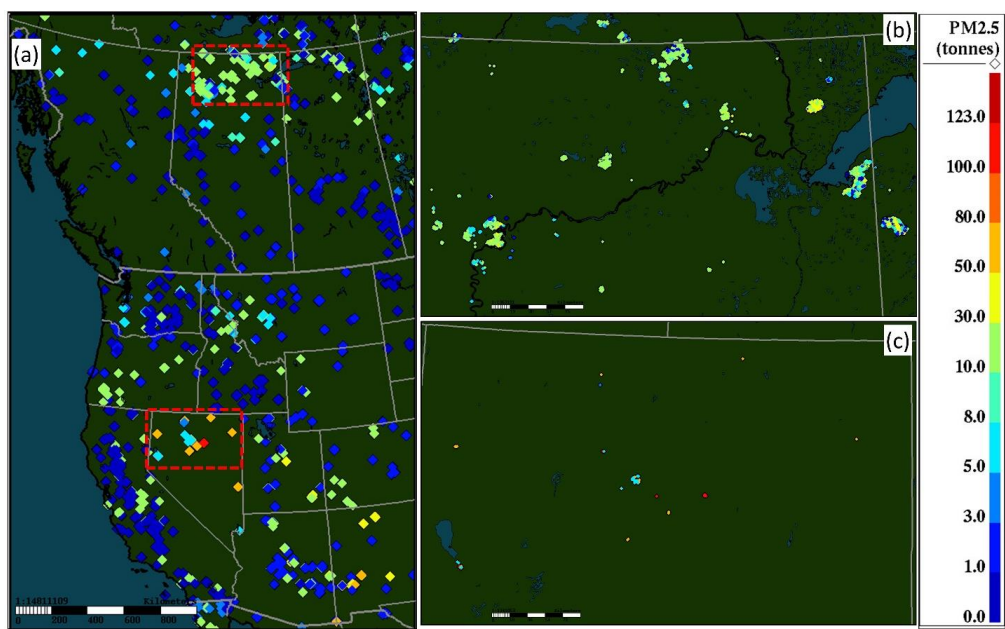
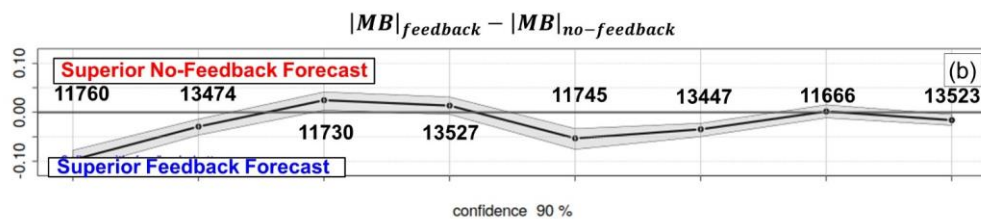
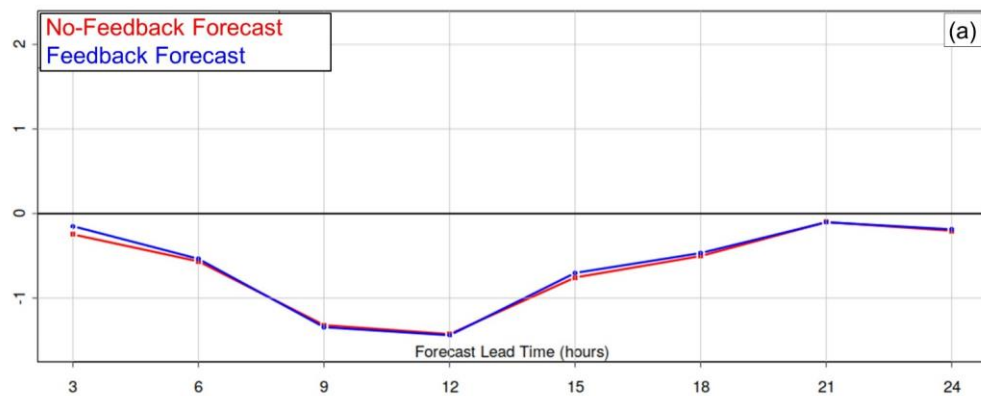


Figure 4: Hotspot locations during the study period, colour-coded by daily total tonnes PM_{2.5} emitted. (a) Entire model 2.5-km domain, with northern Alberta and northern Nevada sub-regions as red dashed boxes; (b) northern Alberta zoom, with smaller symbols for individual hotspots showing the large fire regions; (c) northern Nevada zoom, to the same scale as (b), showing isolated hotspots with high emissions.



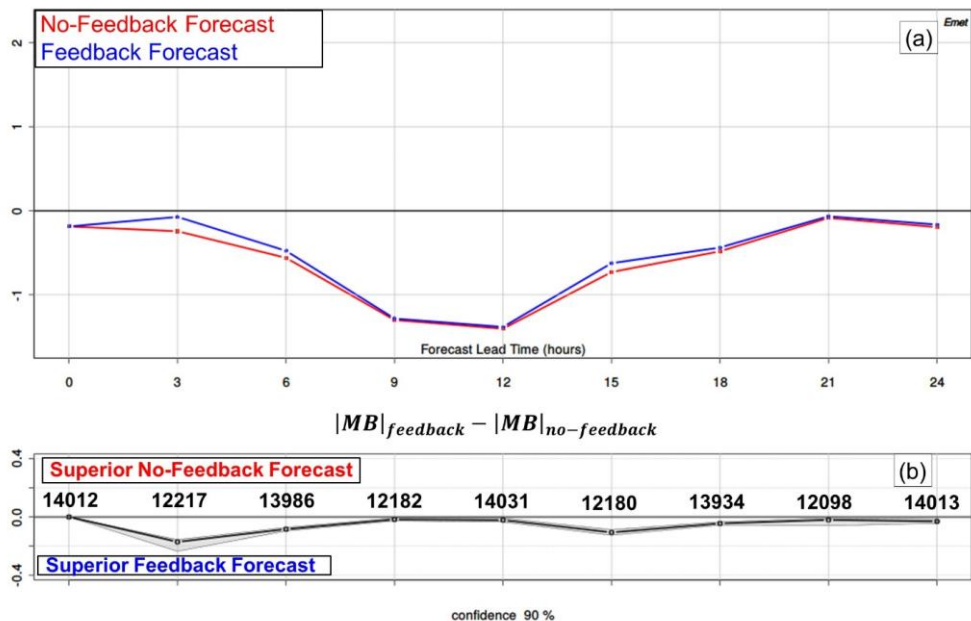
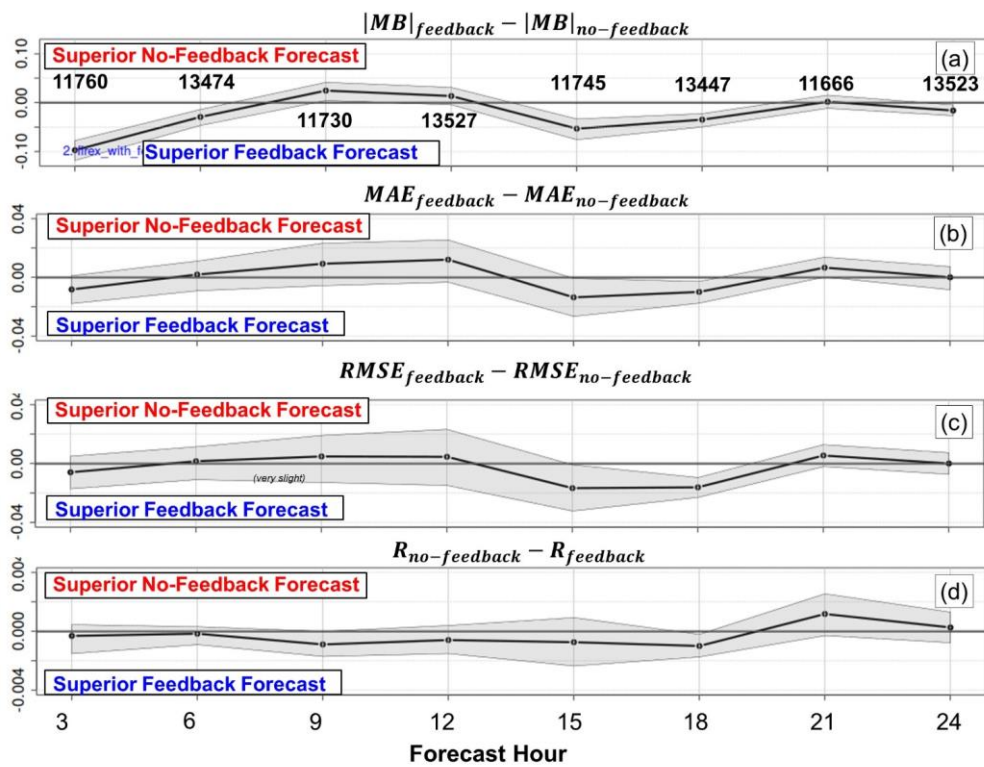


Figure 5: Mean bias in surface temperature (°C) at forecast hours starting at 0 UT. (a) Red line: no-feedback forecast values; blue line: feedback forecast values. (b) Difference in absolute value of mean bias between the two forecasts ($|MB|_{feedback} - |MB|_{no-feedback}$), with the region below 90% confidence level shown shaded grey. Mean values above/below the '0' line, and outside of the shaded region thus indicate differences in the mean between the two forecasts which differ at or above the 90% confidence level. Values of the difference which appear below/above the zero line and outside of the grey area thus indicate superior domain average performance for the feedback/no-feedback forecasts at each of the 3-hourly intervals, respectively. Numbers appearing above the metric differences are the number of observations contributing to the calculated metrics.



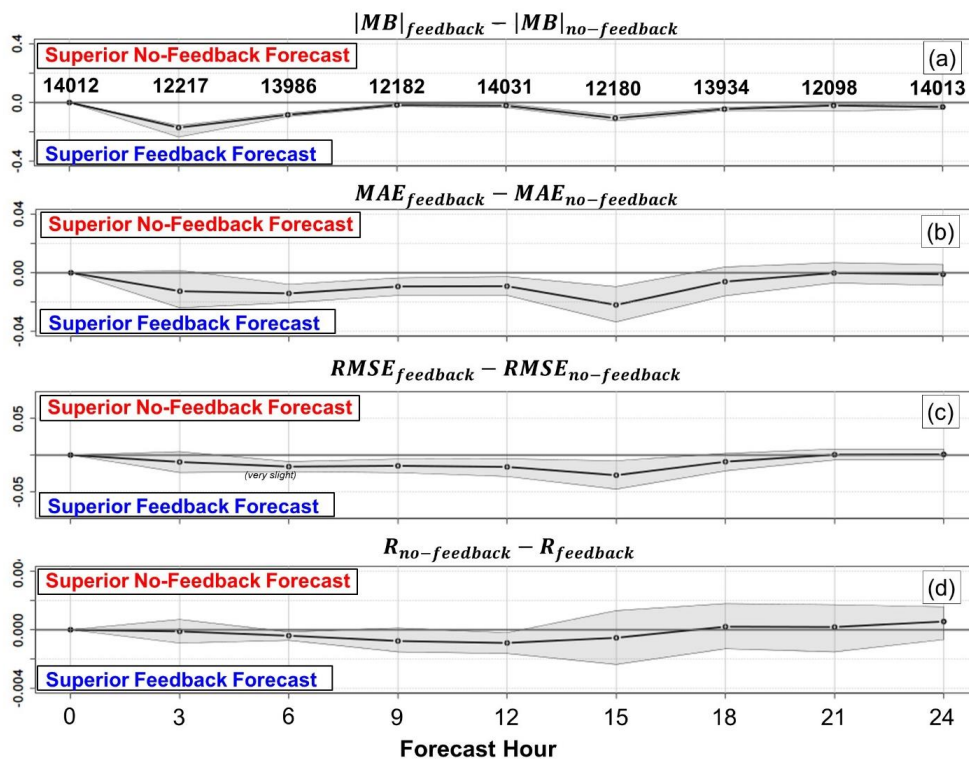
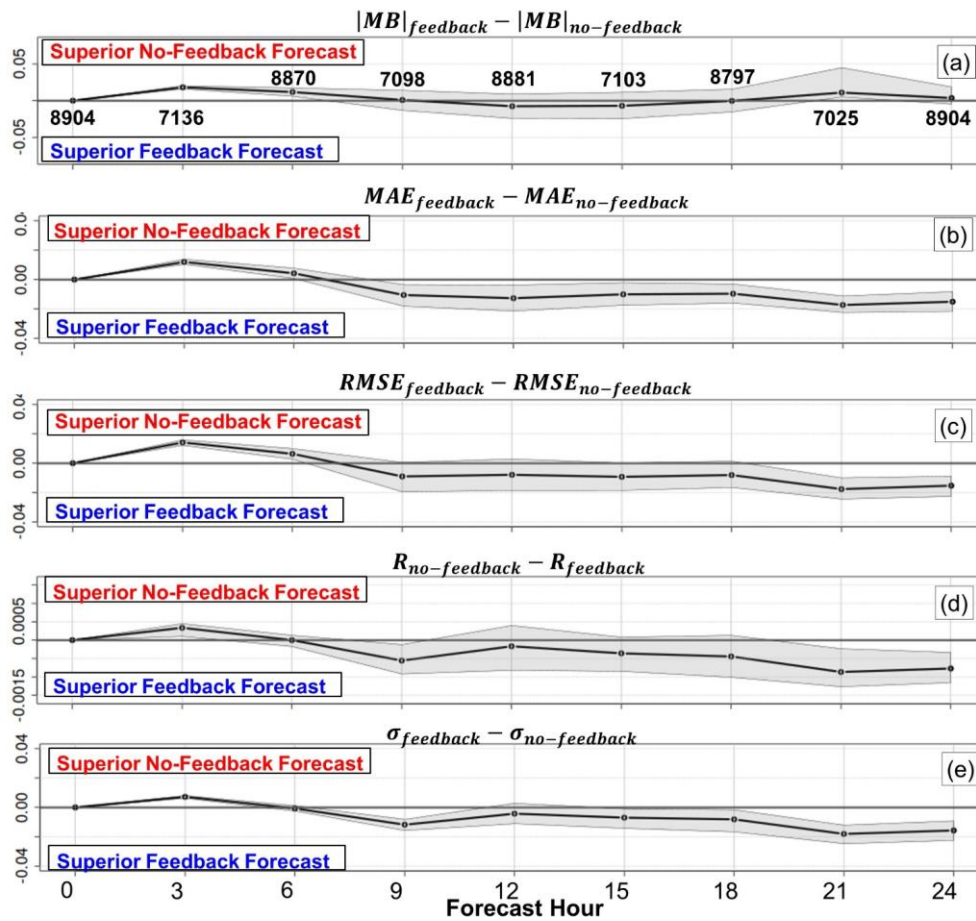


Figure 6: Summary meteorological performance comparison for surface temperature (C). (a) mean bias, (b) mean absolute error, (c) root mean square error and (d) Pearson correlation coefficient. 90% confidence level shown in grey. Numbers appearing above the absolute mean bias differences are the number of stations contributing to the calculated metrics.



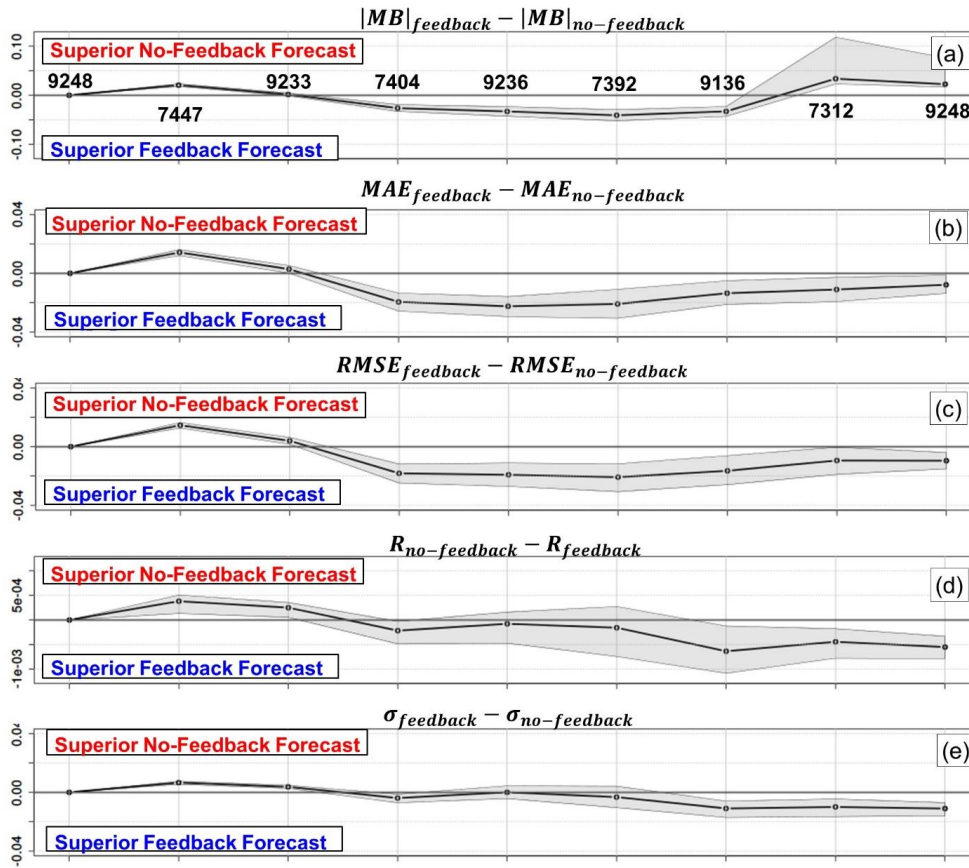
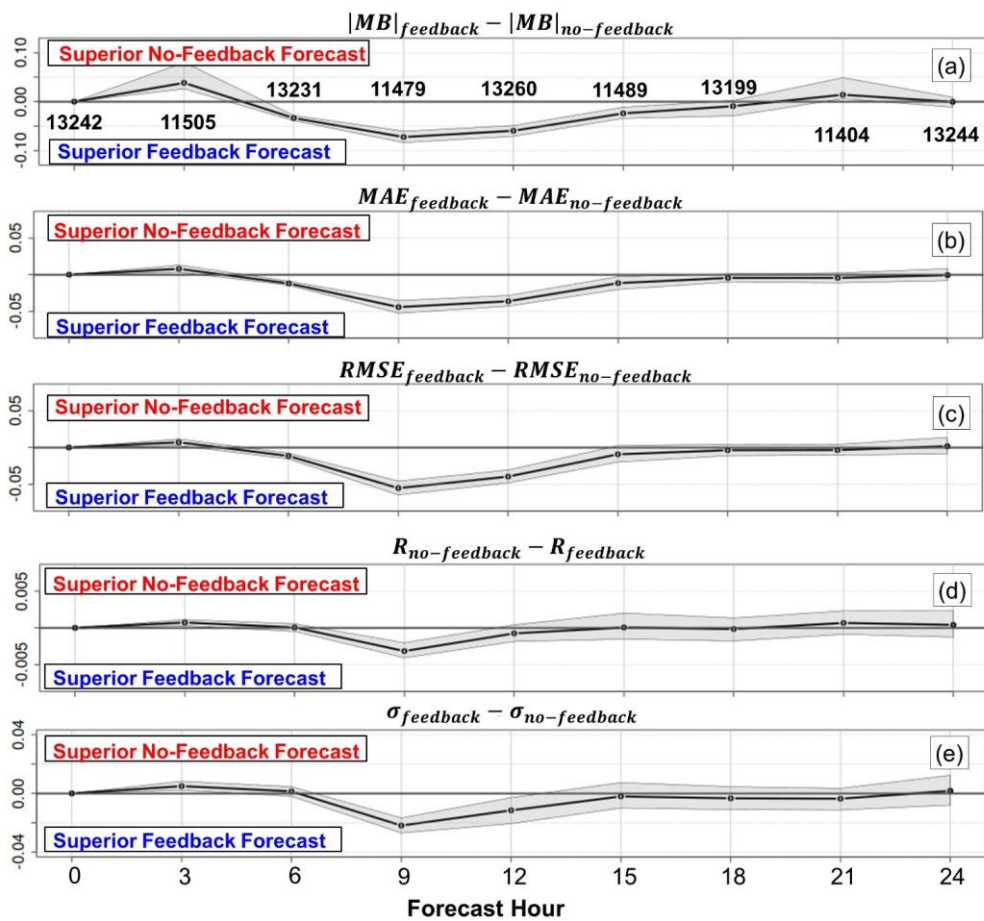


Figure 7: Summary meteorological performance comparison for surface pressure (hPa). (a) mean bias, (b) mean absolute error, (c) root mean square error, (d) Pearson correlation coefficient, and (e) standard deviation. 90% confidence level shown in grey. Numbers appearing above the absolute mean bias differences are the number of stations contributing to the calculated metrics.



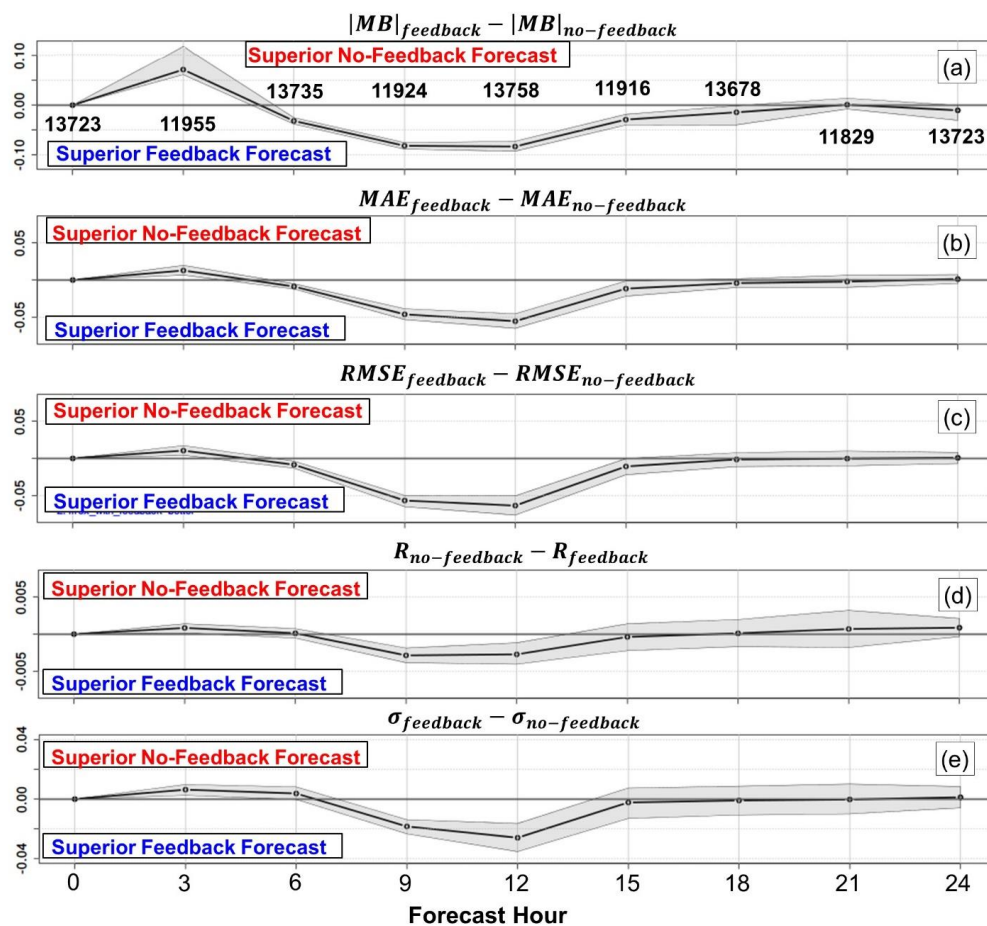
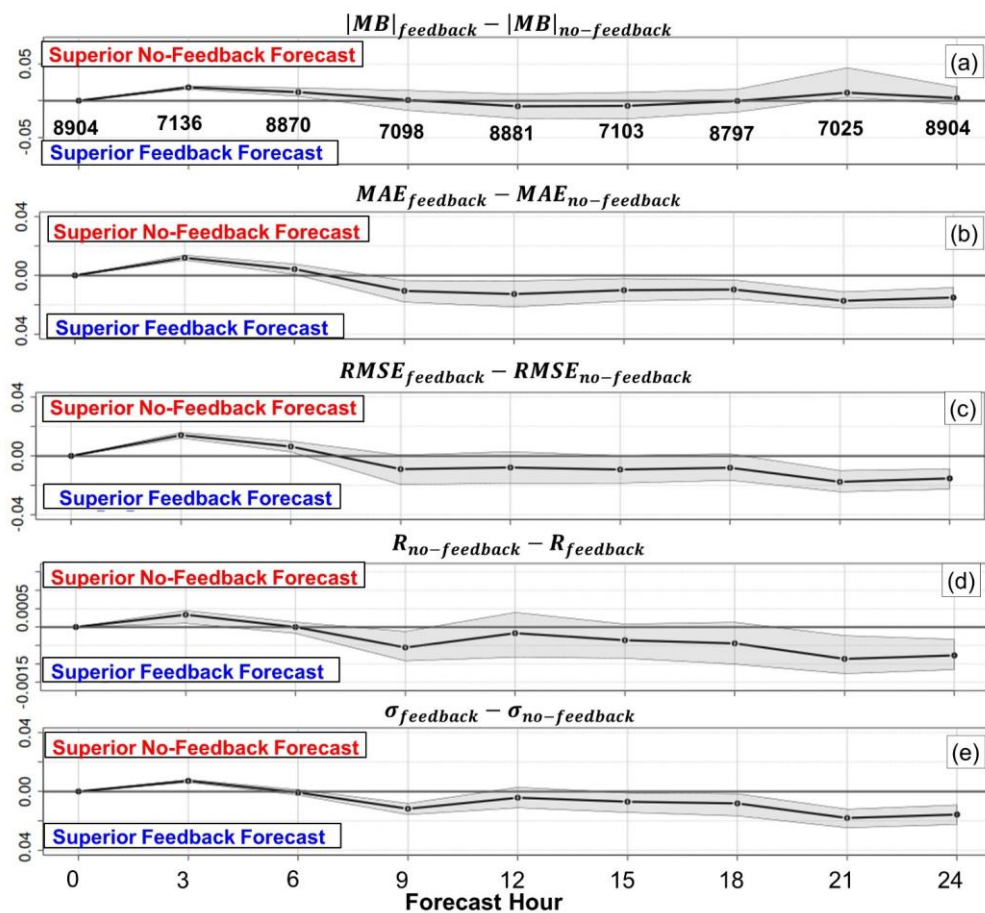
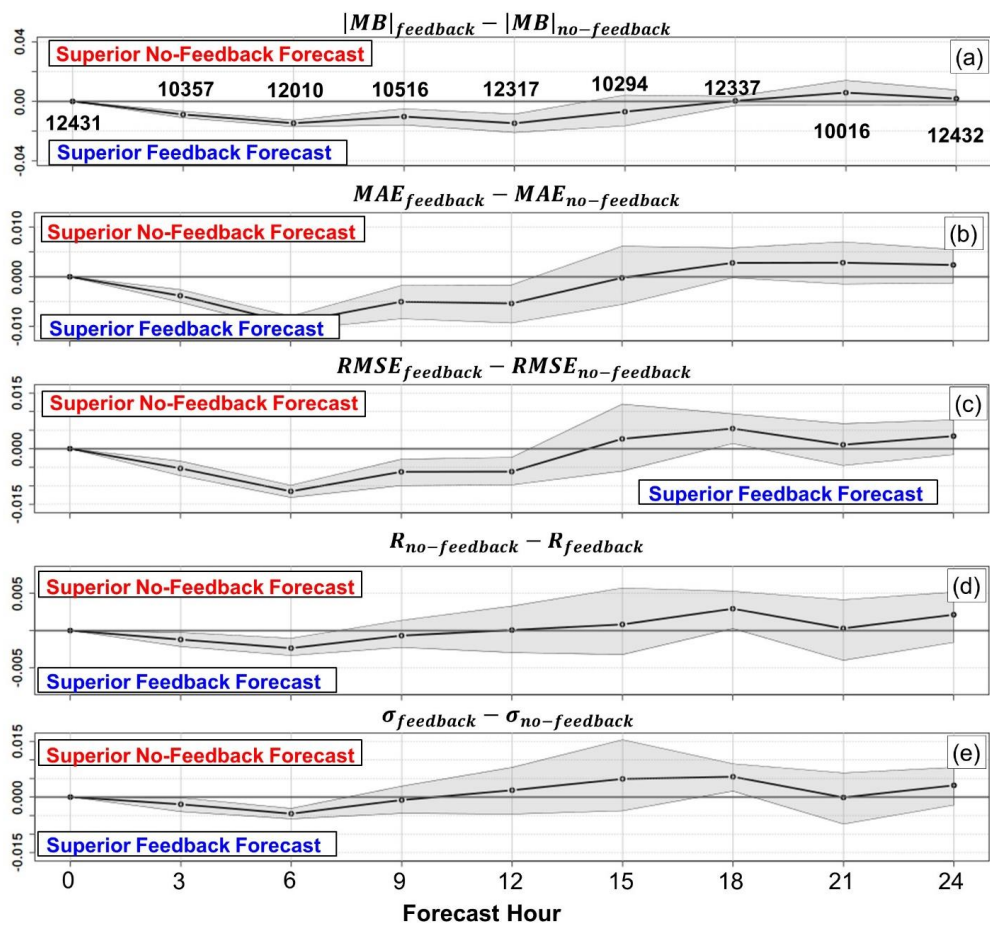


Figure 8: Summary meteorological performance comparison for dewpoint temperature (C). (a) mean bias, (b) mean absolute error, (c) root mean square error, (d) Pearson correlation coefficient, and (e) standard deviation. 90% confidence level shown in grey. Numbers appearing above the absolute mean bias differences are the number of stations contributing to the calculated metrics.



Figure



: Summary meteorological performance comparison for sea-level pressure (hPa). (a) mean bias, (b) mean absolute error, (c) root mean square error, (d) Pearson correlation coefficient, and (e) standard deviation. 90% confidence level shown in grey. Numbers appearing above the absolute mean bias differences are the number of stations contributing to the calculated metrics.

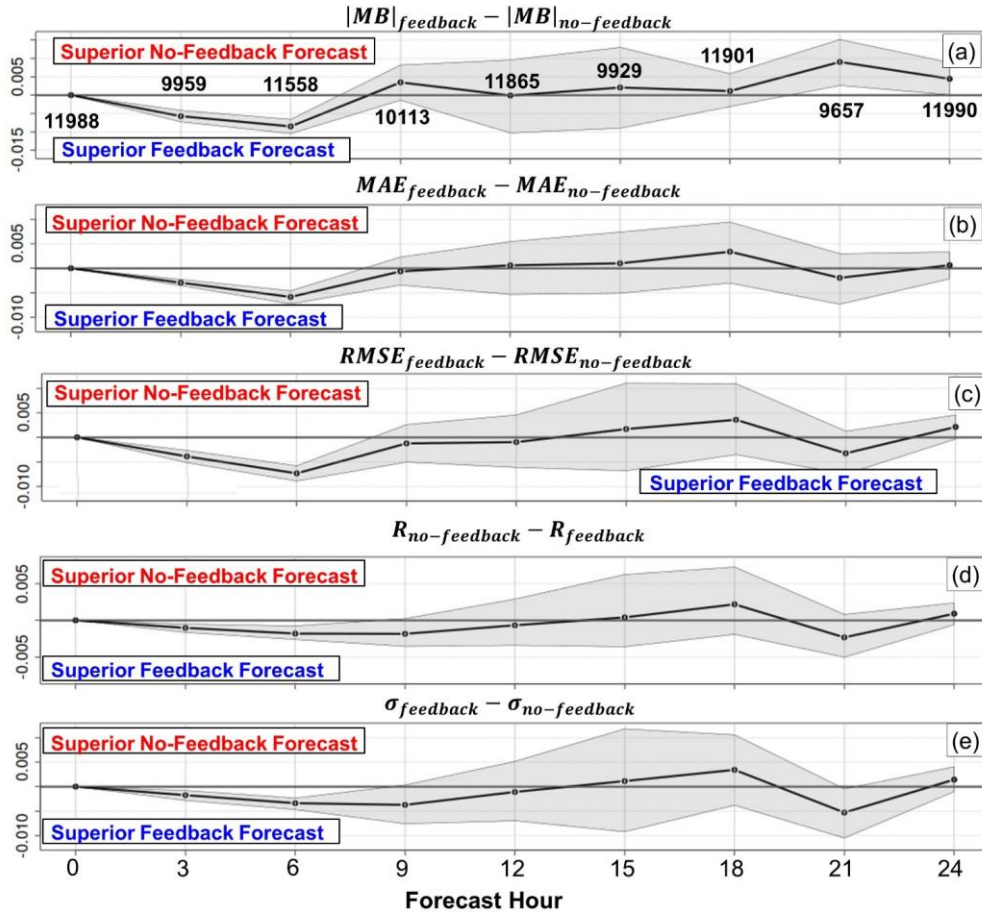


Figure 109: Summary meteorological performance comparison for 10m windspeed (m s^{-1}). (a) mean bias, (b) mean absolute error, (c) root mean square error, (d) Pearson correlation coefficient, and (e) standard deviation. 90% confidence level shown in grey. Numbers appearing above the absolute mean bias differences are the number of stations contributing to the calculated metrics.

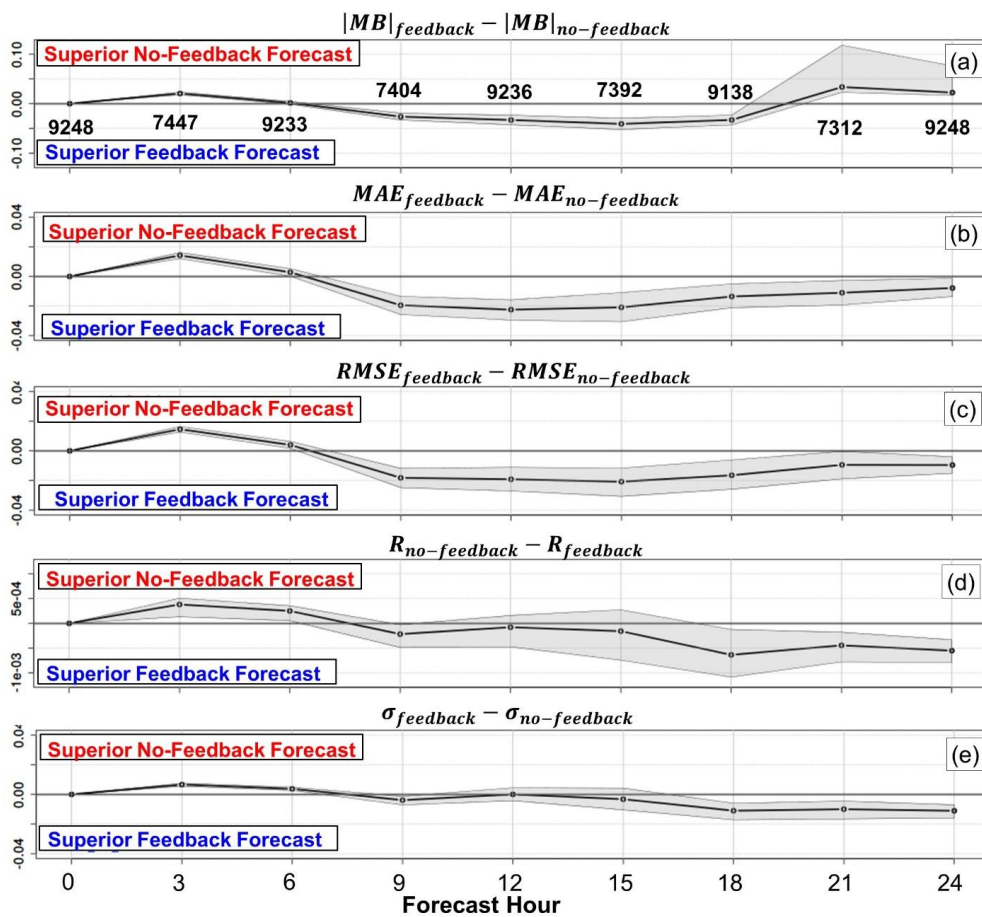
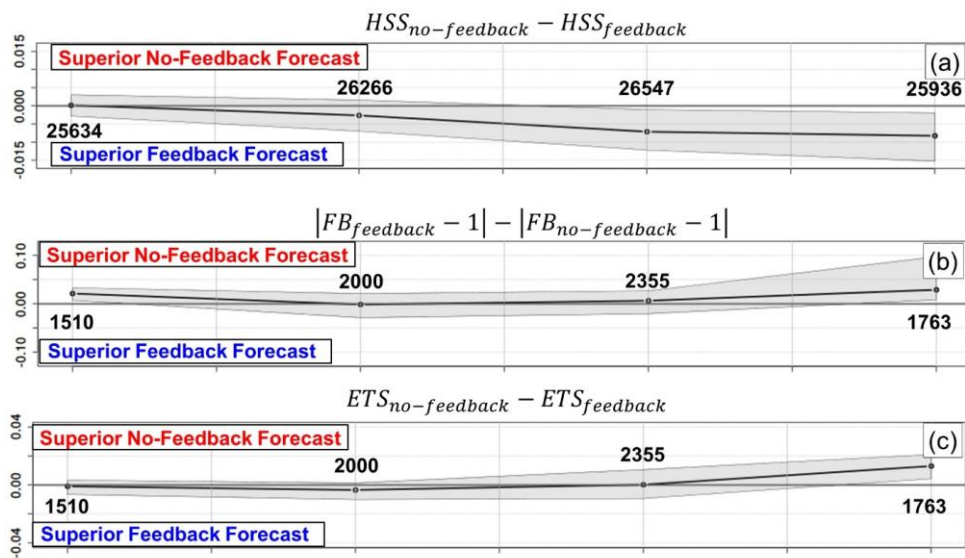


Figure 10: Summary meteorological performance comparison for sea-level pressure (hPa). (a) mean bias, (b) mean absolute error, (c) root mean square error, (d) Pearson correlation coefficient, and (e) standard deviation. 90% confidence level shown in grey. Numbers appearing above the absolute mean bias differences are the number of stations contributing to the calculated metrics.



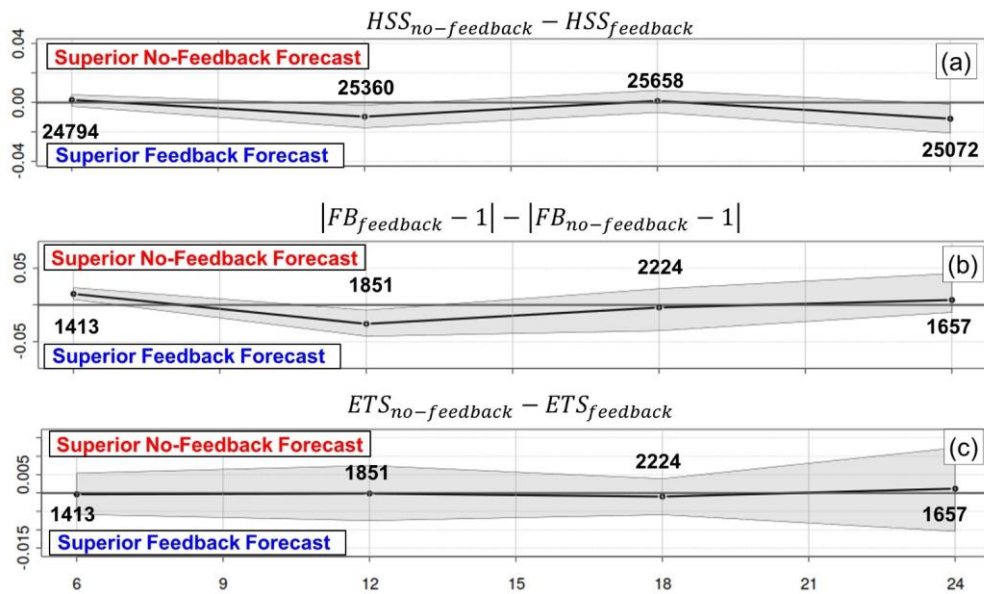
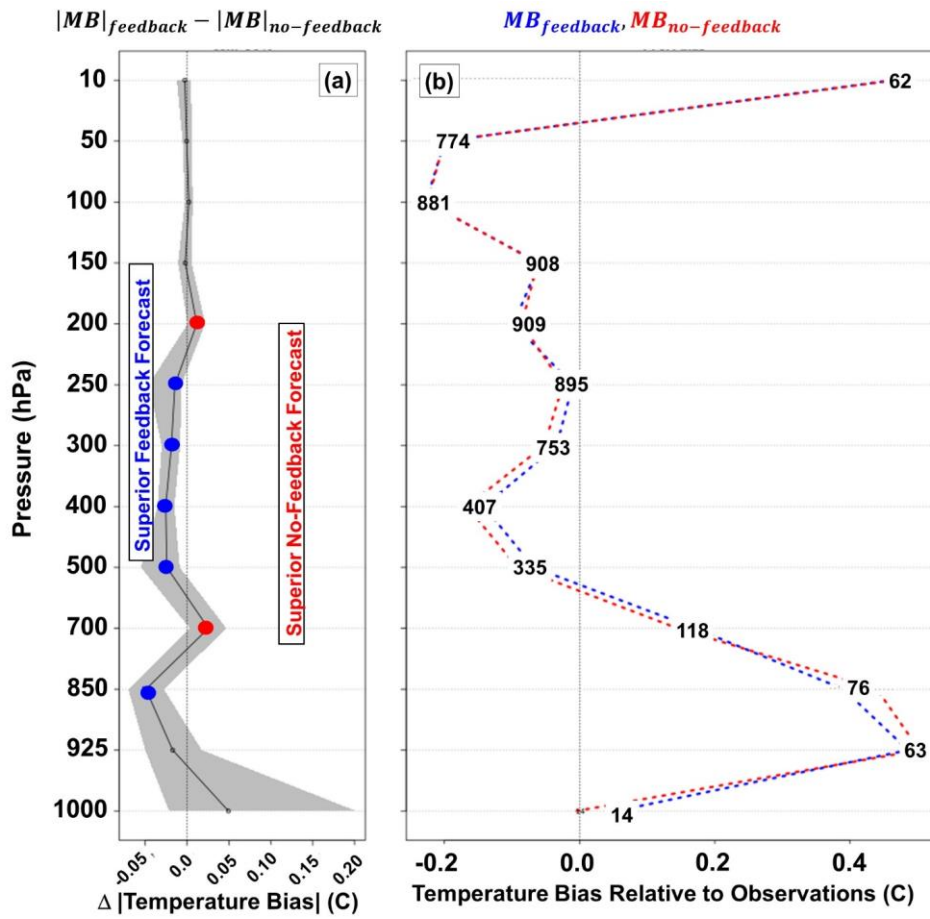


Figure 11: Precipitation performance evaluation (mm precipitation). (a) Heike skill score of 6-hour accumulated precipitation (No-Feedback – Feedback). (b) Frequency bias index of 6-hour accumulated precipitation (threshold of 2 mm, No-Feedback – Feedback). (c) Equitable Threat Score of 6-hour accumulated precipitation (threshold of 2 mm, No-Feedback – Feedback).



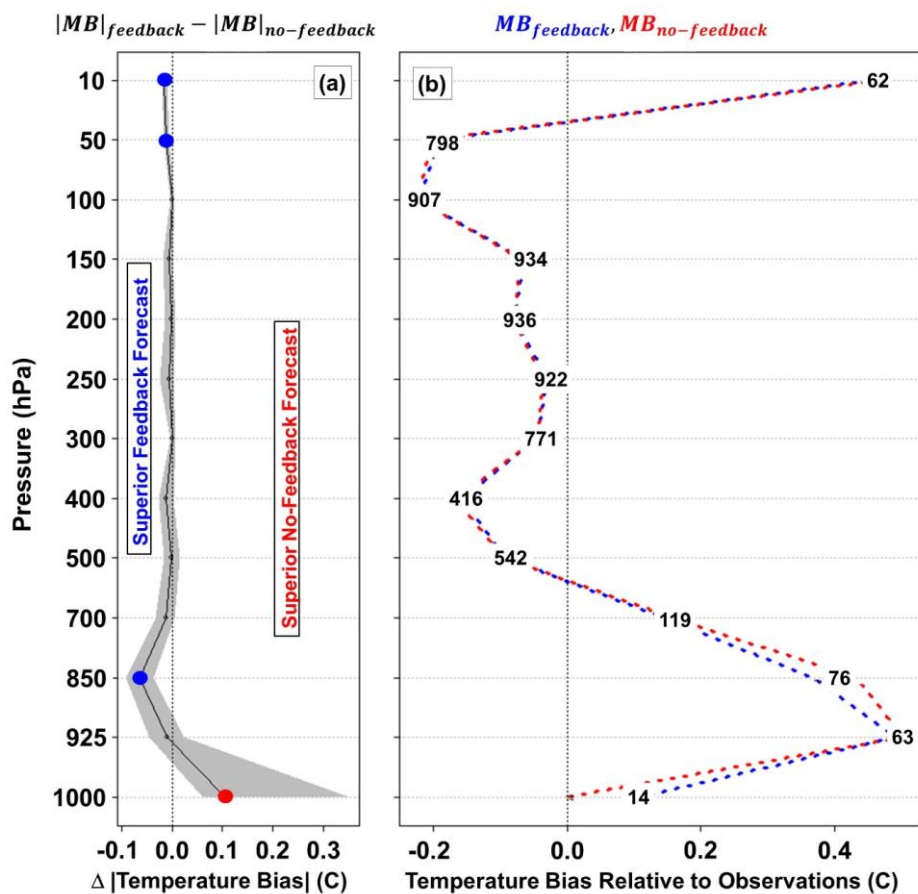
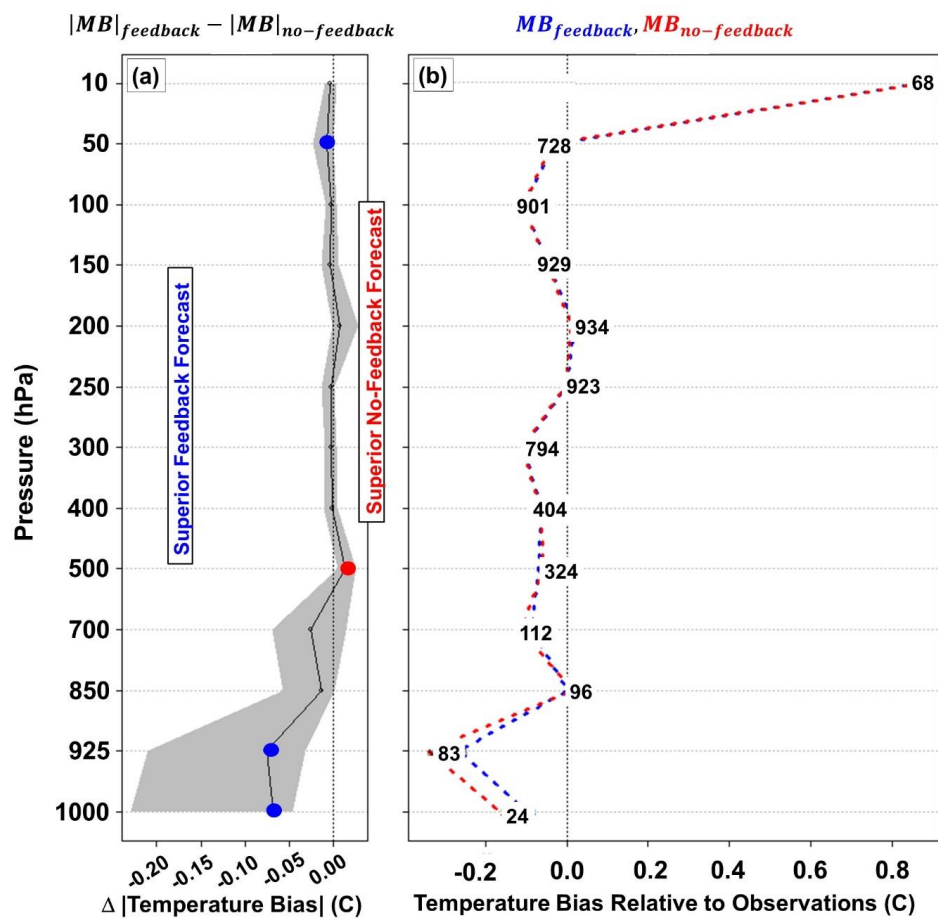


Figure 12: Forecast hour 12 (0 UT) summary upper air temperature performance comparison for air temperature (mean bias, C). (a) Difference in absolute value of mean bias in temperature, (feedback forecast - no-feedback forecast). Grey regions represent 90% confidence levels, blue symbols: pressure levels at which the feedback mean bias outperforms the no-feedback mean-bias at > 90% confidence. Red symbols: pressure levels at which the no-feedback mean bias outperforms the feedback mean bias at > 90% confidence. 90% confidence level shown in grey. (b) Mean bias in upper air temperature for feedback (blue) and no-feedback (red) (C). Numbered values on the profiles indicate the number of observed data-model pairs at each pressure level.



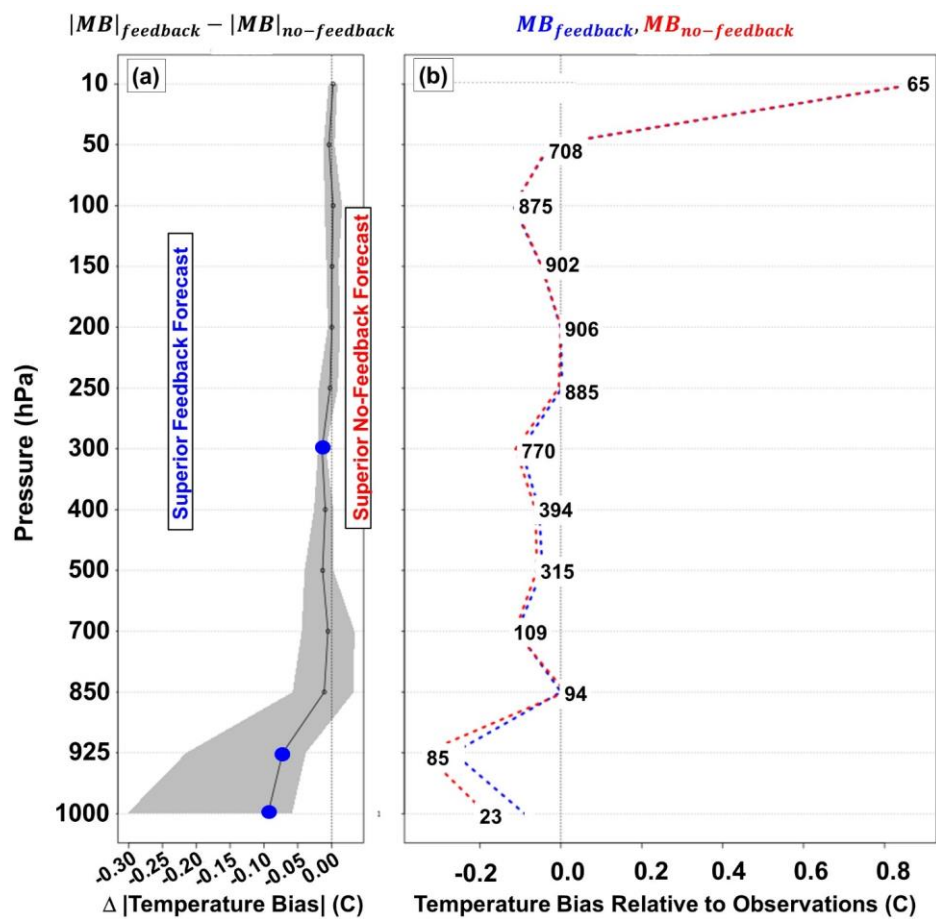
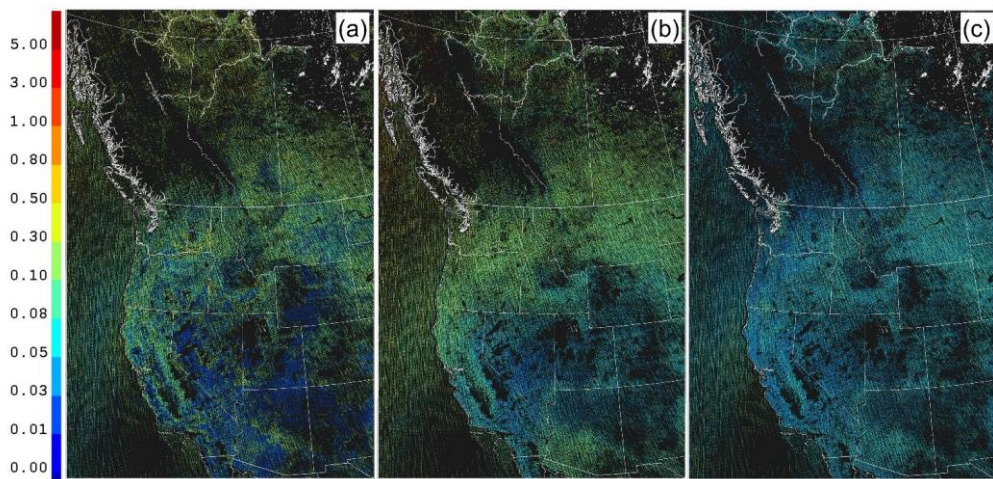


Figure 13: Forecast hour 24 (12 UT) summary upper air temperature performance comparison for air temperature (mean bias, C). (a,b) as in Figure 12.



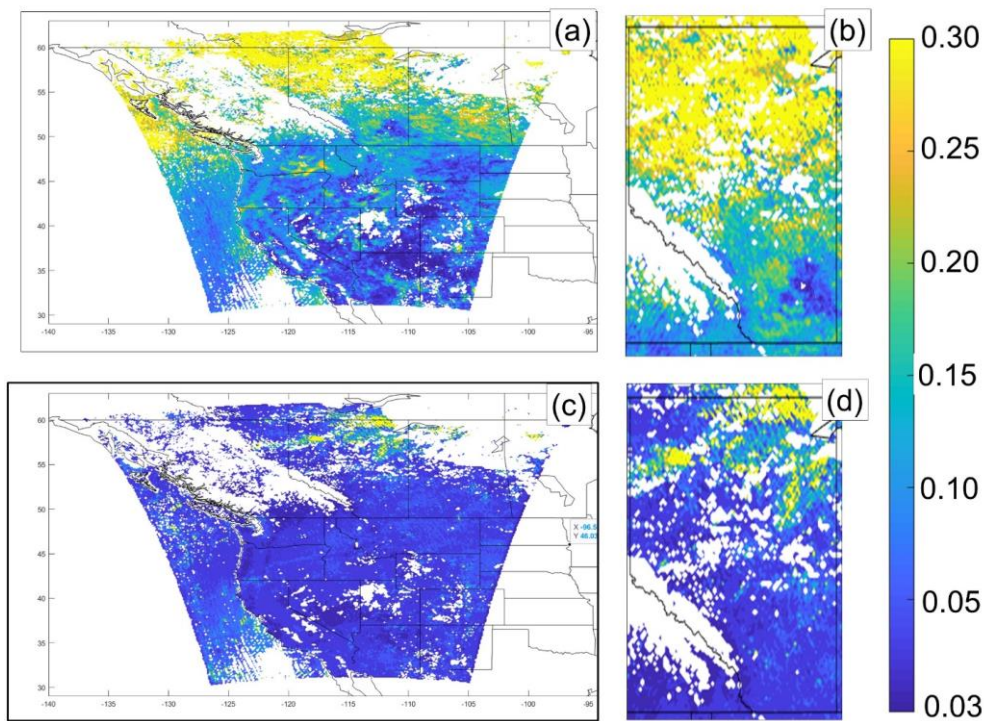


Figure 14: 550nm AOD comparison. (a) All MODIS observations spatiotemporally averaged and sampled over the model domain and forecast duration and (b) zoom-in on the province of Alberta. (c,d) GEM-MACH 2.5km simulation, driven by 10km GEM-MACH simulations, in turn driven by ECMWF Reanalysis nearest output hour AOD values corresponding to satellite sensor data availability, for 2.5km domain boundary conditions. (c) GEM-MACH 2.5km simulation, driven by MOZART climatological boundary conditions, the same regions.

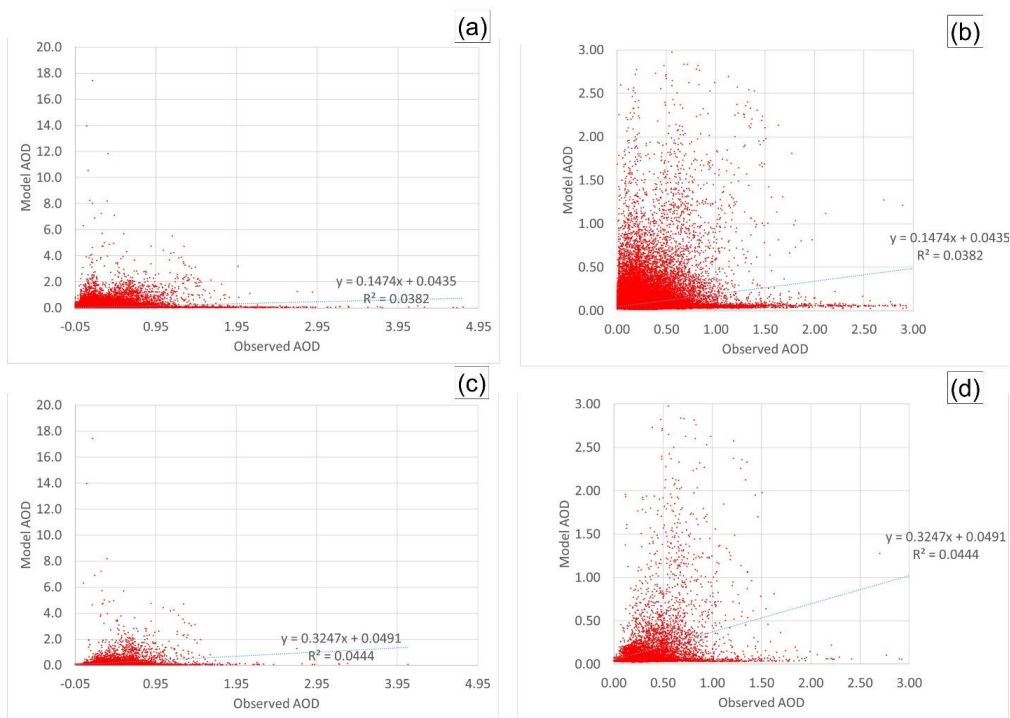
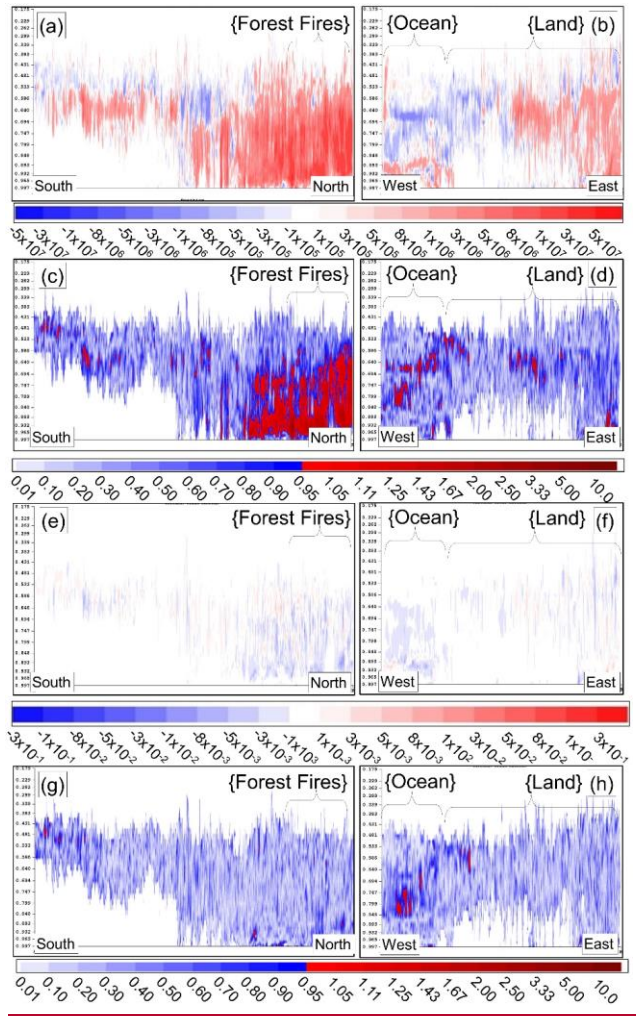


Figure 15: Scatterplots comparing model and observed AOD values. (a) All model observation pairs. (b) As in (a), rescaled to focus on AODs in the 0.3 range. (c) Model observation pairs in the region bounded by 56N, 60N, 110W and 120 W (northern Alberta). (d) As in (c), rescaled to focus on AODs in the 0.3 range.



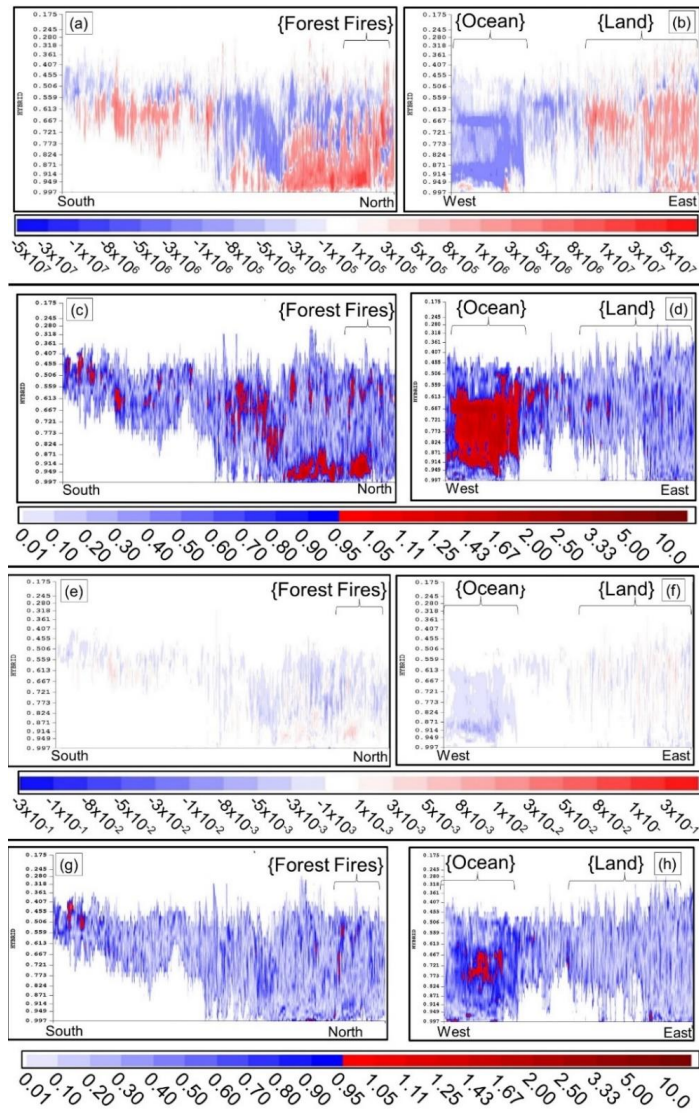
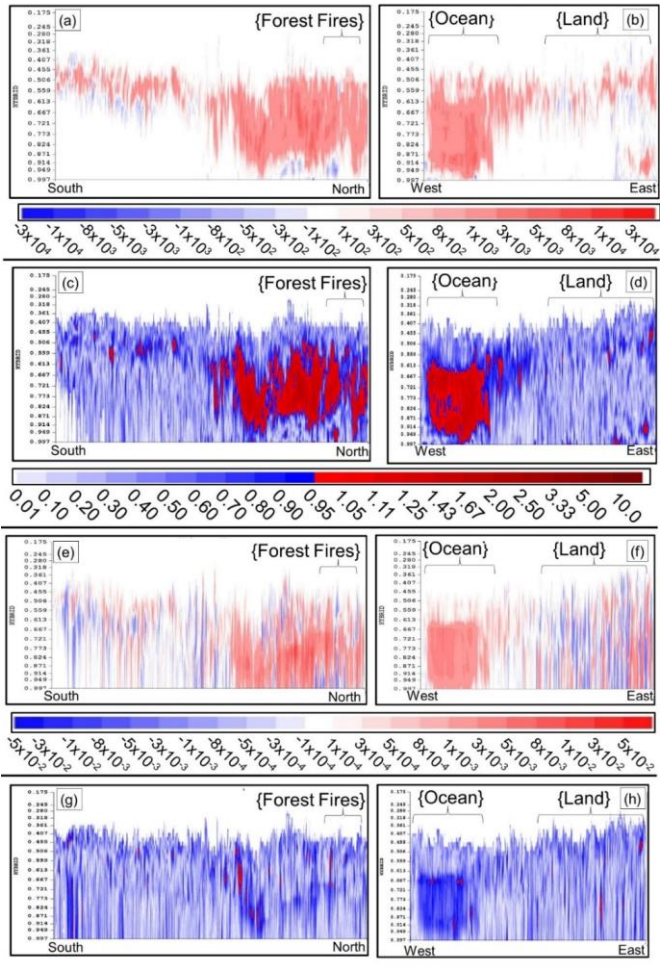


Figure 1546. (a,b) Difference in mean (Feedback – No-Feedback) cloud droplet number simulations along south to north and east to west cross-sections through the middle of the model domain. (c,d) Corresponding significance level of mean cloud droplet number

differences using the confidence ratio defined in equation (1) – red areas indicate ratio values greater than unity, i.e., significance at or above the 90% confidence level. (e,f) Difference in mean cloud droplet mass (g kg^{-1}) (g,h) Corresponding significance level of mean cloud droplet mass difference. *Note: the vertical axis in hybrid coordinates does not show all model levels for clarity; the model has much finer resolution in the lower part of the atmosphere than shown, and the portion of the vertical domain shown encompasses only the lower half of the levels in the model.*



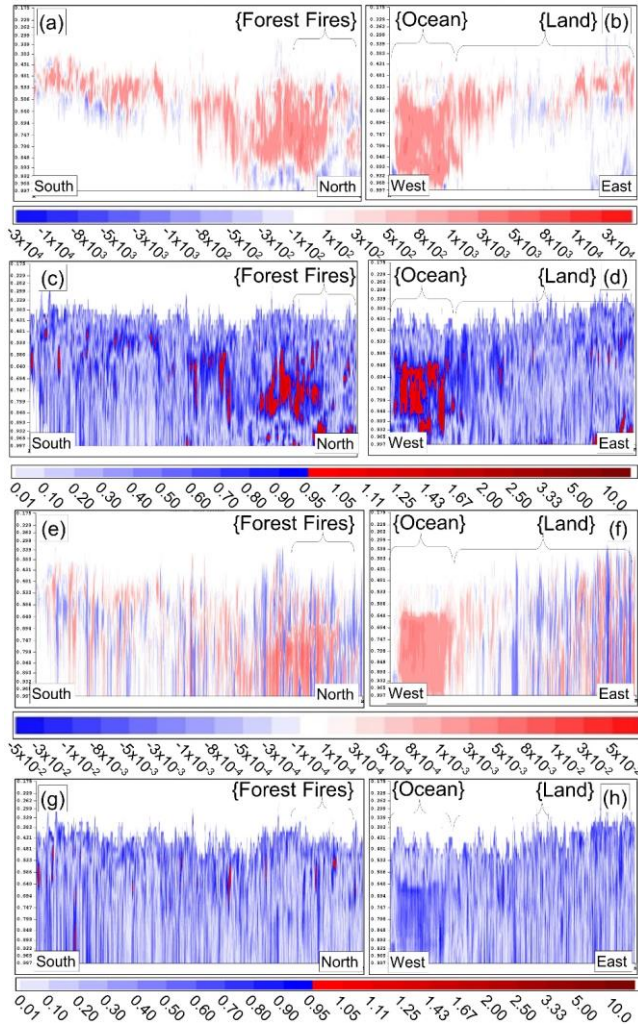
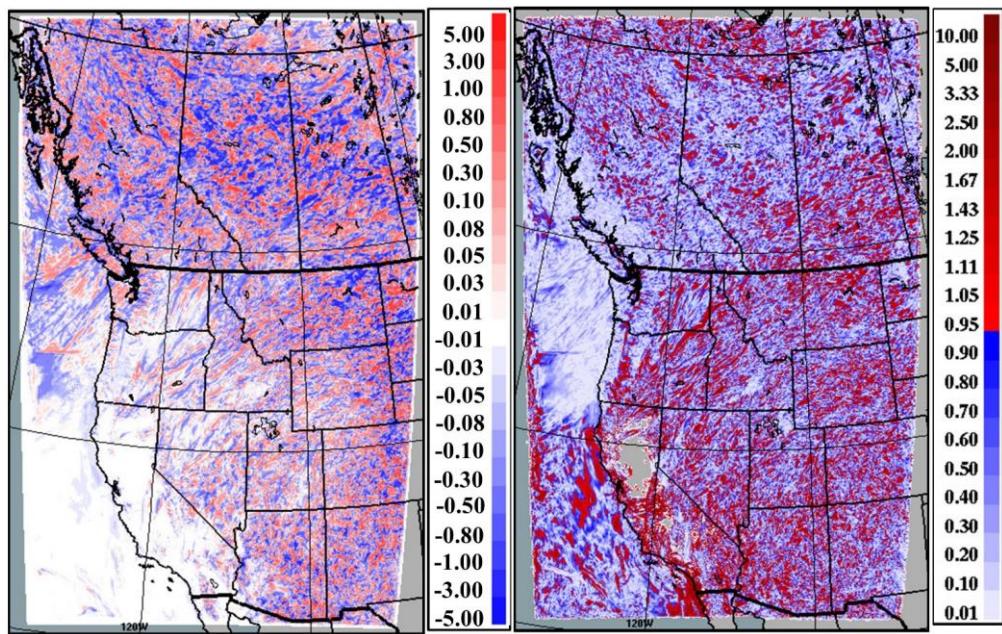


Figure 1647. (a,b) Difference in mean (Feedback – No-Feedback) rain drop number simulations along south-to-north and east-to-west cross-sections through the middle of the model domain. (c,d) Corresponding significance level of mean rain drop number differences using the confidence ratio defined in equation (1) – red areas indicate ratio values greater than unity, i.e., significance at or above the 90% confidence level. (e,f) Difference in rain cloud drop mass (g kg^{-1}) (g,h) Corresponding significance level of mean rain drop mass difference.



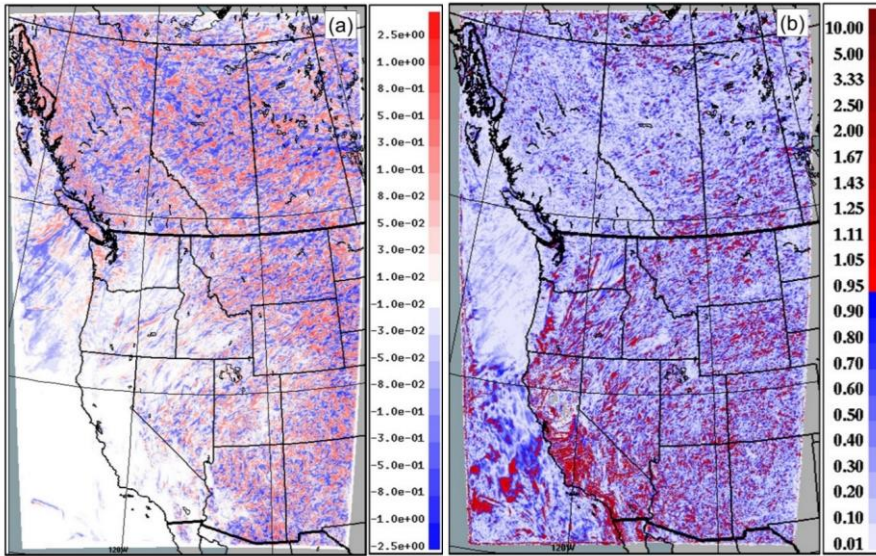
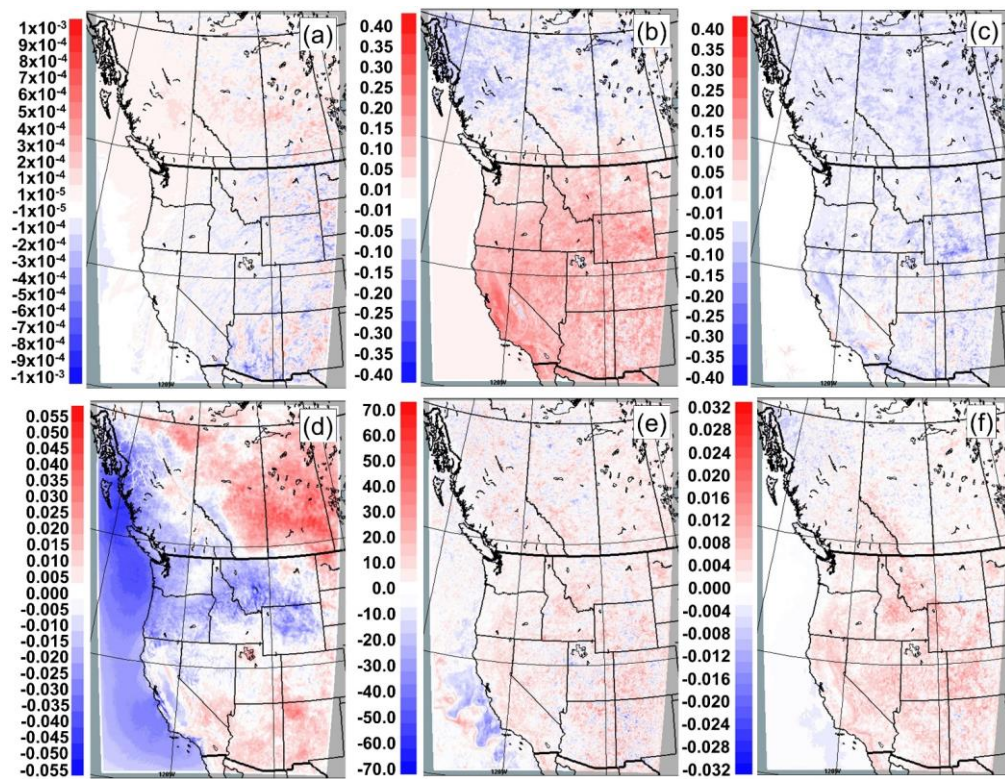


Figure 1748: (a) Average (Feedback - No Feedback) total surface precipitation during the simulation period. (b) 90% confidence ratio - values greater than 1 indicate significantly different results at the 90% confidence level.



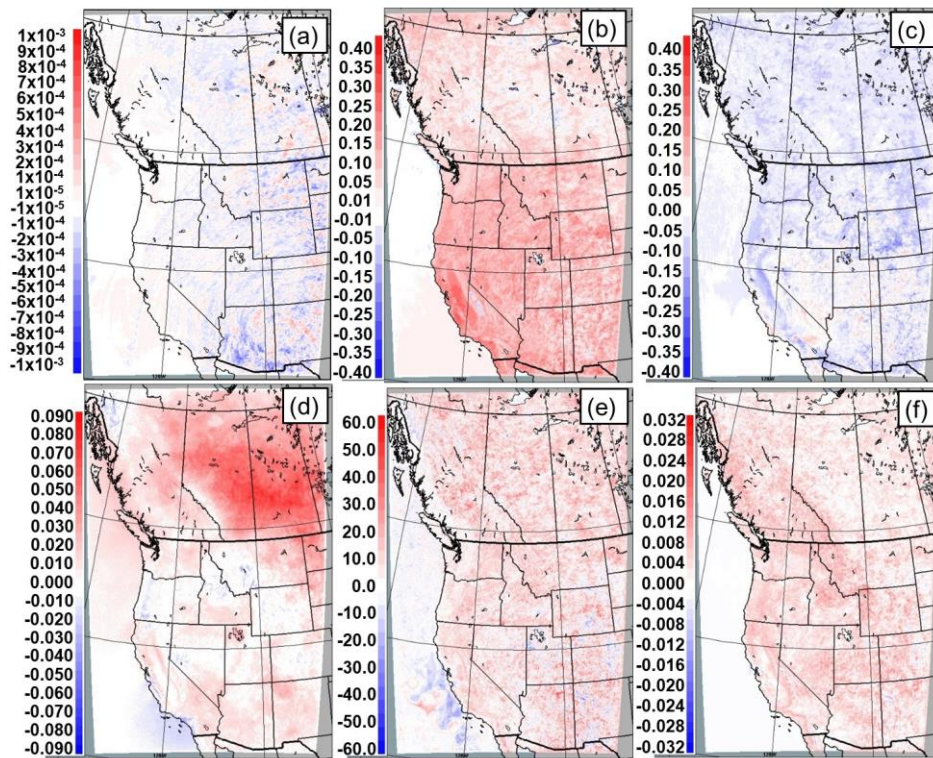
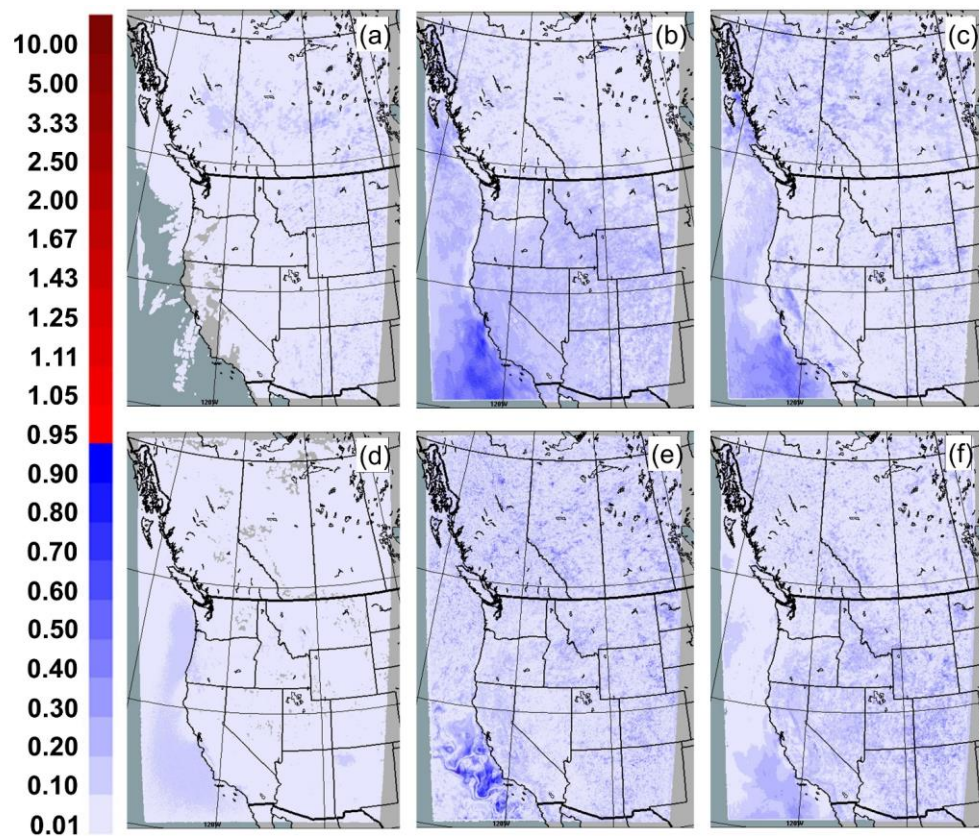


Figure 1849: Differences in average meteorological fields (feedback – no-feedback; red values indicate more positive values in the feedback simulation than in the no-feedback simulation). Panels show average difference in: (a) specific humidity (g kg^{-1}); (b) air temperature ($^{\circ}\text{C}$), (c) dewpoint temperature ($^{\circ}\text{C}$), (d) surface pressure (mb), (e) planetary boundary layer height (m), (f) friction velocity (m s^{-1}).



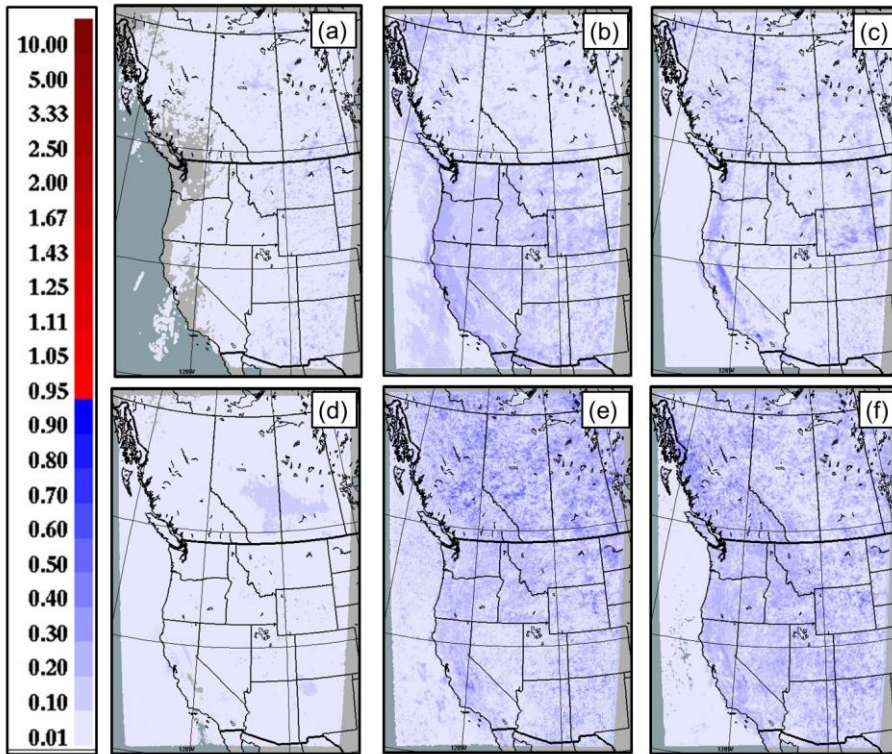
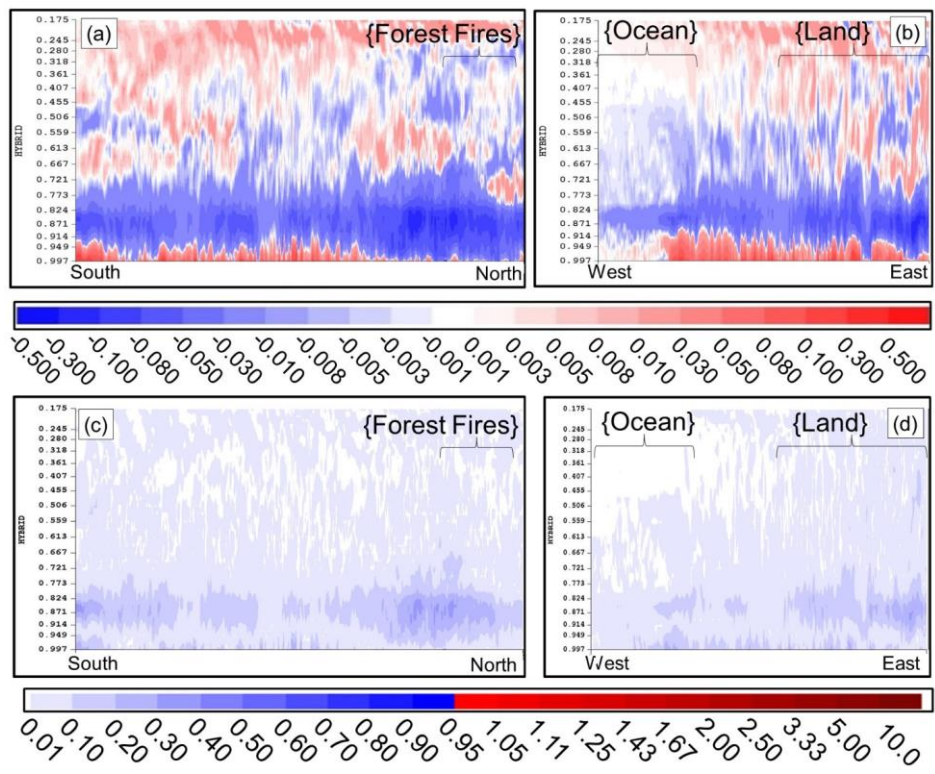


Figure 1920: 90% confidence ratios, same fields as Figure 19. Values greater than 1 indicate significantly different results at or greater than the 90% confidence level.



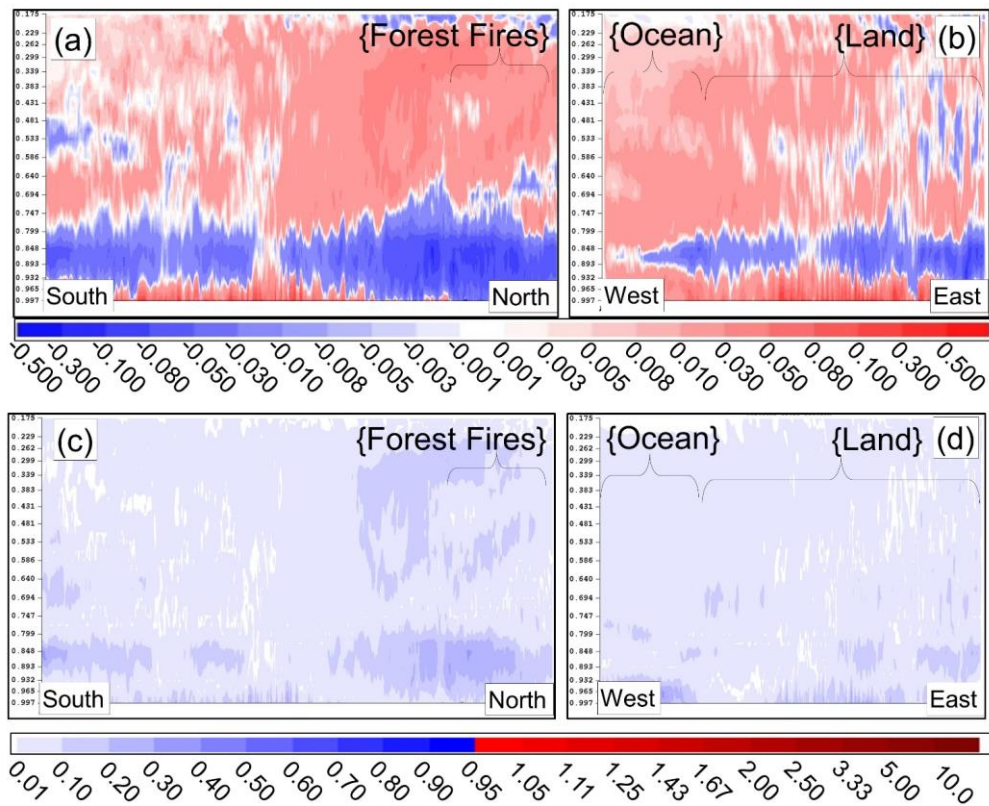
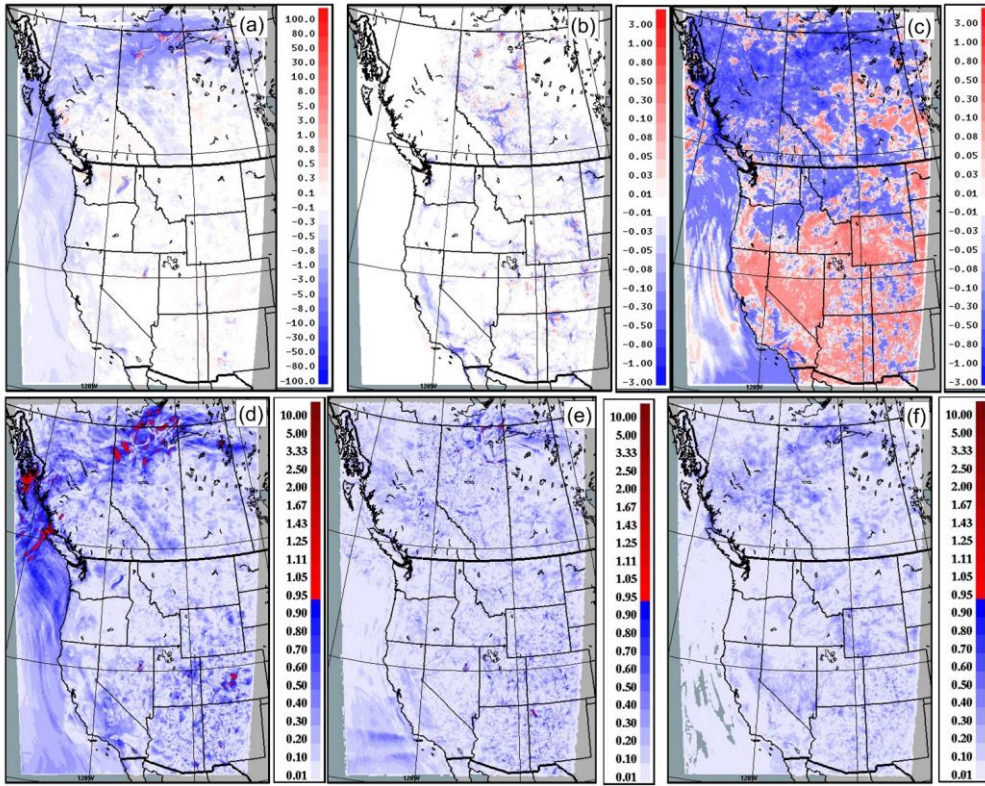


Figure 2024: (a,b) Difference in mean (Feedback - No-Feedback) temperature simulations along south-to-north and east-to-west cross-sections through the middle of the model domain. (c,d) Corresponding confidence ratio of mean temperature differences— red areas indicate ratio values greater than unity, i.e., significance at or above the 90% confidence level. ~~Note the reduction in temperatures between hybrid levels 0.90 to 0.70, similar to the findings of Saponaro et al., (2017).~~



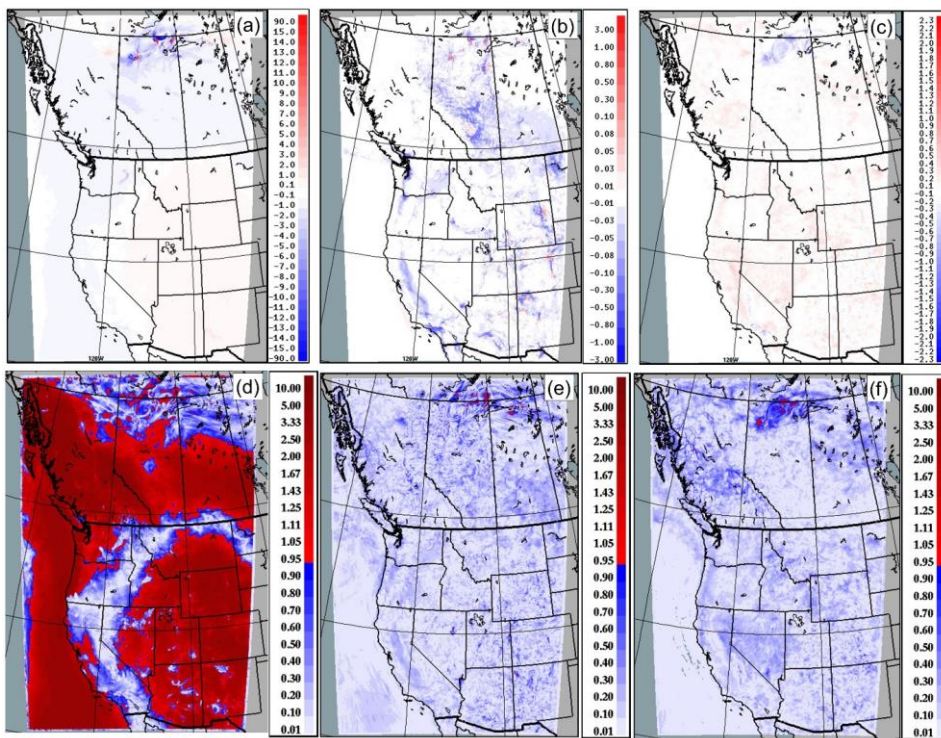


Figure 2122: (a,b,c) Difference (Feedback – No-Feedback) in surface mean PM_{2.5} (ug m⁻³), NO₂ (ppbv) and O₃ (ppbv), respectively. (d,e,f) Corresponding confidence ratio of mean differences – red areas indicate ratio values greater than unity, i.e., significance at or above the 90% confidence level.

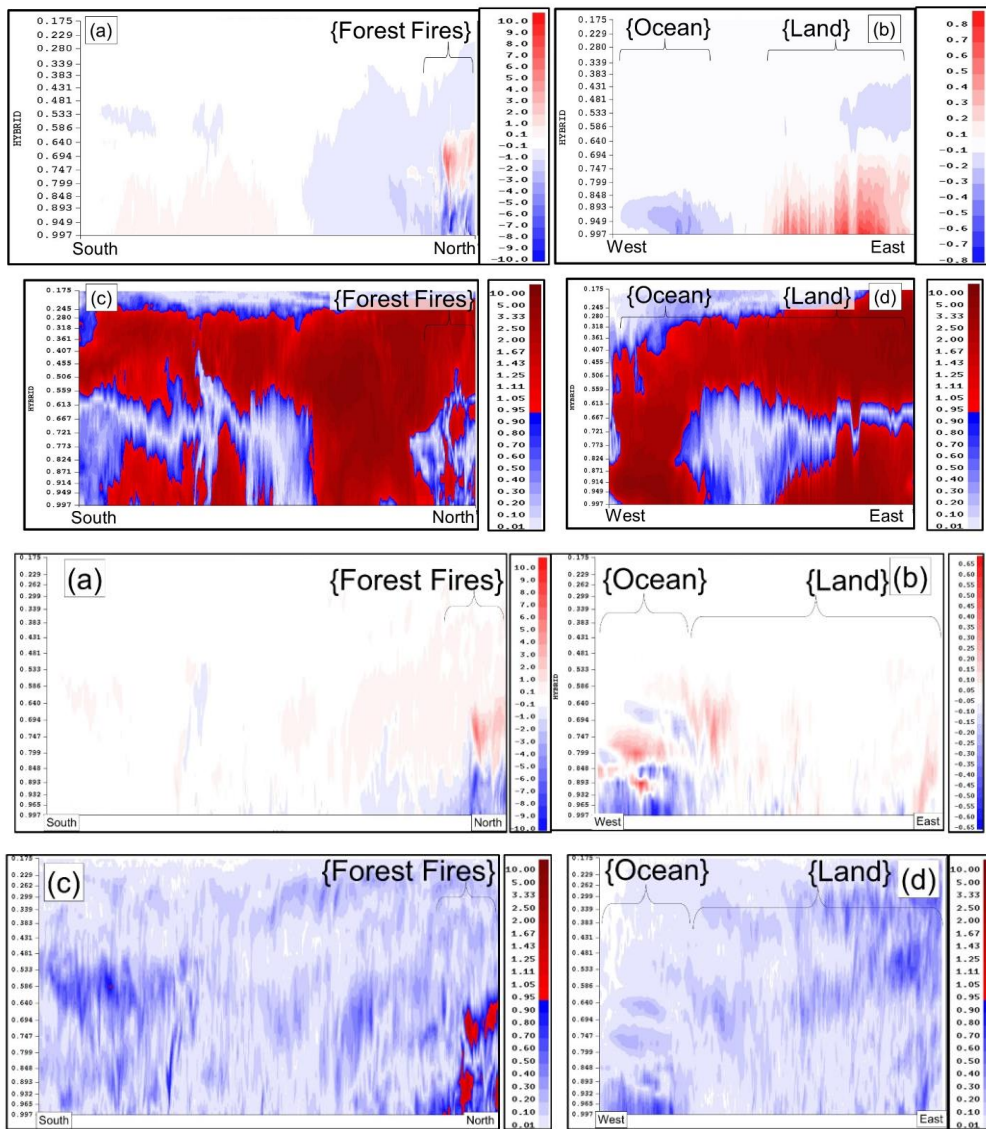
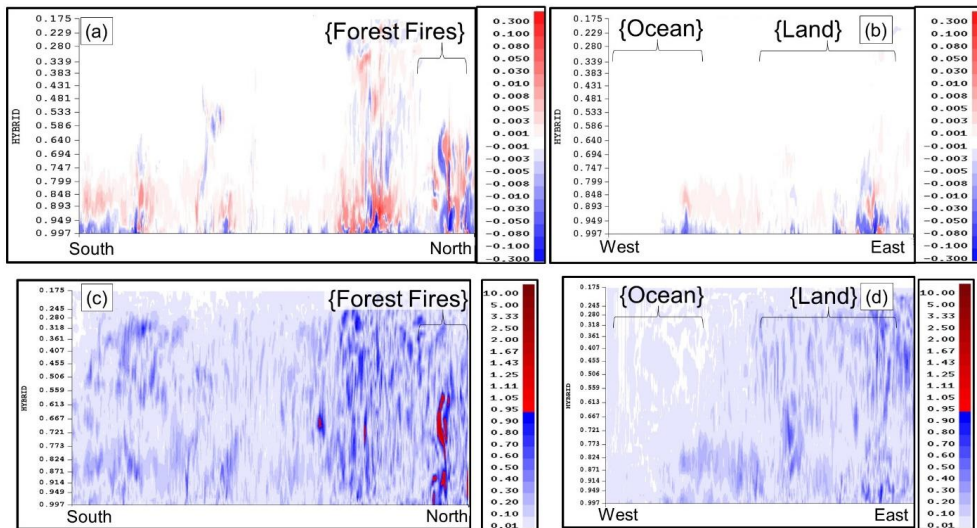


Figure 2223: (a,b) Difference (Feedback – No-Feedback) in predicted mean PM2.5 ($\mu\text{g m}^{-3}$), along domain-center South-North and West – East cross-sections. (c,d) Corresponding confidence ratio of mean differences – red areas indicate ratio values greater than unity, i.e., significance at or above the 90% confidence level. Note that colour bar scales differ between (a) and (b).



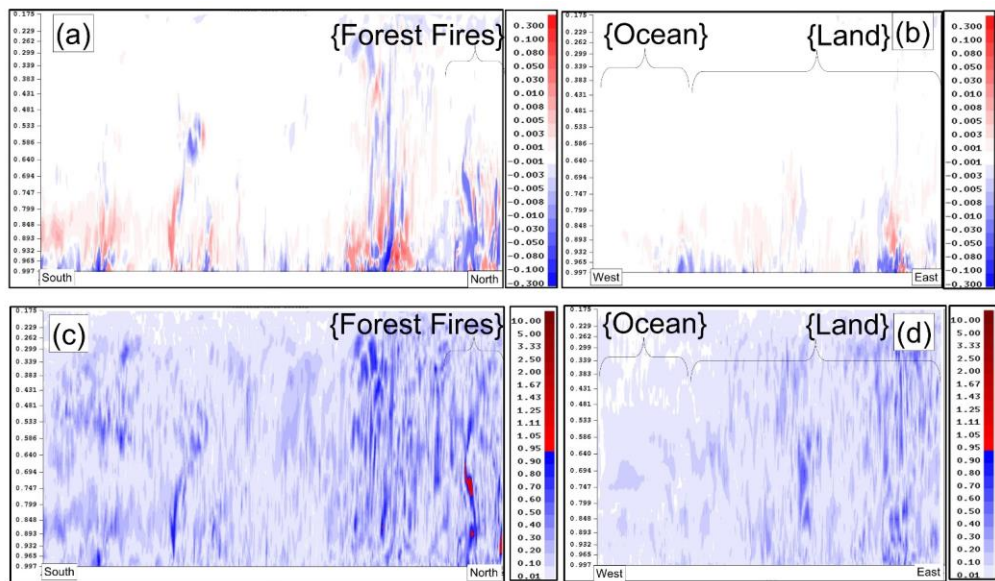


Figure 2324: (a,b) Difference (Feedback – No-Feedback) in predicted mean NO₂ (ppbv), along domain-center South-North and West – East cross-sections. (c,d) Corresponding confidence ratio of mean differences – red areas indicate ratio values greater than unity, i.e., significance at or above the 90% confidence level.

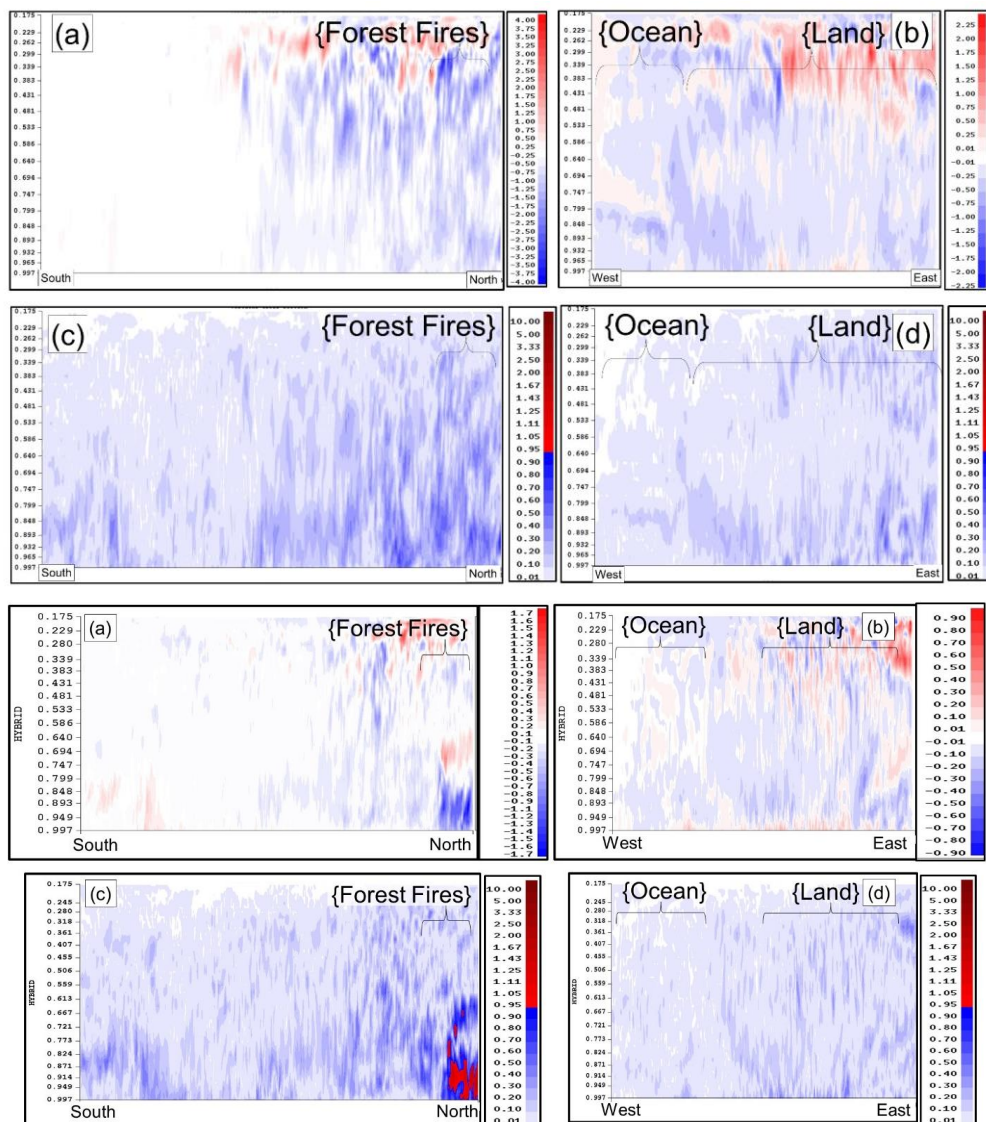


Figure 2425: (a,b) Difference (Feedback – No-Feedback) in predicted mean O_3 (ppbv), along domain-center South-North and West – East cross-sections. (c,d) Corresponding confidence ratio of mean differences – red areas indicate ratio values greater than unity, i.e., significance at or above the 90% confidence level. Note that colour bar scales differ between (a) and (b).